

ANGULAR AND POLARISATION  
CORRELATION MEASUREMENTS ON THE  
 $2^1P$  AND  $3^1P$  STATES OF HELIUM

BY

KHALID SALMAN IBRAHEIM  
M.Sc. EN SHAMES UNIVERSITY, EGYPT

THESIS SUBMITTED TO THE UNIVERSITY OF STIRLING  
FOR THE DEGREE OF DOCTOR OF PHILOSOPHY

ATOMIC PHYSICS LABORATORY  
UNIVERSITY OF STIRLING,  
SCOTLAND, U.K.

SEPTEMBER 1986

5/87

### ABSTRACT

The delayed coincidence technique was applied to investigate angular and polarization correlations between electrons scattered inelastically from helium atoms and photons emitted in the decay of  $n^1P$  states.

Electron photon angular correlations were studied for the excitation of the  $2^1P$  and  $3^1P$  states of helium at an incident electron energy of 50 eV and for electron scattering angles in the range of  $20^\circ - 102^\circ$  and  $35^\circ - 55^\circ$  respectively. From the analysis of these measurements the excitation parameters  $\lambda = \frac{|a_0|^2}{2|a_1|^2 + |a_0|^2} = \frac{\sigma_0}{\sigma}$  and the magnitude  $|\chi|$  of the phase difference between the excitation amplitudes  $a_{M_L}$  for the  $M_L = 1$  and  $M_L = 0$  states are obtained

Using the  $3^1P - 2^1S$  decay light the electron-photon polarization correlation were measured for the  $3^1P$  state of helium at electron impact energies 50, 80, 120 and 160 eV and for electron scattering angles between  $27.5^\circ$  and  $108^\circ$ . The Stokes parameters  $\eta_1$ ,  $\eta_2$  and  $\eta_3$  were derived and the sign change of the angular momentum transfer  $\langle L_y \rangle$  to the atom was investigated using the circular polarization results ( $\eta_2$ ). A sign change was confirmed for all energies studied and the scattering angle of the sign change was found to increase with decreasing electron energy. The excitation parameters  $\lambda$  and  $\chi$  have been derived and the present results are compared with theoretical calculations and with previous experimental values obtained from angular and polarization correlation measurements.

## CONTENTS

	page
<b>ABSTRACT</b>	
<b>ACKNOWLEDGEMENTS</b>	
<b>CHAPTER I</b>	
<b>Introduction</b>	1
<b>CHAPTER II - THEORETICAL CONSIDERATIONS</b>	
<b>Theory of coincidence experiments</b>	10
<b>Excitation process</b>	13
<b>Electron-photon angular correlation</b>	15
<b>Electron-photon polarization correlation</b>	19
<b>Angular momentum transfer</b>	23
<b>CHAPTER III - THE APPARATUS</b>	
<b>Introduction</b>	30
<b>Vacuum system</b>	31
<b>The 127° electron analyser</b>	35
<b>The electron gun assembly</b>	40
<b>Atomic beam source</b>	48
<b>The optical system for the polarization measurements</b>	53
<b>Introduction</b>	53
<b>Alignment</b>	55
<b>The photomultiplier</b>	55
<b>The voltage divider</b>	57
<b>Detection of VUV photons and scattered electrons</b>	61

	page
Introduction	61
VUV photon detection	61
Scattered electron detection	61
Coincidence circuit	64
Interlock system	66
<b>CHAPTER IV - MEASUREMENTS AND DATA ANALYSIS</b>	
Electron signal	67
The alignment of the electron beam and the analyser	67
Performance of the electron gun	67
The 127° electron analyser	68
Energy loss spectrum	68
Photon signal	72
Alignment of the photon detector	72
Photon detection	72
Single photon polarization	74
Resonance radiation	74
Coincidence time spectra and analysis	76
Coincidence signal	76
Coincidence analysis	79
Analysis of the angular correlation data	82
Polarization correlation analysis	84
Linear polarization measurements	85
Circular polarization analysis	85
<b>CHAPTER V - RESULTS AND DISCUSSION</b>	
Angular correlation measurements	90
Electron-photon polarization correlations	98

	page
Linear polarization measurements	98
Circular polarization results	102
The excitation parameters	110
CHAPTER VI - CONCLUSIONS	129

TO MY CHILDREN

OMAR

REBA

& ALI

### ACKNOWLEDGEMENTS

I wish to express my profound gratitude to Professor H Kleinpoppen as my principle supervisor. His advice and encouragement throughout this period has been a source of great inspiration to me.

One of the pleasures throughout the planning and running of the system was to work with Dr H J Beyer. I should like to thank him very much for his constructive criticism and co-operation in helping me to overcome various difficulties. His able guidance and continued pressure on me throughout this work has given me a greater understanding of the polarized light analysis.

My thanks go to Dr A J Duncan who, as my second supervisor, has always been very helpful.

My thanks also go to Professors H R Wilson (Head of the Department), and L.I. McIntyre, as well as to Drs. Ian McGregor and Mike Roberts for their co-operation and assistance.

I wish to thank Chief Technician Mr Alan J Duncan and Senior Technicians Mr Alasdair Sherman and Mr James Weir.

My thanks also to Mrs H Queen who typed this thesis despite her other pressing commitments.

I acknowledge financial support from the University of Al Moustansoryah (Iraq).

Finally ...

Finally I am much indebted to my mother and brothers, especially Hashim, for their patience, co-operation and help in making this exercise a success.

CHAPTER I

INTRODUCTION

Electron-atom collisions have been the subject of a great deal of experimental and theoretical effort since the early days of atomic physics. Collision phenomena such as elastic scattering, electron impact excitation and ionization have been investigated for a wide range of atomic systems and incident projectile energies.

The experimental determination of total and differential cross sections as well as measurements of optical excitation functions and of the polarization of atomic line radiation produced by electron impact have provided important tests for theoretical models of electron-atom scattering processes.

The traditional experimental investigations of the electron impact excitation of atoms were of two types.

1. The first type of experiment detects the scattered electrons only. Such experiments yield values for total excitation cross-sections, as a function of incident electron energy. Such cross-sections represent sums of partial cross-sections for the excitation of each degenerate or unresolved atomic state. If electrons are detected as a function of the scattering angle, differential cross-sections are obtained.
2. In the second type of experiment, the radiation resulting from the spontaneous decay of an atom which has been excited by electron impact is observed without regard to the scattered electrons. Such experiments can yield values for the total excitation cross section or, if the polarization of the emitted radiation is measured, information on the total cross-sections for excitation of individual magnetic sublevels (Hamilton (1940)).

The polarization of helium line radiation excited by electron impact has been the subject of both theoretical and experimental

investigations since the first measurements were made by Steiner (1928). These measurements have been of interest since the polarization of the emitted light depends upon the population distribution between the  $M_L$  sublevels. Percival and Seaton (1958) predicted for a singlet P state, that at threshold only the  $M_L=0$  sublevels is excited and the light is 100% polarized parallel to the incident electron beam. In the high-energy limit, only the  $M_L = \pm 1$  sublevels are excited and the light is 100% polarized perpendicular to the incident electron beam.

The traditional work in electron-atom collisions as described so far has usually involved averaging over fundamental collision parameters with the result that important detail is lost. For example, measurements of the line polarization involve an average over all electron scattering angles since the analysis of the radiation takes place without regard to the electrons. More detailed information of the collision process can be obtained by an experiment which only analyzes the radiation emitted from atoms which are excited to a given state by electrons scattered in a particular direction. The method of detecting inelastically scattered electrons in delayed coincidence with photons emitted in a given direction provides a technique for precisely this kind of measurement.

The method to detect two particles in delayed coincidence has been in use for many years in the field of nuclear physics. It was used by Brady and Deutsch (1949) to investigate the non-isotropic emission of gamma rays, which had been predicted by Dunsworth (1940). The theory developed for nuclear studies is not directly applicable to atomic studies but many features of the theory have closely followed earlier developments in the field of nuclear physics.

The first full theoretical treatment of photon-particle coincidence measurements applied to atomic studies was given

by Macek and Jaecks (1971). The field has been further developed by Fano and Macek (1973), Blum and Kleinpoppen (1979) and Blum (1981).

For the study of electron-atom collision processes, the electron-photon coincidence technique was first used by Eminyán et al. (1973) for the excitation of the  $2^1P$  state of helium. The importance of the technique lies in its capability of measuring the complete excitation amplitudes  $|a_M|$  of the sub-states including their relative phases. These may be represented by the dimensionless parameters  $\lambda = \frac{|a_0|^2}{|a_0|^2 + 2|a_1|^2}$  and  $\chi$ , the phase difference between  $a_0$  and  $a_1$ . The amplitudes are related directly to the way in which angular momentum is transferred to the atom during the collision process, and the results of electron-photon coincidence experiments thus give direct information on the dynamics of the collision process.

The coincidence method has been used in many areas of atomic physics. Imhof and Read (1969) have used the electron-photon coincidence technique to eliminate cascade effects from higher states in the measurement of the excited state lifetime of the  $4^1S$  state of helium. This technique has since been used widely, e.g. Imhof and Read (1971a,b,c) and (1977). Pochat et al. (1973) measured differential cross-sections for electron impact excitation of the  $n=4$  and 5 states of helium using the decay photons of appropriate wavelengths to uniquely specify the coincident scattered electrons. The coincidence technique has been used by other groups, e.g. Smith et al. (1973 and 1975), Shaw et al. (1975), King and Adam (1974), and King et al. (1975), to measure lifetimes in atoms and molecules.

Besides the electron-photon coincidence methods which have been used in the present experiment, two other commonly used delayed coincidence techniques are the photon-photon coincidence and the electron-electron coincidence method. The photon-photon coincidence

method was first used by Brannen et al. (1955) to measure the lifetime of the  $7^3S$  state of mercury. Photon-photon coincidences, have further been used by Kaul (1966), Poppet et al. (1970), Holt and Pipkin (1974), and King and Read (1975, 1976)

The electron-electron coincidence method was first reported by Ehrhardt et al. (1969) where the correlations between the outgoing electrons from the ionization of helium were measured. This technique of detecting the scattered and ejected electrons in coincidence has been used by various groups for the measurement of the ionization of atoms by electron impact, e.g. Weigold et al. (1973), Ehrhardt et al. (1974), Back et al. (1975), Jung et al. (1975), and Crowe (1982).

In order to determine the excitation amplitudes, an electron-photon coincidence experiment can be performed in two equivalent ways. Firstly, electron-photon angular correlations can be measured between the inelastically scattered electrons and the photons emitted during the collision from which  $\lambda$  and  $|\chi|$  parameters can be obtained. Alternatively, the same information can be obtained by measuring the polarization of the emitted radiation. However, the sign of  $\chi$ , the phase difference between the excitation amplitudes cannot be determined from the angular correlation measurements. For this one has to measure the circular polarization of the emitted radiation.

The first electron-photon angular correlation measurements in coincidence were carried out by Eminyán et al. (1973) for the  $2^1P$  state of helium and lead to values for  $\lambda$  and  $|\chi|$  as mentioned above.

This first experiment was followed by a series of measurements on helium by Eminyán et al. (1974, 1975), Tan et al. (1977), Sutcliffe et al. (1978), Fon et al. (1979), Hollywood et al. (1979),

Slevin et al. (1980) and Steph and Golden (1979). Neill et al. (1984) studied the behaviour of the excitation parameters as the incident electron energy approached the threshold energy where their values are expected to be governed by simple threshold arguments. They measured the angular correlation between scattered electrons and emitted photons for the  $2^1P$  state of helium at an incident electron energy of 22.0 eV (0.8 eV above threshold) and for scattering angles up to  $120^\circ$ .

Measurements of the  $3^1P$  state of helium were carried out by Eminyan et al. (1975), Standage and Kleinpoppen (1976), Crowe et al. (1981) and MacAdams and Williams (1982). The same technique has been applied to the  $2P$  state of atomic hydrogen by Williams (1975), Dixon et al. (1978) and Slevin et al. (1985).

The electron-photon angular correlation method has also been used on neon by Ugbabe et al. (1977), and on argon by Arriola et al. (1975). Further measurements on Ar were reported by Malcolm and McConkey (1979) who determined  $\lambda$  and  $|\chi|$  as well as the threshold polarization for the resolved Ar lines at 104.8 and 106.7 nm. Malik and Kleinpoppen (1980) studied the electron-photon angular correlations for the  $4p^5(^2P_{3/2})5S^3P_1$  and  $4p^5(^2P_{1/2})5S^1P_1$  states of krypton and the  $5p^5(^2P_{3/2})6S^3P_1$  state of xenon to determine the collision parameters  $\lambda$ ,  $|\chi|$  and  $\cos \epsilon$ , where  $\cos \epsilon$  is a new parameter suggested by Blum and Paixao (1980); this parameter takes into consideration the spin-orbit interaction experienced in heavy atoms. A value of  $\cos \epsilon$  equal to 1 indicates the absence of spin-orbit interactions. The deviation of the value of  $\cos \epsilon$  from 1 is a measure of the strength of the spin-orbit interaction experienced by the target atom.

The same information as for angular correlation measurements can be obtained from linear polarization measurements where the

emitted light is observed in a direction perpendicular to the scattering plane. A circular polarization measurement further determines the sign of the relative phase  $\chi$ .

Non-coincidence polarization measurements were carried out by McFarland (1964), who investigated the polarization of the  $4^1D - 2^1P$  (492 nm) line of helium. Heddle and Kissing (1967) and Heideman et al. (1969) found a rapid change of the polarization close to threshold for a number of lines. Similarly, the work of Federov and Mezentev (1965), on the polarization of the  $7^1D_2 - 6^1P_1$  (434.7 nm),  $7^3S_1 - 6^3P_1$  (435.8 nm) and  $6^3D_2 - 6^1P_1$  (577.0 nm) lines of mercury revealed a sharp change near threshold. Hafner, Kleinpoppen and Krüger (1967), measured the threshold polarization of the resonance lines of  $^6Li$ ,  $^7Li$  and  $^{23}Na$  and their results were in good agreement with the theoretical calculations of Flower and Seaton (1967) for the same lines, using the theory of Percival and Seaton (1958). Ottley and Kleinpoppen (1975) carried out polarization studies of the  $6^3P_1 - 6^1S_0$  (253.7 nm) lines of mercury close to threshold.

Polarization values of the light as above can be derived from angular correlation measurements and this was done by Steph and Golden (1982) who studied the polarization fraction of the  $2^1P$  and  $3^1P$  states in helium for electron impact energies from 30 to 500 eV. Standage (1977) used the previous angular correlation data of Eminyan et al. (1973, 1974, 1975), and the polarization data of Standage and Kleinpoppen (1976) to study the polarization of the helium line radiation at incident electron energies from 60 to 100 eV, for the transitions  $2^1P - 1^1S$  (58.5),  $3^1P - 1^1S$  (53.7 nm) and  $3^1P - 2^1S$  (501.6 nm).

The electron-photon coincidence technique was used by King et al. (1972) to measure the threshold polarization of the impact line radiation in the  $3^1P$  state of helium at an incident electron energy of 80 eV.

Standage and Kleinpoppen (1976) reported the first complete polarization analysis for the  $3^1P_1 - 2^1S_0$  (501.6 nm) line of helium at an impact energy of 80 eV and scattering angles between  $15^\circ$  and  $27.5^\circ$ . The circular polarization measurements determine the sign of the relative phase  $\chi$  which can not be obtained from the angular correlation measurements.

Zehle et al. (1978) measured the linear and circular polarization of the  $K(4^2P \rightarrow 4^2S)$  photons detected in delayed coincidence with inelastically scattered potassium atoms for K-He, K-Ne and K-Ar collisions as a function of the projectile scattering angle.

Anderson et al. (1979) performed similar measurements of the Stokes parameters for  $Mg(3^2P - 3^2S)$  photons in a coincidence experiment involving  $Mg^+ - He, Ne$  and  $Ar$  collisions and Zaidi et al. (1980) measured the linear and the circular polarization of the  $(6^3P_1 - 6^1S_0)$  line in mercury.

Recently, the change in the sign of the orientation has been discussed by Herman and Hertel (1980). Kohmoto and Fano (1981), Madison and Winters (1981), Blum (1981), Fon et al. (1980) and later by Beyer et al. (1982) along the line of the classical grazing model.

Hermann and Hertel (1980), Madison and Winters (1981) and Fon et al. (1980) predicted theoretically that, since the electrons scattered at  $0^\circ$  and  $180^\circ$  can not transfer angular momentum,  $\langle L_y \rangle$  (and thus  $O_{1-}^{col}$ ) is constrained to be zero at these angles. Based on the classical grazing model the orientation between these two extremes should be positive at small scattering angles and negative at large scattering angles, passing through zero at some intermediate angle. Kohmoto and Fano (1981) have attempted to justify a simple classical grazing model which can be used to relate the attractive or repulsive nature of the interaction to the sign of the orientation produced.

They conclude that a change in sign of the interaction (e.g. from attractive to repulsive) results in a change of sign of the orientation: a result consistent with a classical grazing model. Blum (1981) suggested that the negative orientation is due to a repulsive force and the positive orientation due to an attractive force.

Hollywood et al. (1978) calculated the absolute value of the orientation from the parameters  $\lambda$  and  $|\chi|$  measured in an angular correlation experiment on the  $2^1P$  state up to scattering angle of  $130^\circ$ . Their data strongly suggest the presence of a sign reversal in the orientation at  $\theta_e = 70^\circ$  but since they measured only  $|\chi|$  they could not positively prove it.

MacAdams and Williams (1981) determined the excitation parameters  $\lambda$  and  $|\chi|$  from angular correlation measurements for  $He(3^1P)$  at an incident energy of 81.2 eV for electron scattering angles between  $60^\circ$  and  $120^\circ$ . Beijers et al. (1984) studied the orbital angular momentum transfer from the angular correlation measurement of the  $2^1P$  state of helium, at incident energies of 50, 60 and 80 eV. They found that, at an energy of 80 eV, the orbital angular momentum transferred by the electrons to the atom during the collision appears to change sign at a scattering angle of about  $65^\circ$ . However, at energies of 50 and 60 eV no indication of a sign change was found.

To clarify the situation, circular polarization measurements are essential and such measurements on the  $3^1P$  state on helium are reported in this thesis. A similar measurement on the  $2^1P$  state is being carried by Khakoo et al. (1986) and their first results for 50, 60 and 80 eV confirm the sign change of the angular momentum transfer found in the present work for the  $3^1P$  state.

#### The Aim of this Work

The aim of the present work was to establish whether the angular

momentum  $\langle L_y \rangle$  transferred to the atom during the excitation of the  $3^1P$  state, changes sign at some intermediate scattering angle. Furthermore, the energy dependence of the angle at which the sign changes should be investigated. At the same time the complete linear and circular polarization analysis of the  $3^1P - 2^1S$  (501.6 nm) line of helium should be extended to large scattering angles and a wide range of electron impact energies.

In Chapter II of this thesis, the relevant theory of the electron impact excitation and the subsequent decay of the  $n^1P$  state of helium is outlined. Chapter III describes the apparatus used. Chapter IV describes the measurements and the analysis. Chapter V presents the results and discussion. Chapter VI the Conclusions.

## CHAPTER II

## THEORETICAL CONSIDERATIONS

2.1 Theory of coincidence experiments

In electron-atom collisions, some excited atoms are produced which subsequently decay by photon emission. Macek and Jaecks (1971) derived an expression relating the coincidence rate  $dN_c$  to the amplitudes which describe the excitation process. They considered that the atom which is initially in the ground state, is excited to a set of degenerate or nearly degenerate upper states by electron impact. The atom in turn decays from the upper levels to a set of closely spaced lower levels. In all practical cases the collision takes place in a time short compared with the radiative lifetime. Thus at time  $t=0$  the collision occurs producing a set of excited states  $(SM_S, LM_L)$ , where S and L are, respectively, the total spin and orbital momenta and  $M_S$  and  $M_L$  their projections along the incoming electron beam axis z. The wave function of the excited atom is then

$$|\psi(t=0)\rangle = \sum_{M_S M_L} a(SLM_S M_L) |SLM_S M_L\rangle \quad 1.2$$

where  $a(SLM_S M_L)$  is the probability amplitude for exciting this atomic state from the ground state. It is a function of the incident electron energy and scattering angles ( $\theta_e$  and  $\phi_e$ ).  $|SLM_S M_L\rangle$  is the state vector describing a particular atomic state. After the collision the upper states evolve with time under the influence of fine and hyperfine interactions and of the radiation field. The probability of photon emission for a given transition has been calculated by Percival and Seaton (1958), and expressions were obtained relating the partial cross

sections to the polarization of the atomic line radiation. Their results, however, are averaged over all directions of the scattered electrons and integrated over time. Wykes (1972) has extended the Percival and Seaton theory and expressed the probability of observing polarized photons as a function of the direction of emission for a given electron scattering angle. An equivalent way to calculate the probability of light emission for excitation by short light pulses was taken by Macek and Jaecks (1971).

At time  $t$  after the collision the wave function can be described by (assuming that there are no external fields)

$$|\psi(t)\rangle = \sum_{JFM_F} a(JFM_F) |JIFM_F\rangle e^{-\left(\frac{\gamma}{2} + i E_{JF}/\hbar\right)t} \quad 2.2$$

where  $J$  is the electronic angular momentum,  $F$  is the total angular momentum.  $I$  is the nuclear spin,  $E_{JF}$  is the energy of a particular atomic state and the factor  $e^{-\gamma t/2}$  is included to account for the decay of the upper level population. Here  $\frac{1}{\gamma}$  is the mean lifetime of the excited atom.

Assuming that the atomic levels are adequately described by LS coupling, the amplitudes can be written by usual coupling rules in the following way

$$a(JFM_F) = \sum_{M'_L M'_S M'_I M_J} (a(LM'_L SM'_S IM'_I)) ((LM'_L SM'_S | LS, M_J)(JM_J IM'_I | JIFM_F)) \quad 2.3$$

In the electric dipole approximation, the probability of observing a photon with momentum  $K$  and polarization  $\hat{\epsilon}$  in a time interval  $\Delta t$  after the collision, while the electrons are scattered in a direction  $(\theta_e, \phi_e)$ , is proportional to the square of the electric dipole matrix element.

Thus,

$$\omega(E, \theta, \phi; K, \hat{\epsilon}, t) = C \sum_{\mu} \int_t^{t+\Delta t} |\langle \psi_{\mu} | \hat{\epsilon} \cdot D | \psi(t) \rangle|^2 dt \quad 2.4$$

where C is an overall normalization constant,  $|\psi_{\mu}\rangle$  is the wave function of the state reached in the light emission,  $\hat{\epsilon}$  is the polarization vector of light, D is the electric dipole moment operator. Expanding equation 2.4.

$$\omega(E, \theta, \phi; K, \hat{\epsilon}, t) = C \sum_{J_0 F_0 M_{F_0}} \left| \sum_{J F M_F} \langle J_0 F_0 M_{F_0} | \hat{\epsilon} \cdot D | J F M_F \rangle a(J F M_F) \right|^2 \int_t^{t+\Delta t} e^{-(\gamma + i(E_{JF} - E_{J_0 F_0})/\hbar)t} dt \quad 2.5$$

where  $\omega(E, \theta, \phi; K, \hat{\epsilon}, t)$  is equivalent to  $\frac{dN_c}{d\Omega_e d\Omega_{\gamma}}$  (Macek and Jaecks (1971)) which gives the number of counts per unit of time in terms of the amplitudes  $a(J F M_F)$ , the dipole matrix elements and the time dependent factor.

Macek and Jaecks (1971), derived the coincidence rate for the excitation of the  $n^1P$  state of helium as follows

$$\frac{dN_c}{d\Omega_e d\Omega_{\gamma}} = C \frac{|\langle 0 | D | 1 \rangle|^2}{3} \sum_M a(M) a^*(M') a_M^{(\alpha)} a_{M'}^{(\alpha)*} \int_t^{t+\Delta t} e^{-\gamma t} dt \quad 2.6$$

where C is an overall normalization constant.

## 2.2 Excitation Process

The total wave function of the excited singlet P states for electrons scattered in a particular direction  $(\theta_e, \phi_e)$  with respect to the incident electron beam, can be described as a coherent superposition of degenerate magnetic sublevels, Macek and Jaecks (1971) as follows

$$|\psi\rangle = a(1)|11\rangle + a(0)|10\rangle + a(-1)|1-1\rangle \quad 2.7$$

where  $a(1)$ ,  $a(0)$  and  $a(-1)$  are the scattering amplitudes. It is assumed that spin-spin and spin-orbit interaction in the collision can be neglected.

The excitation amplitudes  $a(M)$  are functions of the electron scattering angles  $(\theta_e, \phi_e)$  and of the incident electron energy  $E$ . They describe the excitation to particular magnetic sublevels  $|JM\rangle$  of the  $3^1P$  state ( $L = 1$ ). The dependence on  $\phi_e$  can be factored out so that in the following we use amplitudes that depend only on  $E$  and  $\theta_e$

$$a(M; E, \theta_e, \phi_e) = a_M(E, \theta_e) e^{-iM\phi_e} \quad 2.8$$

The mirror symmetry of the scattering process in the scattering plane implies  $a_1 = a_{-1}$ .

$|\psi\rangle$  can be normalized,  $(\langle\psi|\psi\rangle = \sigma_M)$ , so that the amplitudes are related to differential cross sections as follows

$$|a_1|^2 = \sigma_1 \quad 2.9$$

$$|a_0|^2 = \sigma_0 \quad 2.10$$

$$2|a_1|^2 + |a_0|^2 = \sigma \quad 2.11$$

Here  $\sigma$  is the differential cross section for exciting the  $n^1P$  state and  $\sigma_m$  is the differential cross section for exciting the magnetic sublevel. The amplitudes  $a(M)$  are in general complex numbers. However, since  $|\psi\rangle$  is defined only up to an overall phase factor,  $a_0$  may be assumed to be real and positive. The relative phase  $\chi$  between  $a_1$  and  $a_0$  is defined by

$$a_1 = |a_1| e^{i\chi} \quad (-\pi < \chi < \pi) \quad 2.12$$

Therefore  $|\psi\rangle$  is described completely for given  $E$ ,  $\theta_e$  and  $\phi_e$  by parameters  $\sigma, \lambda = |a_0|^2 / (2|a_1|^2 + |a_0|^2) = \frac{\sigma_0}{\sigma}$ , ( $0 < \lambda < 1$ ) and  $\chi$  which could be in any region of  $2\pi$ .

$\lambda$  and  $\chi$  are functions of the energy and the scattering angle. They are dimensionless parameters describing the excited state of an atom after the collision and together with the total differential cross section  $\sigma = |a_2|^2 + 2|a_1|^2$  provide a complete determination of the scattering amplitudes.

### 2.3 Electron-photon angular correlation

The theory of angular correlation has been discussed in detail previously by Macek and Jaecks (1971). They described the angular correlations between photons and scattered electrons in terms of scattering amplitudes.

Substituting the spherical components of the polarization vectors into equation (2.6), integrating over the resolution time of the coincidence circuit  $\Delta t$ , and summing over the photon polarization, Eminyan et al. (1974) obtained

$$\frac{d^2 N_c}{d\Omega_e d\Omega_\gamma} = \frac{\sigma}{\Sigma} \frac{dN_c}{d\Omega_\gamma} \quad 2.13$$

where

$$\begin{aligned} \frac{dN_c}{d\Omega_\gamma} = \frac{3}{8\pi} \left( \lambda \sin^2 \theta_\gamma + \frac{1}{2} [1-\lambda] (\cos^2 \theta_\gamma + 1) - \frac{1}{2} [1-\lambda] \right. \\ \left. \sin^2 \theta_\gamma \cos 2(\phi_\gamma - \phi_e) + [\lambda(1-\lambda)]^{\frac{1}{2}} \right. \\ \left. \cos \chi \sin 2\theta_\gamma \cos(\phi_\gamma - \phi_e) \right) = \frac{3}{8\pi} N \end{aligned} \quad 2.14$$

Here  $\frac{d^2 N_c}{d\Omega_e d\Omega_\gamma}$  is the joint probability density for the electron to be scattered in the direction  $(\theta_e, \phi_e)$  in any  $n^1P$  excitation, with subsequent emission of the photon in the direction  $(\theta_\gamma, \phi_\gamma)$ .  $\sigma$  is the differential cross section.  $\Sigma$  is the total (integrated) cross section for excitation of the  $n^1P$  state at energy  $E$ , and  $\frac{dN_c}{d\Omega_\gamma}$  is the probability density for photon emission after electron scattering in a particular direction on which  $\lambda$  and  $\chi$  depend.

Figure (2-1) shows a schematic diagram of the coordinate system. The electron beam is incident in  $z$ -direction on the target located at the origin of the coordinate system. Scattered electrons are collected

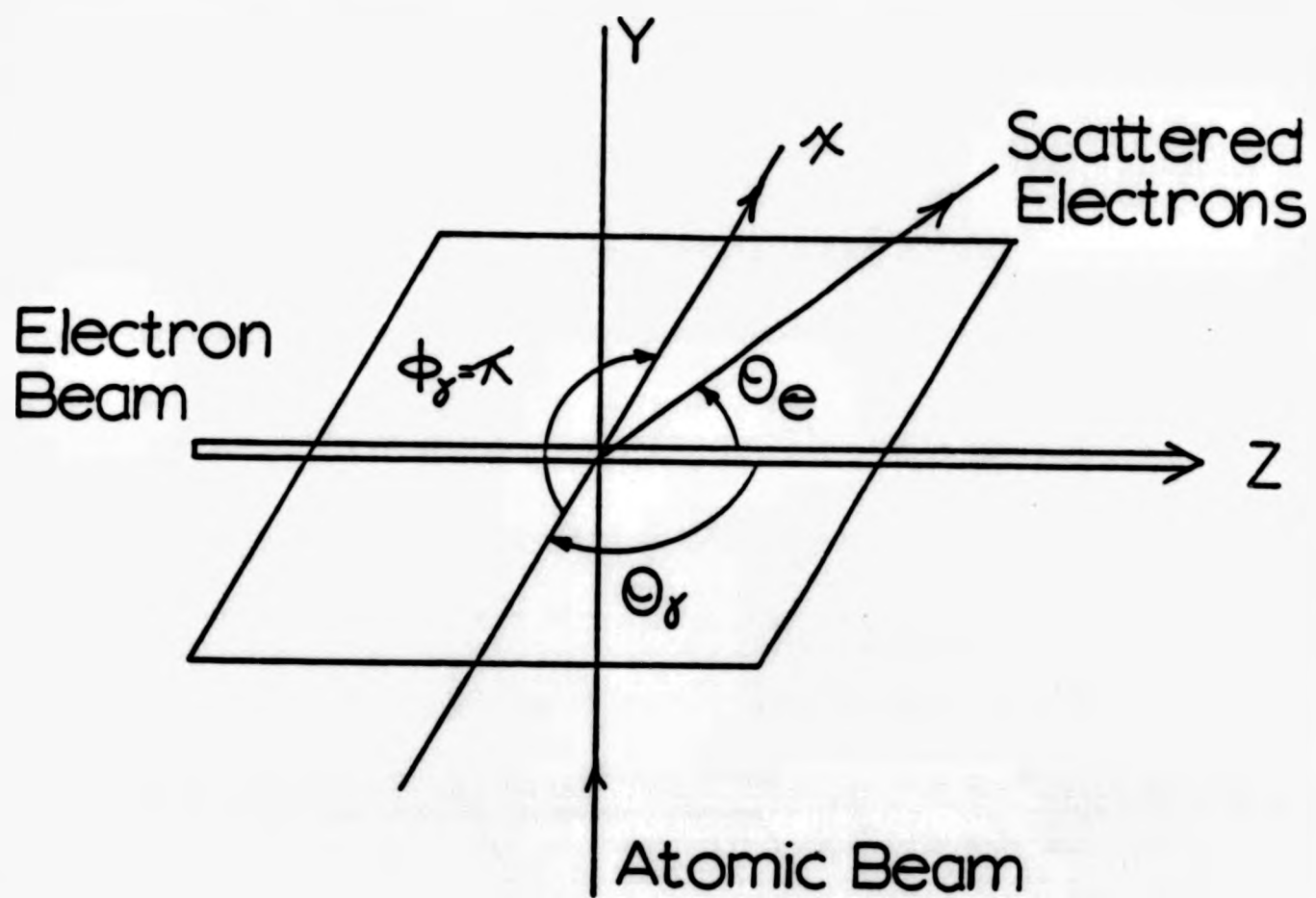


Figure (2-1): Geometry of the electron photon coincidence experiment using the crossed-beam technique.

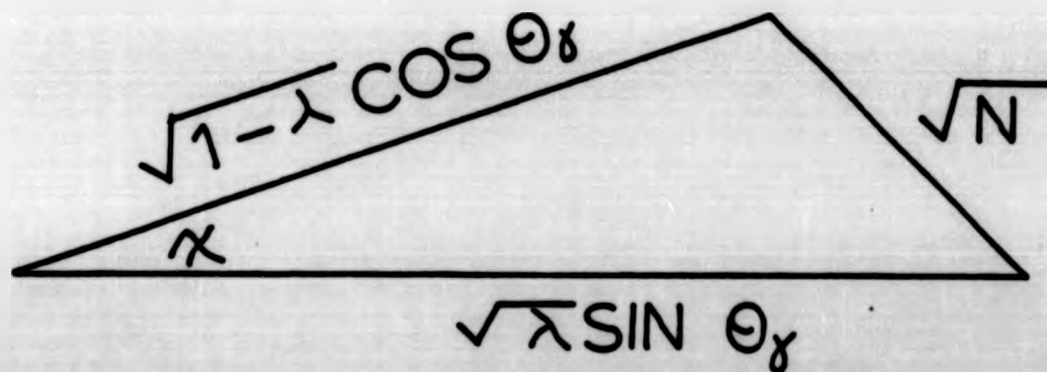


Figure (2-2): Geometrical representation of the angular correlation function (equation 2.15).

by a  $127^\circ$  electron analyser whose position defines the scattering plane, which is taken to be the  $xz$  plane. Therefore, the azimuthal angle  $\phi_e$  is zero for all detected scattering events. Photons are detected without regard to polarization by a detector placed in the  $xz$  plane on the opposite side of the electron beam from the analyser, i.e.  $\phi_\gamma = \pi$ . In this case the angular correlation function in equation (2-14) takes the form

$$N = \lambda \sin^2 \theta_\gamma + (1-\lambda) \cos^2 \theta_\gamma - 2[\lambda(1-\lambda)]^{\frac{1}{2}} \sin \theta_\gamma \cos \theta_\gamma \cos \chi \quad 2.15$$

The angular correlation function  $N$  can be represented by the geometrical construction in figure (2-2) where  $\lambda = |a|^2 / (|a_0|^2 + 2|a_1|^2)$  and  $\chi$  the phase difference between the scattering amplitudes  $a_1$  and  $a_0$ .

The information obtained from a measurement of the linear polarization is identical to that given by a photon angular distribution. Consider a linear polarizer set at an angle  $\alpha$  in front of the photon detector. The probability density for scattering an electron in a given direction with subsequent emission and observation of the photon is

$$\frac{d^3 N_c}{d\Omega_e d\Omega_\gamma}(\alpha) = \frac{\sigma}{\Sigma} \left( \left( \frac{dN_c}{d\Omega_\gamma} \right)_{\hat{\epsilon}^{(1)}} \cos^2 \alpha + \left( \frac{dN_c}{d\Omega_\gamma} \right)_{\hat{\epsilon}^{(2)}} \sin^2 \alpha \right) \quad 2.16$$

where  $\left( \frac{dN_c}{d\Omega_\gamma} \right)_{\hat{\epsilon}^{(1,2)}}$  is the probability density for photon emission polarized along  $\hat{\epsilon}^{(\alpha)}$  (which is the polarization unit tensor) as obtained from equation (2.6).

Thus,

$$\frac{dN_c}{d\Omega_\gamma} \hat{\epsilon}^{(1)} = \frac{3}{8\pi} \left( \lambda \sin^2 \theta_\gamma + \left( \frac{1-\lambda}{2} \right) \cos^2 \theta_\gamma (1 - \cos^2(\phi_\gamma - \phi_e)) \right. \\ \left. + (\lambda(1-\lambda))^{\frac{1}{2}} \cos \chi \sin 2\theta_\gamma \cos(\phi_\gamma - \phi_e) \right) \quad 2.17$$

$$\text{and } \left( \frac{dN_c}{d\Omega} \right)_{\hat{\epsilon}}^{(2)} = \frac{3}{8\pi} \left( \left( \frac{1-\lambda}{2} \right) (1 - \cos^2 2(\phi_\gamma - \phi_e)) \right) \quad 2.18$$

Therefore, for the photon detector set at a fixed angle out of the plane of scattering (i.e.  $(\phi_\gamma - \phi_e) \neq 0, \pi$ ) the measurement of

$$\frac{d^2 N_c}{d\Omega_e d\Omega_\gamma} (\alpha)$$

obtained by rotating the polarizer axis yields values for  $\lambda$  and  $|\chi|$ .

#### 2.4 Electron-photon polarization correlation

In order to obtain information about the coherence properties of the emitted light, it is necessary to introduce quantities which completely characterize the quantum mechanical state of the emitted light. Such quantities are the elements of the polarization density matrix of photons, Blum and Kleinpoppen (1979), or, equivalently the Stokes parameters. These quantities have been discussed extensively by Born and Wolf (1976), Blum and Kleinpoppen (1979) and de Paixao et al. (1984).

These Stokes parameters are defined as follows in connection with the photon radiation observed perpendicular to the scattering plane.

$$I(\theta, \phi) = I(0) + I(90) = J_{zz} + J_{xx} \quad 2.19$$

$$I\eta_1 = I(0) - I(90) = J_{zz} - J_{xx} \quad 2.20$$

$$I\eta_3 = I(45) - I(135) = J_{xx} - J_{zz} \quad 2.21$$

$$I\eta_2 = I(\text{RHC}) - I(\text{LHC}) = i(J_{xz} - J_{zx}) \quad 2.22$$

where  $I$  represents the total intensity of the emitted light,  $\theta$  and  $\phi$  are the polar coordinates of the photon detector ( $\theta = \phi = 90$ ),  $I(0)$ ,  $I(90^\circ)$ ,  $I(45^\circ)$  and  $I(135^\circ)$  are the linearly polarized light intensities polarized under the angle  $\alpha$  as shown in figure (2-3).  $I(\text{RHC})$  and  $I(\text{LHC})$  are the right and left hand circular polarized components of the photon radiation.

Blum and Kleinpoppen (1979), produced an expression of the general coincidence rate in terms of the Stokes parameters as follows

$$I(\alpha) = \frac{I}{2} (1 + \eta_3 \cos 2\alpha + \eta_1 \sin 2\alpha \cos 2\delta + \eta_2 \sin 2\alpha \sin 2\delta) \quad 2.23$$

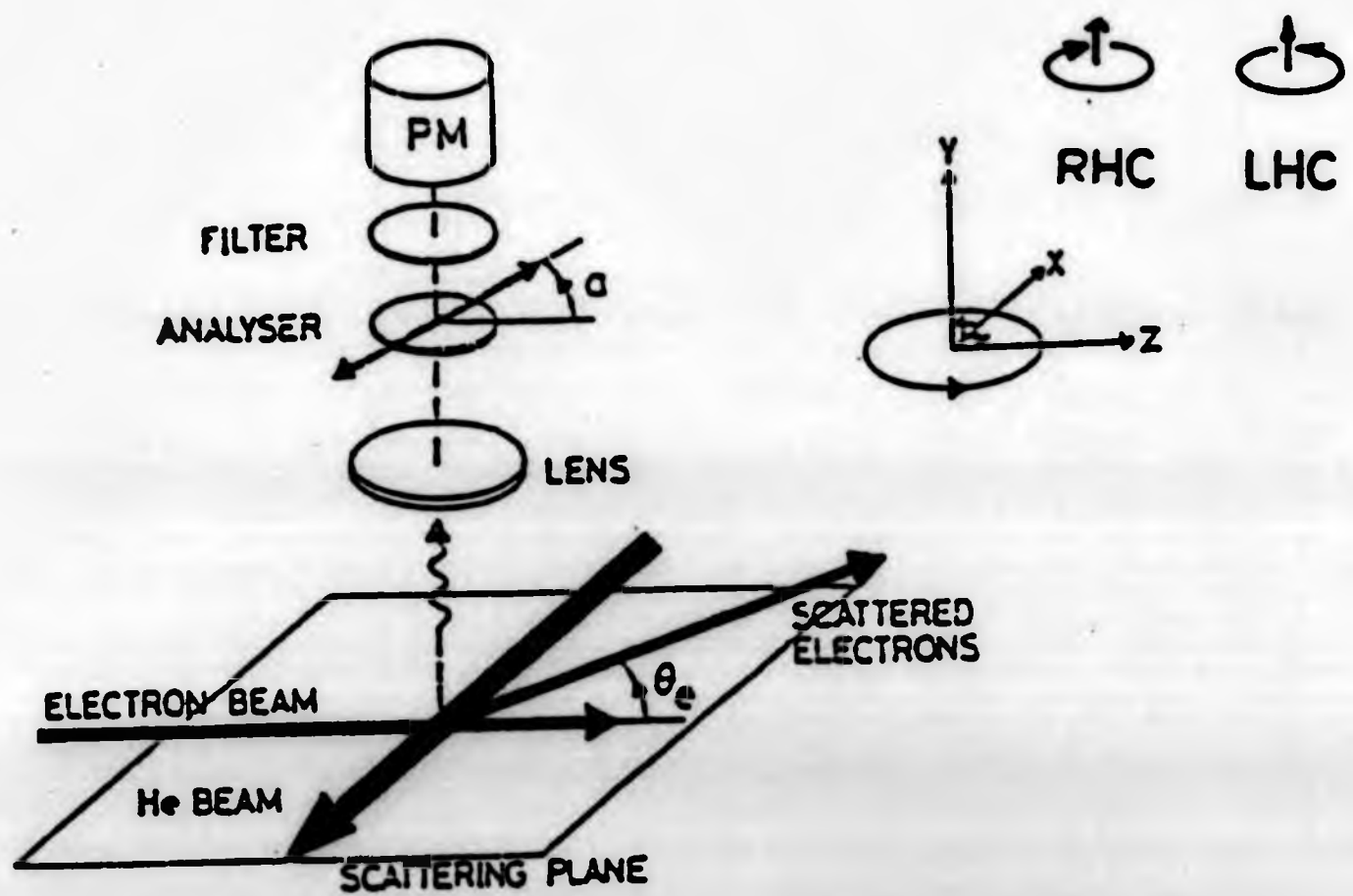


Figure 2-3: Schematic diagram of experiment. The x-z plane is the scattering plane; the photons are detected along the y axis. Scattering angle  $\theta_e$  and linear polarizer angle  $\alpha$  are measured in the x-z plane. Positive scattering angle is shown.

where  $\delta$  is the phase difference of the quarter wavelength plate.

Blum and Kleinpoppen (1979) found it convenient to describe the atomic ensemble by a set of state multipoles  $\langle T(L)_{KQ}^+ \rangle$  where  $K$  takes all values  $0, 1, 2, \dots, 2L$  and  $-K < Q < K$ . These can be expressed in terms of excitation amplitudes and for the cases of  $^1P$  and  $^3P$  states the relations take the following form:

$$\langle T(L)_{00} \rangle = \frac{\sigma}{3} \quad 2.24$$

$$\langle T(L)_{11} \rangle = -i\sigma\sqrt{\lambda(1-\lambda)} \sin\chi \quad 2.25$$

$$\langle T(L)_{20}^+ \rangle = \frac{\sigma}{\sqrt{6}} (1-3\lambda) \quad 2.26$$

$$\langle T(L)_{21}^+ \rangle = -\sigma\sqrt{\lambda(\lambda-1)} \cos\chi \quad 2.27$$

$$\langle T(L)_{22}^+ \rangle = \frac{\sigma}{2} (\lambda-1) \quad 2.28$$

The polarization state of the emitted photons is completely characterized by the four Stokes parameters. Blum and Kleinpoppen (1979) give general formulae for these parameters in terms of the state multipoles as follows

$$I = K(-1)^{L+L_f} \frac{2}{3\sqrt{2L+1}} \langle T(L)_{00}^+ \rangle - K \left\{ \begin{matrix} 1 & 1 & 2 \\ L & L & L_f \end{matrix} \right\} \left( \langle T(L)_{22}^+ \rangle \right. \\ \left. \sin^2\theta \cos\phi + \langle T(L)_{21}^+ \rangle \sin 2\theta \cos\phi + \frac{1}{\sqrt{6}} \langle T(L)_{20}^+ \rangle \right. \\ \left. (3\cos^2\theta - 1) \right) \quad 2.29$$

$$I_{\eta_3} = K \left\{ \begin{matrix} 1 & 1 & 2 \\ L & L & L_f \end{matrix} \right\} \left( \langle T(L)_{22}^+ \rangle (1 + \cos^2\theta) \cos 2\phi + \langle T(L)_{21}^+ \rangle \right. \\ \left. \sin 2\phi + \langle T(L)_{21}^+ \rangle \sin 2\theta \cos\phi + \sqrt{\frac{3}{2}} \langle T(L)_{20}^+ \rangle \sin^2\theta \right) \quad 2.30$$

$$I_{\eta_1} = -K \left\{ \begin{matrix} 1 & 1 & 2 \\ L & L & L_f \end{matrix} \right\} \left( \langle T(L)_{22}^+ \rangle 2 \cos\theta \sin 2\phi + \langle T(L)_{21}^+ \rangle \right. \\ \left. 2 \sin\theta \sin\phi \right) \quad 2.31$$

$$I\eta_2 = -K \begin{Bmatrix} 1 & 1 & 2 \\ L & L & L_f \end{Bmatrix} 2i \langle T(L)_{11}^+ \rangle \sin\theta \sin\phi \quad 2.32$$

where  $K = \frac{1}{\gamma} \omega(L, L_f)$ . For  $n^1P$  state  $L=1$  and  $L_f=0$

$$\begin{Bmatrix} 1 & 1 & 2 \\ 1 & 1 & 0 \end{Bmatrix} = \frac{1}{3}$$

$$\begin{Bmatrix} 1 & 1 & 1 \\ 1 & 1 & 0 \end{Bmatrix} = -\frac{1}{3}$$

where  $I\eta_3$ ,  $I\eta_1$  and  $I\eta_2$  are as defined before.

From equations (2.24 to 28 and 2.29 to 31) one obtains  $\eta_3$ ,  $\eta_1$  and  $\eta_2$ , in terms of  $\lambda$  and  $\chi$  :

$$\eta_3 = \frac{I(0) - I(90)}{I(0) + I(90)} = 2\lambda - 1 \quad 2.33$$

$$\eta_1 = \frac{I(45) - I(135)}{I(45) + I(135)} = -2\sqrt{\lambda(1-\lambda)} \cos\chi \quad 2.34$$

$$\eta_2 = \frac{I(RHC) - I(LHC)}{I(RHC) + I(LHC)} = -2\sqrt{\lambda(1-\lambda)} \sin\chi \quad 2.35$$

In the present analysis of the circularly polarized light the spectroscopic definition of circular polarized light is used, which is the opposite to the helicity definition used by Blum and Kleinpoppen (1979) and for equation 2.35.

Thus in our case  $\eta_2$  will take the following form, Standage and Kleinpoppen (1976)

$$\eta_2 = +2\sqrt{\lambda(1-\lambda)} \sin\chi \quad 2.36$$

From the Stokes parameters some quantities can be derived which characterize the degree of "coherence" of the emitted light. Born and Wolf determined the coherence-correlated factor  $\mu$  and the degree of polarization  $P$  as follows

$$\mu_{zx} = |\mu_{zx}| e^{i\epsilon_{zx}} = \frac{\eta_1 + i\eta_2}{\sqrt{1 - \eta_3^2}} \quad 2.37$$

where

$\mu_{zx}$  is effectively a measure of the correlation between the x and z components of the electric vector of radiation.

$|\mu_{zx}|$  is a measure of the "degree of coherence" of the light.

$\epsilon_{zx}$  is the "effective phase difference" between the two components of the electric vector.

The magnitude of the vector  $\vec{P}$ , is defined as the "degree of polarization"

$$|\vec{P}| = \sqrt{\eta_1^2 + \eta_3^2 + \eta_2^2} \quad 2.38$$

For completely coherent light  $|\mu| = |P| = 1$ .

### 2.5. Angular Momentum Transfer

The angular momentum transfer  $\langle Ly \rangle$  to the atom during the collision has been discussed by Happer (1972), Fano and Macek (1973), Blum (1981), Madison and Winters (1981) and Beyer et al. (1982).

The initial electron photon angular correlation experiments of Eminyan et al. (1973 and 1974) on helium excited by 50-100 eV electrons derived clear evidence of the orientation magnitude, but not of its sign. Standage and Kleinpoppen (1976) measured a positive value for the angular momentum transfer at small scattering angles for observation of the circular polarization of the light emitted from the  $3^1P$  state of helium in a direction perpendicular to the scattering plane.

Happer (1972) described the anisotropic character of the excited states in terms of the alignment tensor  $A^{col}$  and the

orientation vector  $\vec{O}^{\text{col}}$  first introduced into atomic physics for optical pumping experiments. Their application to collision experiments has been described by Fano and Macek (1973). Madison and Winters (1981) confirmed that the orientation of the atoms should change sign when the scattering angle is changed from small to large values goes from small to large scattering angles. This was thought to be due to the change from attractive forces (dominant at small scattering angles) to repulsive forces (dominant at large scattering angles). Kohmoto and Fano (1981) used a simple classical grazing model to relate the attractive or repulsive nature of the interaction to the sign of the orientation produced.

Blum and Kleinpoppen (1979) have formulated the equivalent expressions for Fano and Macek (1973) to calculate the alignment parameters  $A^{\text{col}}$ ,  $A_{1+}^{\text{col}}$  and  $A_{2+}^{\text{col}}$  and the orientation vector  $O_{1-}^{\text{col}}$  in terms of the excitation parameters  $\lambda$  and  $\chi$  as follows:

$$A_0^{\text{col}} = \frac{\langle 3L_z^2 - L^2 \rangle}{L(L+1)} = \frac{1}{\sigma} \sqrt{\frac{3}{2}} \langle T(1)_{20}^+ \rangle = \frac{1}{2}(1-3\lambda) \quad 2.39$$

$$A_{1+}^{\text{col}} = \frac{\langle L_x L_z + L_z L_x \rangle}{L(L+1)} = \frac{1}{\sigma\sqrt{2}} \langle T(1)_{21}^+ \rangle = \sqrt{\lambda(1-\lambda)} \cos\chi \quad 2.40$$

$$A_{2+}^{\text{col}} = \frac{\langle L_x^2 - L_y^2 \rangle}{L(L+1)} = \frac{1}{\sigma\sqrt{2}} \langle T(1)_{22}^+ \rangle = \frac{1}{2}(\lambda-1) \quad 2.41$$

$$O_{1-}^{\text{col}} = \frac{\langle L_y \rangle}{L(L+1)} = \frac{i\langle T(1)_{11}^+ \rangle}{\sigma} = \sqrt{\lambda(1-\lambda)} \sin\chi \quad 2.42$$

In order to relate the behaviour of  $O_{1-}^{\text{col}}$  to the collision process within the semiclassical model two principle paths of the scattered electron are considered as shown in figure (2-4). In figure (2-4a),

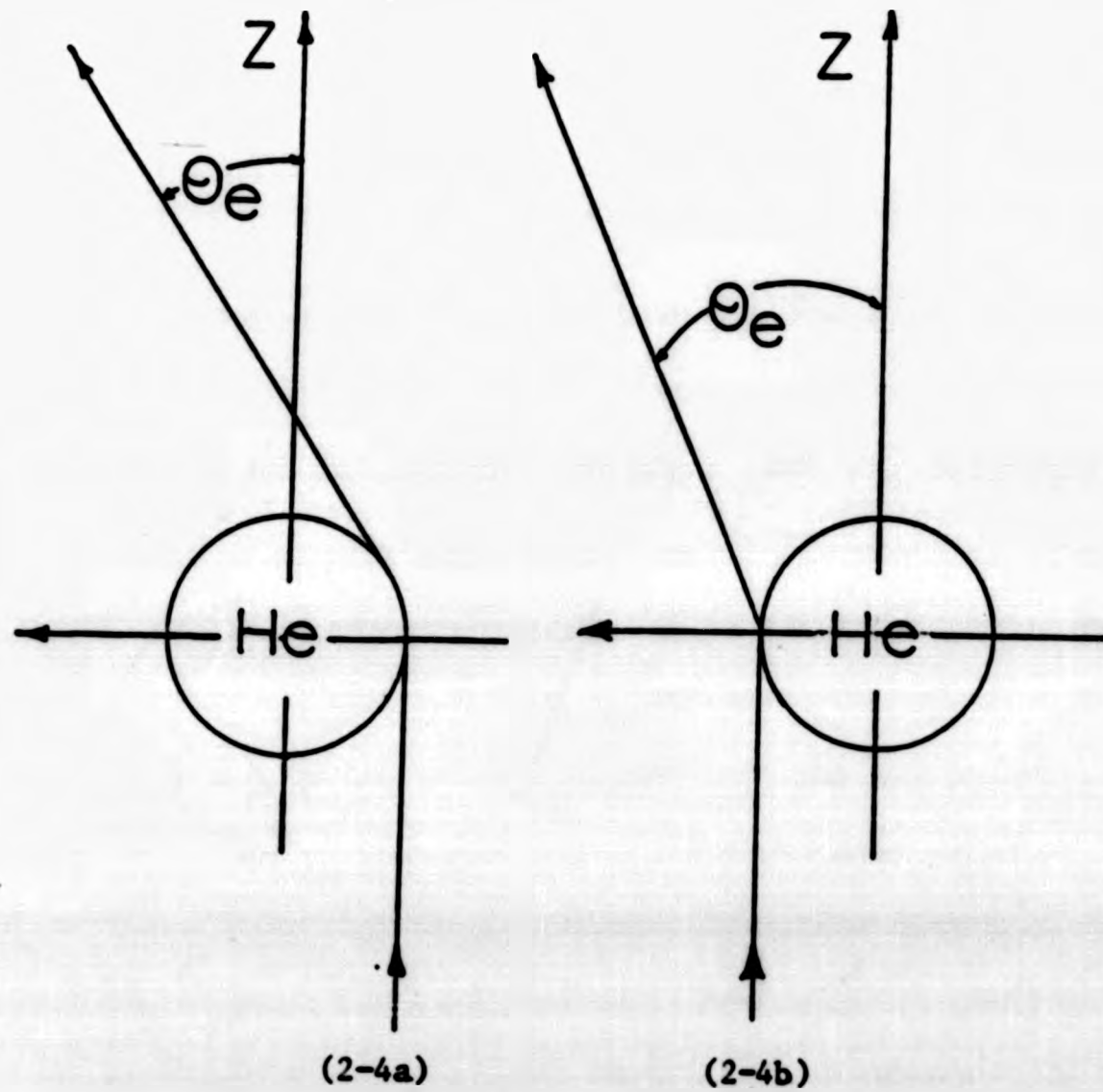


Figure (2-4): The two principal paths for semiclassical scattering of electrons for helium. (a) The electron is incident with a negative impact parameter and scatters from the attractive potential to the positive angle  $\theta_e$ , (b) The electron is incident with positive impact parameter and scatters from the repulsive potential of the helium electrons to the same positive angle  $\theta_e$ .

the electron approaches the helium atom with a negative impact parameter and is scattered by an attractive potential to a positive scattering angle. According to the semiclassical model the atom must obtain positive angular momentum perpendicular to the scattering plane, i.e.  $\langle L_y \rangle$  must lie along the positive direction of the y-axis. The equation  $\langle L_y \rangle = 2O_{1-}^{\text{col}}$  implies that the orientation is positive for this collision. In Figure (2-4b) the electron is incident with a positive impact parameter and is scattered by a repulsive potential into a positive scattering angle. In this case, the atom must obtain negative angular momentum which implies that  $O_{1-}^{\text{col}}$  is negative.

Thus the behaviour of  $O_{1-}^{\text{col}}$  can be explained by using the semiclassical model as follows. When the electron is scattered to  $\theta_e = 0^\circ$ , there is no change in the angular momentum of the atom perpendicular to the scattering plane. Therefore  $O_{1-}^{\text{col}}$  vanishes at  $\theta_e = 0^\circ$ . As the scattering angle increases from  $0^\circ$ , the amount of angular momentum transferred to the atom perpendicular to the scattering plane,  $\langle L_y \rangle$ , increases. Since the dominant scattering potential for small angles is the long-range attractive potential due to atomic polarizability,  $\langle L_y \rangle$  is positive. Thus,  $O_{1-}^{\text{col}}$  is positive and increases towards its extrema value of 0.5. However, as the scattering angle continues to increase, the impact parameter decreases and scattering from the repulsive potential of the helium electrons begins to become significant. Since the sign of the angular momentum transfer due to repulsive scattering is opposite to that for attractive scattering, these processes compete and the value of  $O_{1-}^{\text{col}}$  may or may not reach the value of 0.5 before it decreases with  $\theta_e$ . Then at some values of  $\theta_e$  where the contributions from the two types of scattering are equal in magnitude,  $O_{1-}^{\text{col}}$  vanishes. As  $\theta_e$  increases from this angle the repulsive scattering becomes dominant and  $O_{1-}^{\text{col}}$  becomes negative and decreases to another extrema. As  $\theta_e$  increases

further, the transfer of angular momentum perpendicular to the scattering plane again decreases until at  $\theta_e = 180^\circ$ ,  $O_{1-}^{col}$  vanishes.

The change in the sign of the orientation has been discussed along the line of the classical grazing model by Beyer et al. (1982) who assumed four classical paths for the scattered electron as shown in the figure (2-5). Electrons scattered through  $\theta$  to the left (C and B by either a repulsive or an attractive force are detected by the electron detector at  $+\theta_e$ . Similarly, those electrons scattered to the right (D and E) are incident on a detector at  $-\theta_e$ . According to this model, all electrons passing on the left side will produce a negative orientation of the excited atom,  $\langle Ly \rangle < 0$ , and all electrons passing on the right side a positive orientation  $\langle Ly \rangle > 0$ . The sign of the orientation can be experimentally determined by observing the scattered electrons in coincidence with either left-handed or right-handed circularly polarized light (Stokes parameter  $\eta_2$ ) emitted in the y-direction. The probabilities of electrons to be scattered through  $+\theta_e$ , and  $-\theta_e$  with the emission of left-hand circularly polarized light can be represented by paths C and E respectively. The corresponding paths B and D represent the probabilities for electrons to be scattered through  $+\theta$  and  $-\theta$ , respectively, with the emission of right-hand circularly polarized light. In both cases the emitted light is in y-direction.

According to these definitions the results of four possible experiments involving coincidence detection of electrons and circularly polarized photons can be written, using the Stokes parameters

$$\eta_2 = (I_{RHC} - I_{LHC}) / (I_{RHC} + I_{LHC}) = - \langle Ly \rangle \quad 2.43$$

The measurement of the circular polarization Stokes parameter  $\eta_2$  is given by

$$\eta_2(+\theta) = \frac{B-C}{B+C} \quad \text{and} \quad \eta_2(-\theta) = \frac{D-E}{D+E} \quad 2.44$$

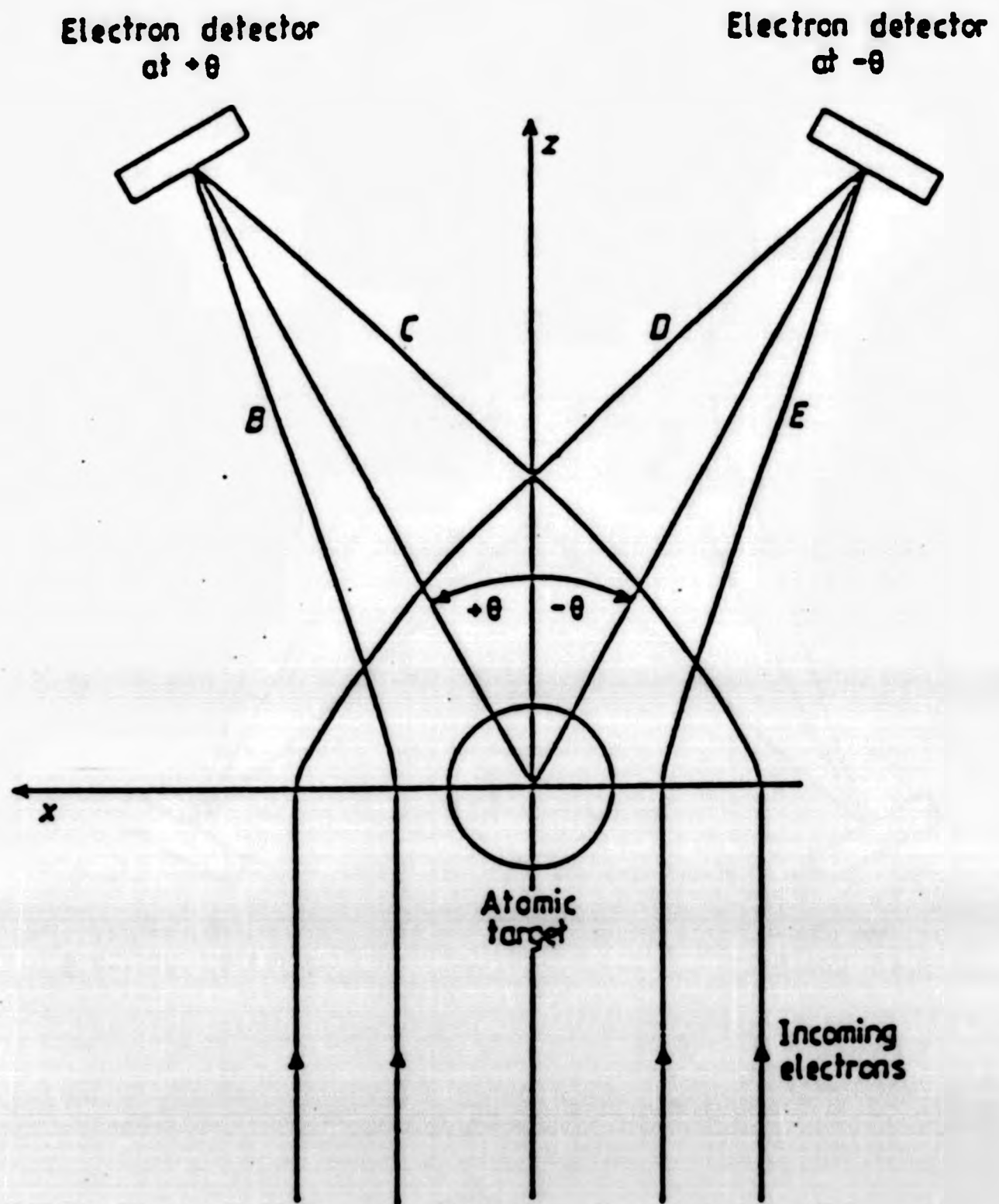


Figure2-5: Classical electron trajectories for scattering angles  $\pm\theta$  for attractive and repulsive forces, (Beyer et al. (1982)).

Measurements of the right-left electron scattering asymmetry in coincidence with right or left hand circularly polarized light, can be written as follows

$$A_{\text{RHC}} = \frac{D-B}{D+B}, \quad A_{\text{LHC}} = \frac{E-C}{E+C} \quad 2.45$$

The parity invariance with respect to reflection in the scattering plane, requires that  $B = E$  and  $C = D$ . Using this symmetry, we find that

$$\eta_2(+\theta) = -\eta_2(-\theta) \quad 2.46$$

$$A_{\text{RHC}} = -\eta_2(+\theta) \quad 2.47$$

$$A_{\text{LHC}} = +\eta_2(+\theta) \quad 2.48$$

The change in sign of the circular polarization when going from small to large scattering angles means that, at small scattering angles  $C > B$  whereas at large scattering angles  $B > C$ .

According to this model the scattering process can be described by a repulsive amplitude related to  $B$  and an attractive amplitude related to  $C$ .

CHAPTER III

THE APPARATUS

3.1 Introduction

The apparatus consists of a vacuum chamber (650 mm long with 350 mm internal radius) as shown in figure (3-1), pumped by an oil diffusion pump. The experimental set-up and the associated feed-throughs are all mounted on one of the 500 mm  $\phi$  end flanges. The turntable assembly shown in figures (3-2 and 3-3) has a diameter of 310 mm  $\phi$  and was made of non-magnetic stainless steel. It is fixed to the end flange inside the excitation chamber and aligned to the centre of the flange. A  $127^\circ$  electron energy analyser (figures (3-4, 3-5 and 3-6)), a photon detector (figure (3-7)) and a Faraday cup (figure (3-8)) are fixed on the three turntable layers.

An electron gun is fixed on the base plate of the turntable. All these components are connected to the associated electrical systems outside the excitation chamber through a variety of feed-throughs. Two new distribution panels with voltage dividers were built, one to adjust the voltages of the electron gun and the other to adjust the electron analyser.

To extend the measurements beyond the angular correlation studies for which the system had originally been built, a new optical system (figure (3-13)) had to be added for the polarization correlation measurements where the light is observed in a direction perpendicular to the scattering plane. Therefore a photomultiplier together with an interference filter, a linear polarizer and a quarter wave plate were mounted outside the vacuum on the end flange, while an optical lens (50 mm  $\phi$ ,  $f = 75$  mm) to collect the emitted light from the interaction region, was fixed to the base of the turntable assembly. A quartz window was mounted on the 500 mm  $\phi$  flange

opposite to the turntable flange.

The vacuum system, the  $127^\circ$  electron analyser, the electron gun, the optical system, the photon detectors, and the potential distribution panels will be described below in more detail, while the excitation chamber, the Faraday cup and the turntable assembly were described in detail elsewhere (Malik, 1980).

### 3.2. Vacuum System

The vacuum system consists of a cylindrical stainless steel chamber, 650 mm long with an internal diameter of 350 mm, a diffusion pump and a rotary pump. Figure (3-1) shows a schematic diagram of the vacuum system.;

The chamber was pumped by a four stage oil diffusion pump (Leybold Heraeus Model D1 3000) with a nominal pumping speed of  $3000 \text{ l.s}^{-1}$  for air, and a large rotary (Piston vacuum) pump (Edwards model ES2000) with a pumping speed of  $126 \text{ m}^3\text{h}^{-1}$ . Since we detected nonconductive brown deposits on the surface of the electrodes of the electron gun, and since there were also signs of some minor oil condensation, it was decided to switch to a pump which was considered to be "cleaner".

In most of the present work the vacuum chamber was pumped first of all by a single stage rotary pump (Edwards Model ES200) and an oil diffstak pump (Edwards Model 160/700) with an integrated water baffle. In addition the pump is baffled with a freon cooled baffle. The pumping speed of the diffstak pump is  $700 \text{ l/sec}$  for air, according to the manufacturer.

The vacuum chamber could be isolated from the diffusion pump by an electro-pneumatically operated gate valve (VAT). This could be closed so that the diffusion pump could remain switched on and the

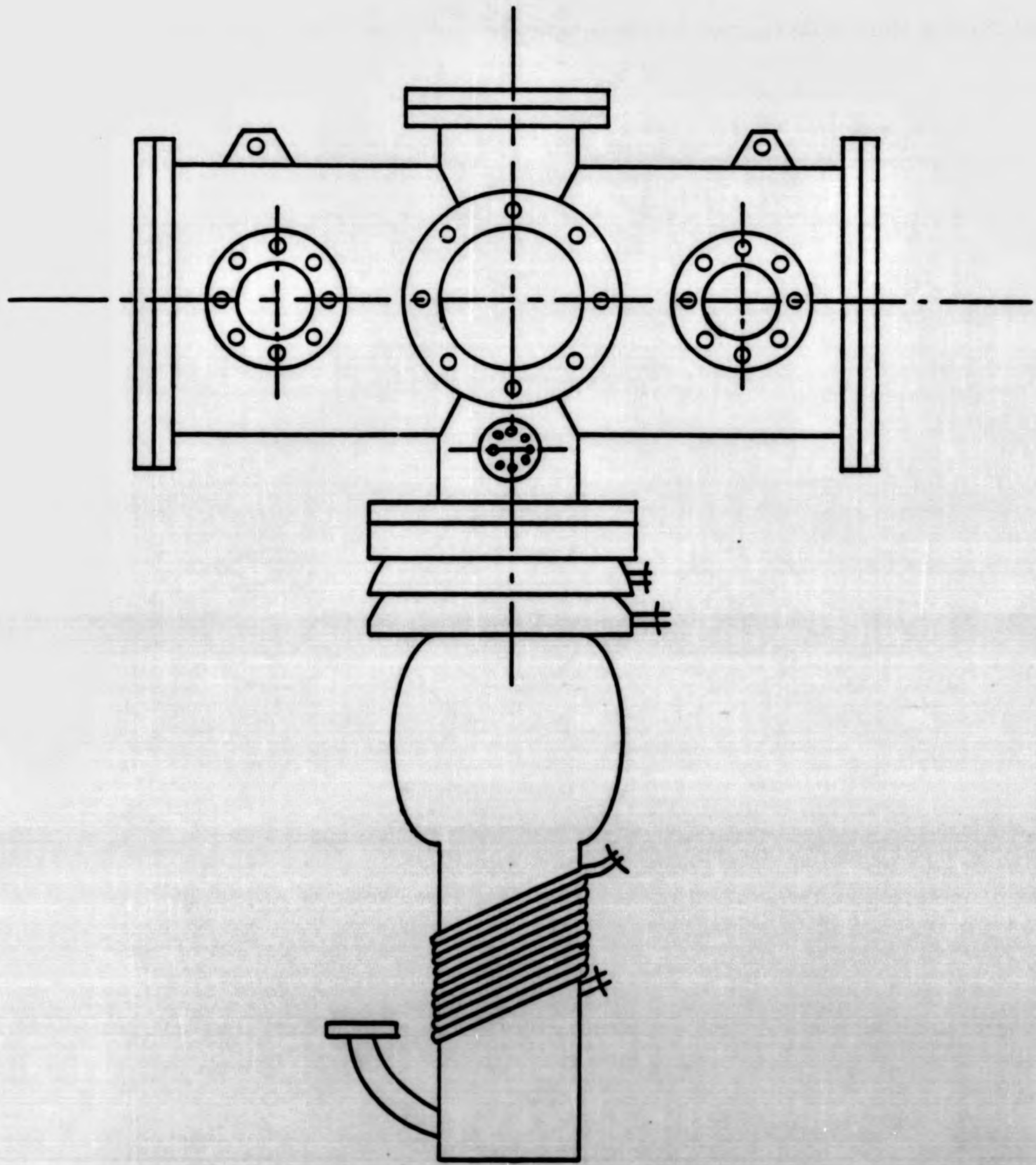


Figure (3-1): Schematic diagram of vacuum system.

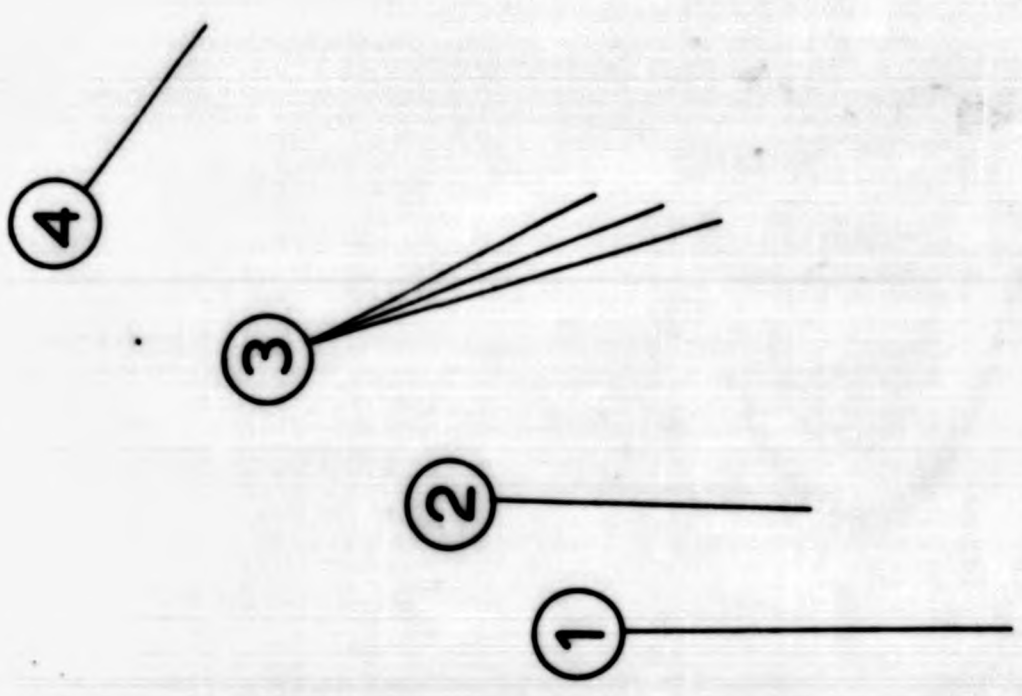
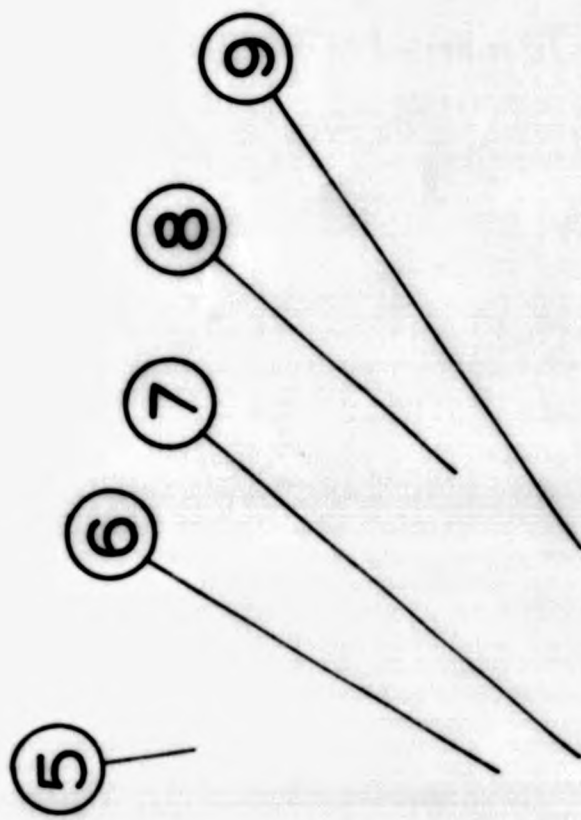


Figure (3-1)

Figure (3-2)

View of the interior of the aperture

1. Flange 500mm $\phi$
2. Rubber gasket
3. Turntable assembly
4. Lens holder
5. Optical lens 50mm $\phi$
6. Electron gun
7. Helium beam nozzle
8. 127 $^{\circ}$  electron analyser assembly
9. Faraday cup.

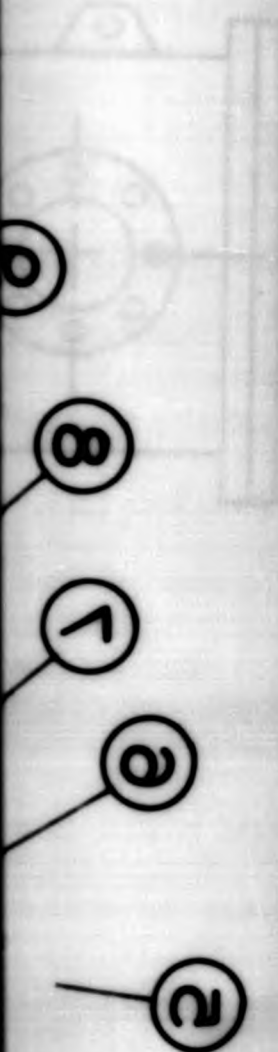
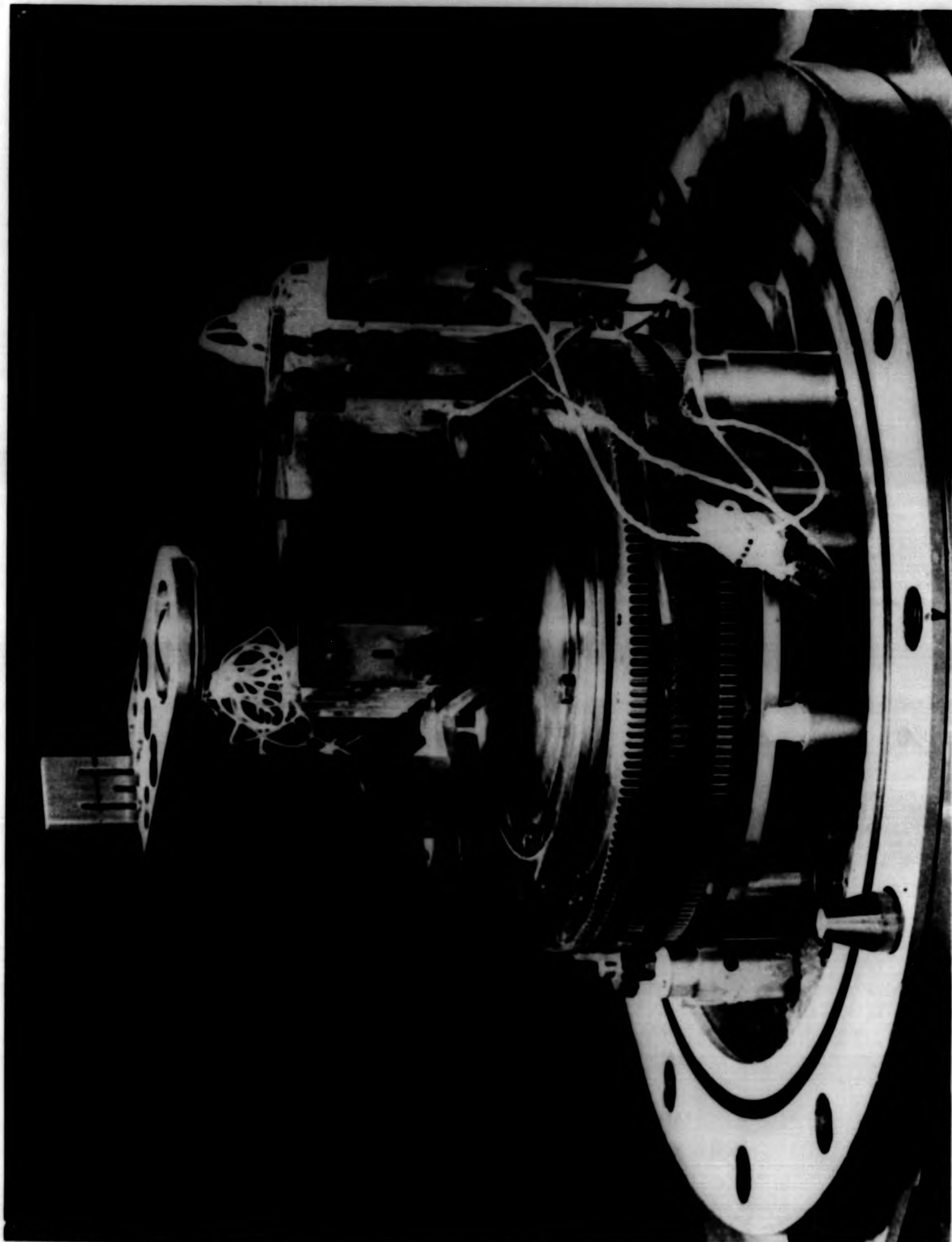


Figure (3-2)

View of the interior of the aperture

1. Flange 500mm $\phi$
2. Rubber gasket
3. Turntable assembly
4. Lens holder
5. Optical lens 50mm $\phi$
6. Electron gun
7. Helium beam nozzle
8. 127 $^{\circ}$  electron analyser assembly
9. Faraday cup.

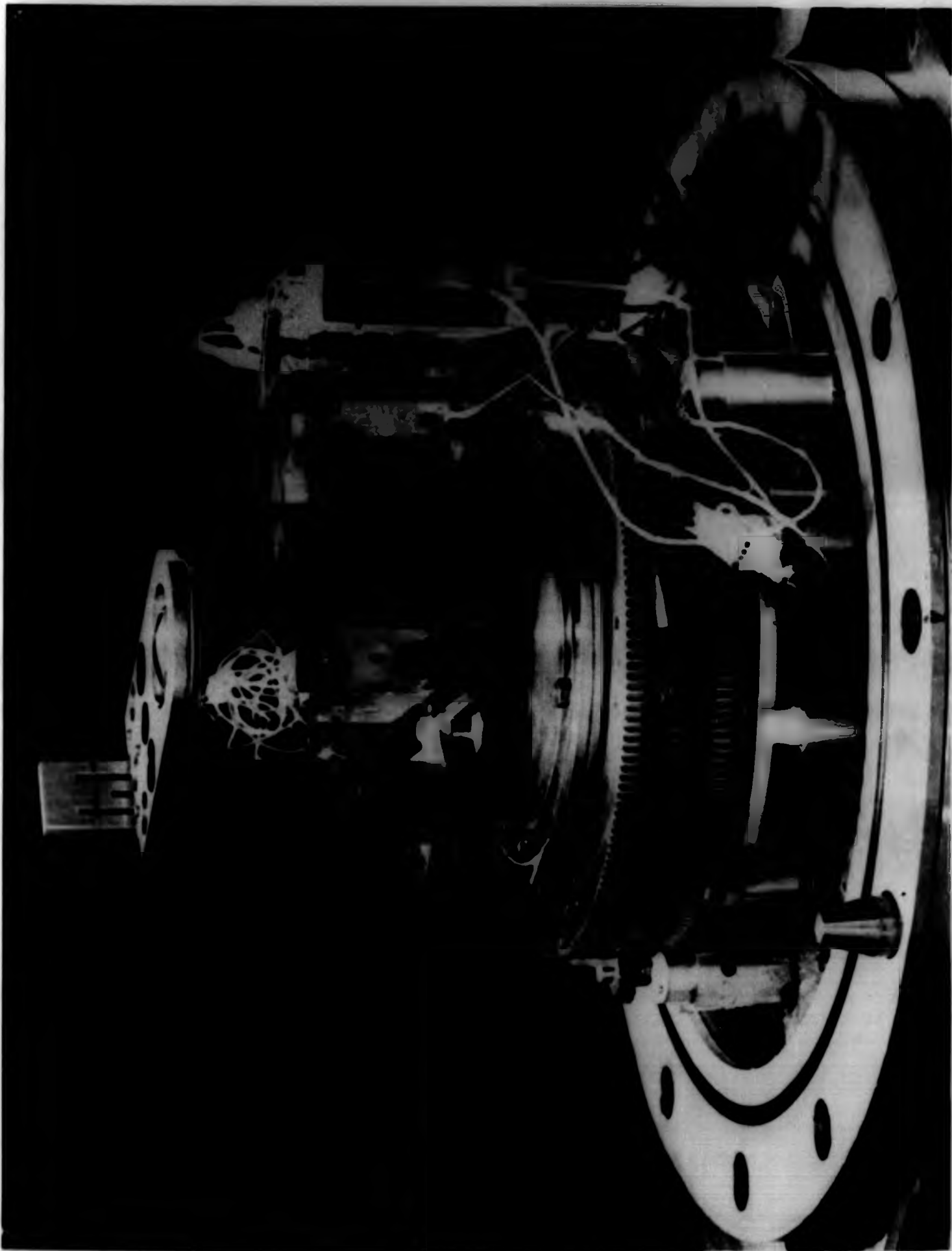
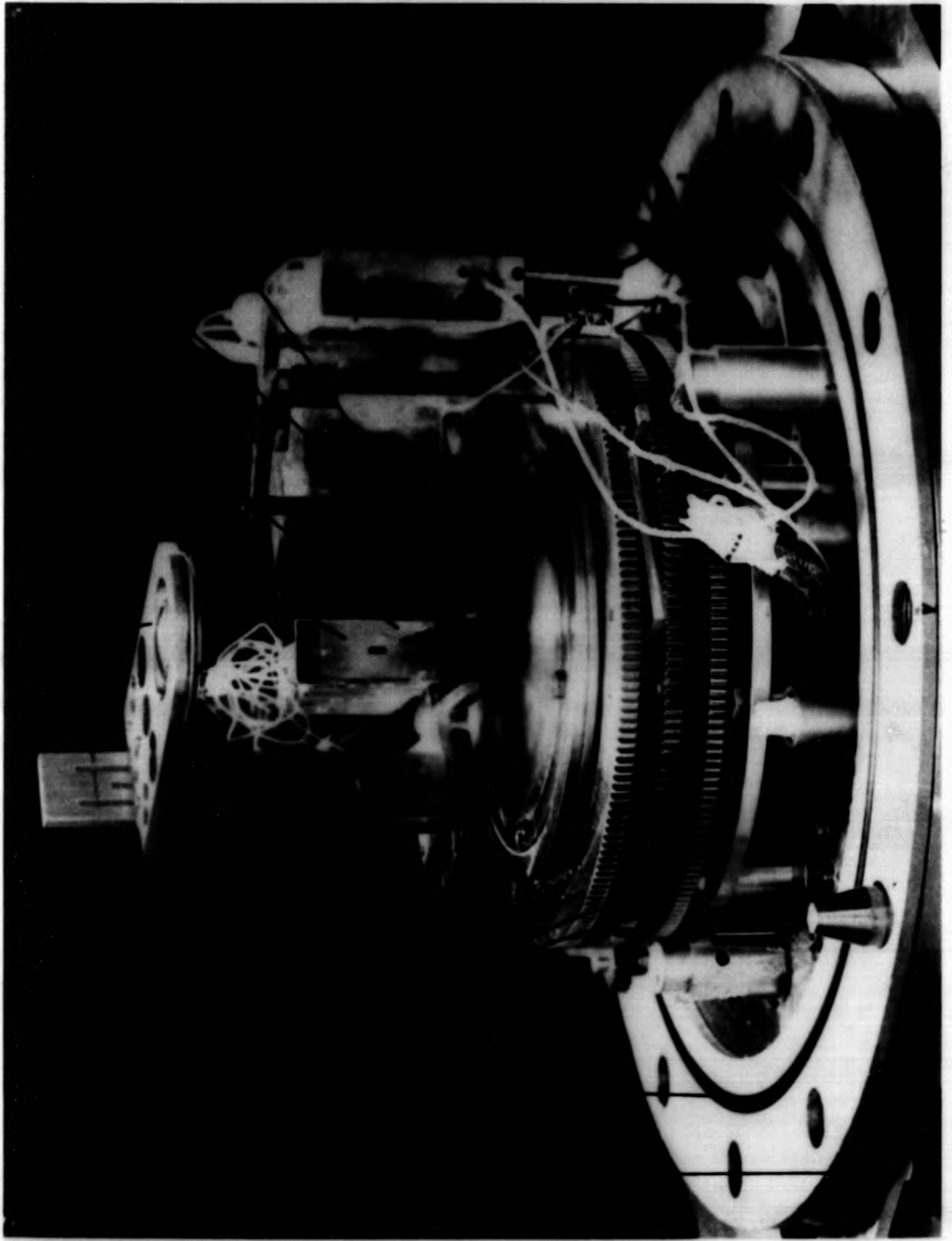


Figure (3-2)

View of the interior of the aperture

1. Flange 500mm $\phi$
2. Rubber gasket
3. Turntable assembly
4. Lens holder
5. Optical lens 50mm $\phi$
6. Electron gun
7. Helium beam nozzle
8. 127° electron analyser assembly
9. Faraday cup.



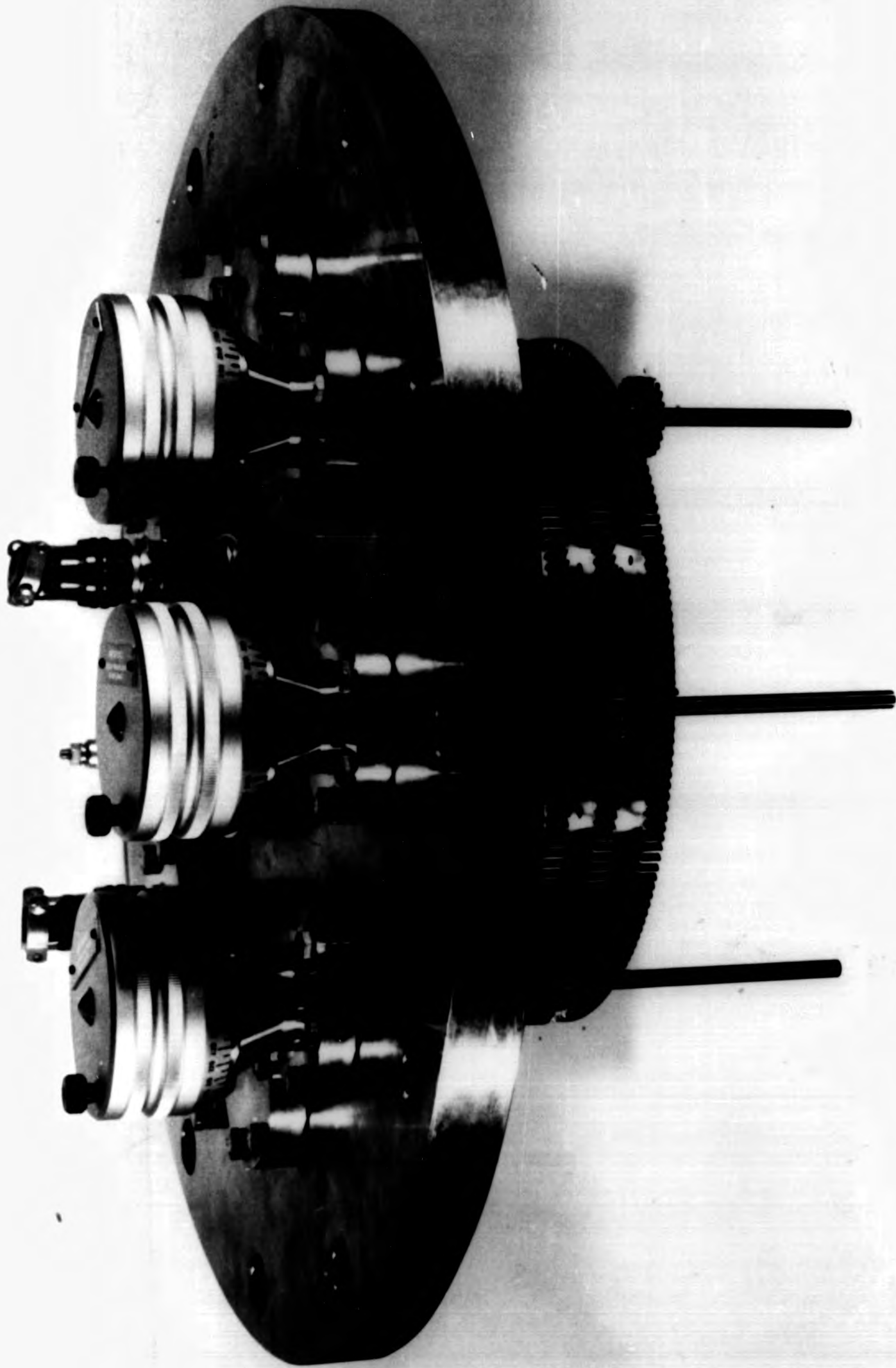


Figure (3-3): The Triple Turntable Assembly

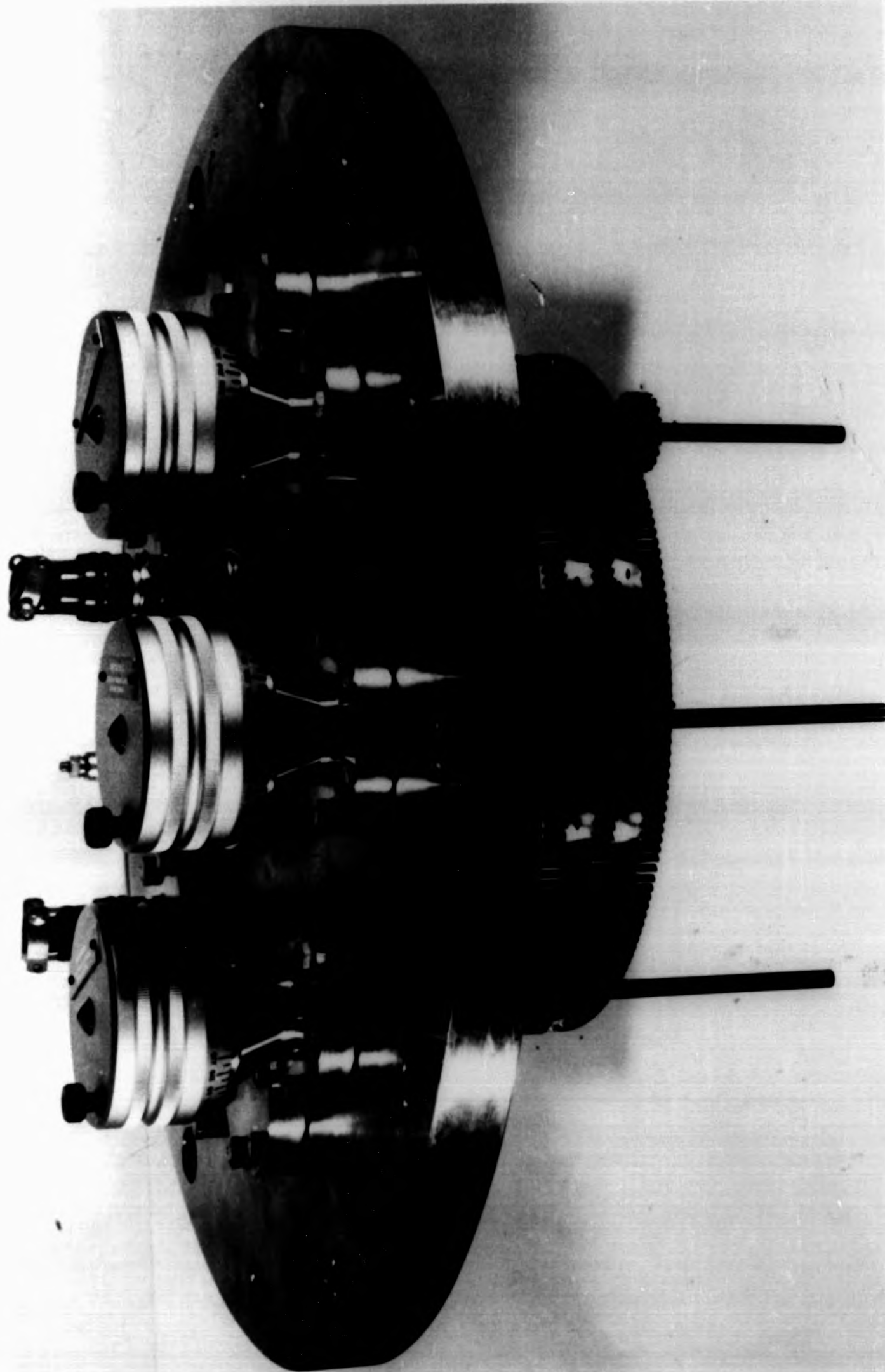


Figure (3-3): The Triple Turntable Assembly

time of cooling and reheating of the pump be saved. The base pressure of the system was approximately  $1 \times 10^{-7}$  Torr.

The effective pumping speed has been calculated, according to equation (3.1), for the old diffusion pump and the one used in the present work

$$S_{\text{eff}} = \frac{S}{1 + \frac{s}{C_i}} \quad 3.1$$

where  $S$  is given in  $\text{l sec}^{-1}$  and  $C_i$  represent the total baffles conductance of the baffles. The results for the two oil pumps are compared in table (3-1)

Table 3-1

No	Oil Pump	Model	$S_{\text{eff}}$ for Air
1	Oil diffusion pump	Teybold Haraeus D13000	860
2	Oil diffusion pump (Used in present experiments)	Edwards 160/700	540

### 3.3. The 127° Electron Analyser

Two main types of monochromators have been used in electron-atom scattering experiments. The 'hemispherical' type with a deflection angle of  $180^\circ$  was introduced by Simpson and Kuyatt (Simpson 1964; Kuyatt and Simpson, 1967). The cylindrical type with a deflection angle of  $127^\circ$  was first used by Clark (1954) and later improved by Marmet and Kerwin (1960). Many improvements have since been made for the cylindrical type, by Andrick and Ehrhardt (1966) and Gibson and Dolder (1969). In this experiment, the

cylindrical type with a deflection angle of  $127^\circ$  was used as the electron analyser.

The theory of the  $127^\circ$  cylindrical analyser was first developed by Hughes and Rojansky (1929) who showed that a beam of electrons entering the cylindrical field through a slit and having a small beam divergence  $\alpha$  with respect to the slit normal, is focussed at an angle of  $\sqrt{\frac{\pi}{2}} = 127^\circ 17'$ .

Figure (3-4) shows the electron trajectories between a pair of  $127^\circ$  concentric cylinders of radii  $r_1$  and  $r_2$  ( $r_1 < r_2$ ) with mean potential (and electron energy)  $E_0$ , where  $E_0 = eV_0$ .

The electric field inside the analyser due to potentials  $V_1$  and  $V_2$  at radius  $r$  is given by

$$E(r) = \frac{V_1 - V_2}{2\ln \frac{r_2}{r_1}} \frac{1}{r} \quad 3.2$$

where  $r_1$  and  $r_2$  are the radii of the inner and outer cylinders respectively and  $r = \frac{r_1 + r_2}{2}$  is the mean radius.

The potential  $V_0$  at the central orbit is given by

$$V_0 = \frac{V_1 - V_2}{2\ln \frac{r_2}{r_1}} \quad 3.3$$

It can be shown that the potential at the inner grid is:

$$V_1 = V_0 \left( 1 + 2\ln \frac{r_2}{r_1} \right) \quad 3.4$$

and at the outer grid is:

$$V_2 = V_0 \left( 1 + 2\ln \frac{r_1}{r_2} \right) \quad 3.5$$

The general transmission function of an analyser is given by Delege and Cavette (1971)

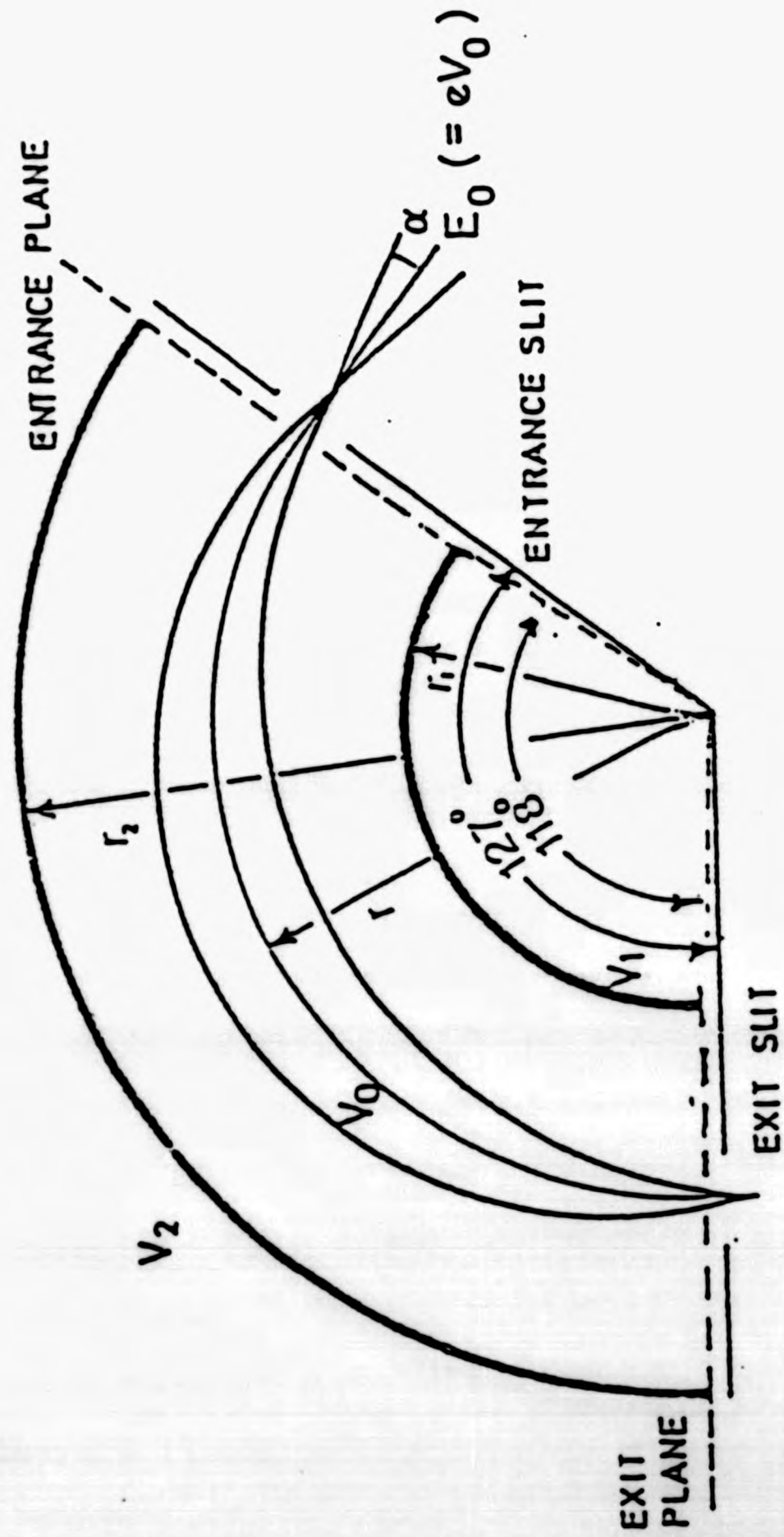


Figure (3-4): Electron trajectories in a  $127^\circ$  cylindrical analyser

$$\frac{\Delta r}{r} = A \frac{\Delta E}{E_0} + B\alpha^2 + C\beta^2 \quad 3.6$$

where  $r$  is the radius of the central path of the electrons through the analyser ( $r = \frac{r_1 + r_2}{2}$ ),  $\Delta r$  is the slit width,  $E_0$  is the mean energy,  $\Delta E$  is the energy spread measured in terms of the full width at half maximum intensity,  $\alpha$  is the angular divergence of the beam in the horizontal plane (figure 3-4) and  $\beta$  is the corresponding angle perpendicular to this plane. A, B and C are constants which have different values for various analysers.

For a  $127^\circ$  cylindrical analyser

$$A = 1, \quad B = \frac{4}{3}, \quad \text{and } C = 1 \quad 3.7$$

Thus the energy resolution for such an analyser is

$$\frac{\Delta E}{E_0} = \frac{\Delta r}{r} + \frac{4}{3} \alpha^2 + \beta^2 \quad 3.8$$

One of the experimental problems which had to be solved before the energy resolution of the  $127^\circ$  monochromator could be fully exploited was the elimination of those electrons hitting the surface of the cylinders, where some could be reflected so that they would be transmitted by the exit slit. Even if these electrons did not leave the analyser through the slits their space charge could distort the path of the other electrons. Marmet and Kerwin (1960) solved this problem by using high transparency grids instead of solid metal for the cylinders, so that the unwanted electrons would be transmitted and could be removed by a collector electrode placed behind the grids.

The  $127^\circ$  electron analyser used in the present work (shown in figure(3-5)) was built along the lines outlined by Marmet and Kerwin (1960). The total height of the cylinders is 62.5mm. The other

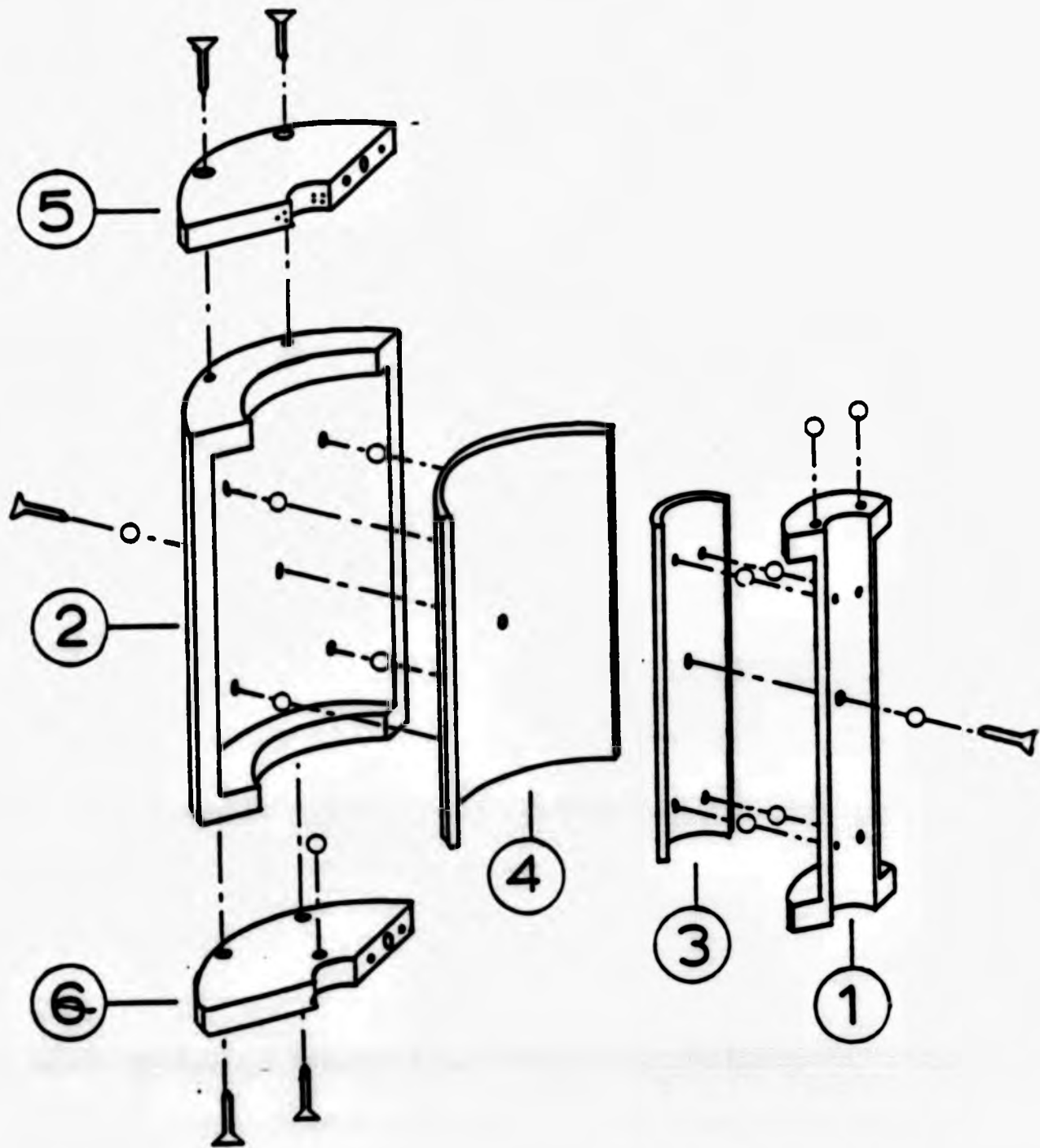


Figure (3-5):

127° Electron energy analyser

1 and 2 Inner and outer grid frame

3 and 4 Inner and outer plates

5 and 6 Assembly sections

O Ruby balls.

dimensions of the analyser are as follows. (For some details see Malik, 1980):

Radius of the inner grid	=	9.725 mm
" " " outer grid	=	14.750 mm
Mean Radius r	=	12.2375 mm
Radius of the inner collector	=	6.125 mm
" " " outer collector	=	20.80 mm
Slit width [Entrance]	=	1 mm
Slit length [Entrance]	=	10.0 mm
Slit width [Exit]	=	0.4 mm
Slit length [Exit]	=	10.0 mm

The insulation between grids was achieved by four 1.6 mm $\phi$  ruby balls placed on each grid structure and holding the plates by stainless steel screws passing through ceramic tubes. The analyser was isolated from the input and output slits which formed part of the analyser input and output optics by means of 2.4 mm $\phi$  ruby balls placed between the input (and output) slits and the top and bottom sides of the analyser. The field section was 118 $^{\circ}$  and not 127 $^{\circ}$  to minimize the effect of fringing field at the input planes of the analyser.

Figure (3-6) shows a schematic diagram of the whole analyser assembly with associated input and output optics.

#### 3.4. The Electron Gun Assembly

The electron gun used was designed according to the principle described by Simpson and Kuyatt (1963), and Harting and Read (1976).

When the mutual repulsion of electrons in a beam is taken into account, it is found that there is a maximum amount of current which is proportional to the three-halves power of the electron energy. When the volume is defined by two apertures of diameter d

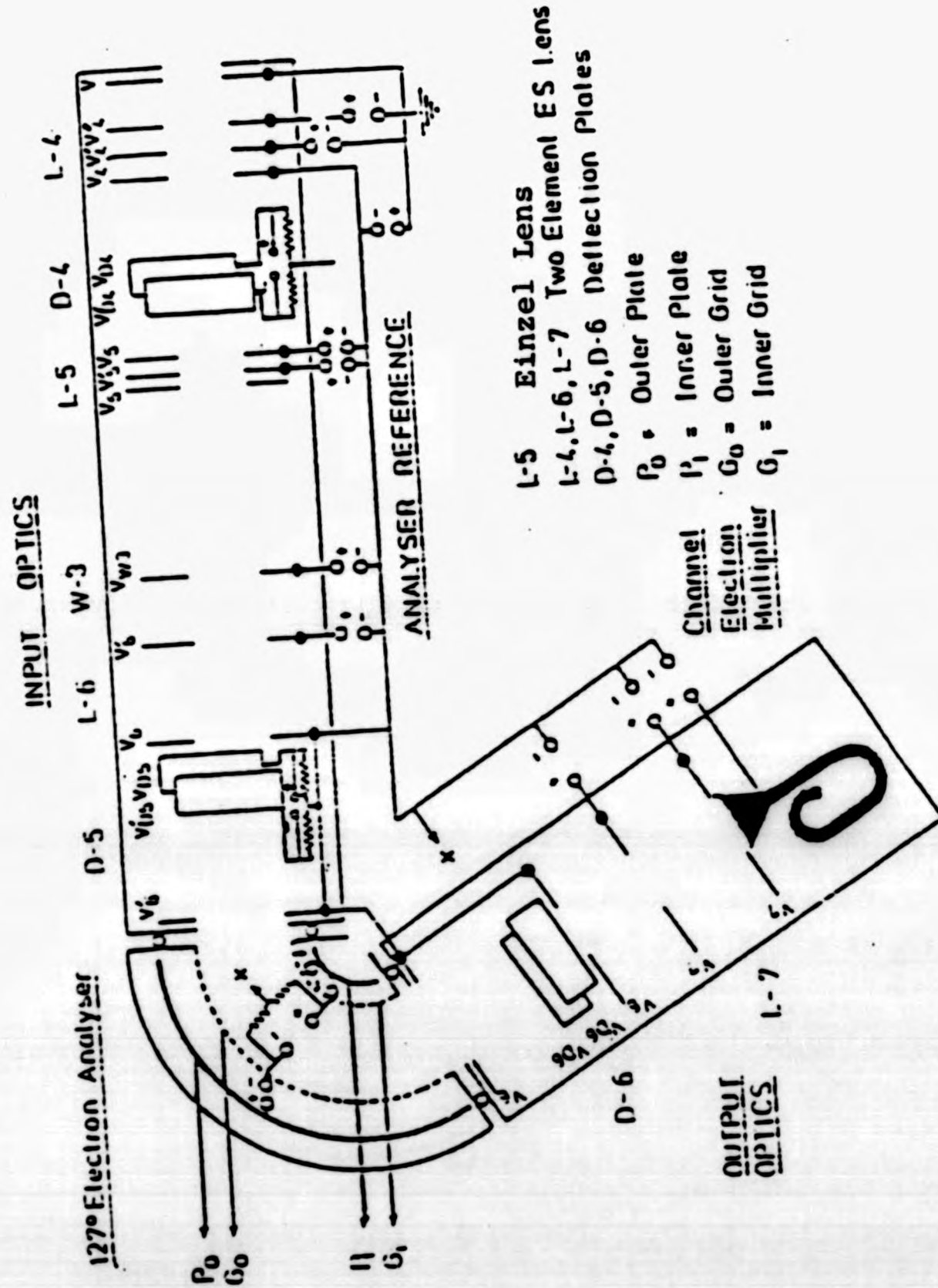


Figure (3-6): Schematic Diagram of Analyser Assembly

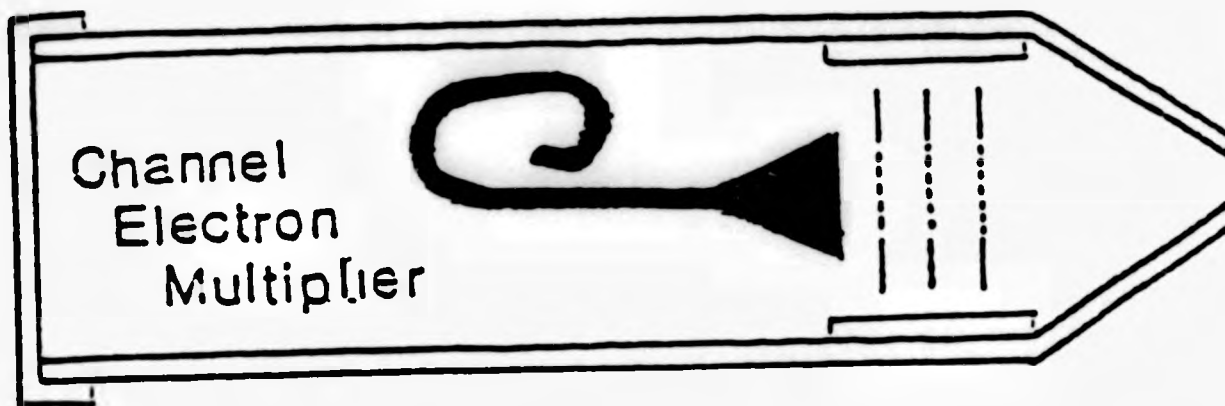


Figure (3-7): Channel electron multiplier with biasing grids used as a photon detector (angular correlation measurements).

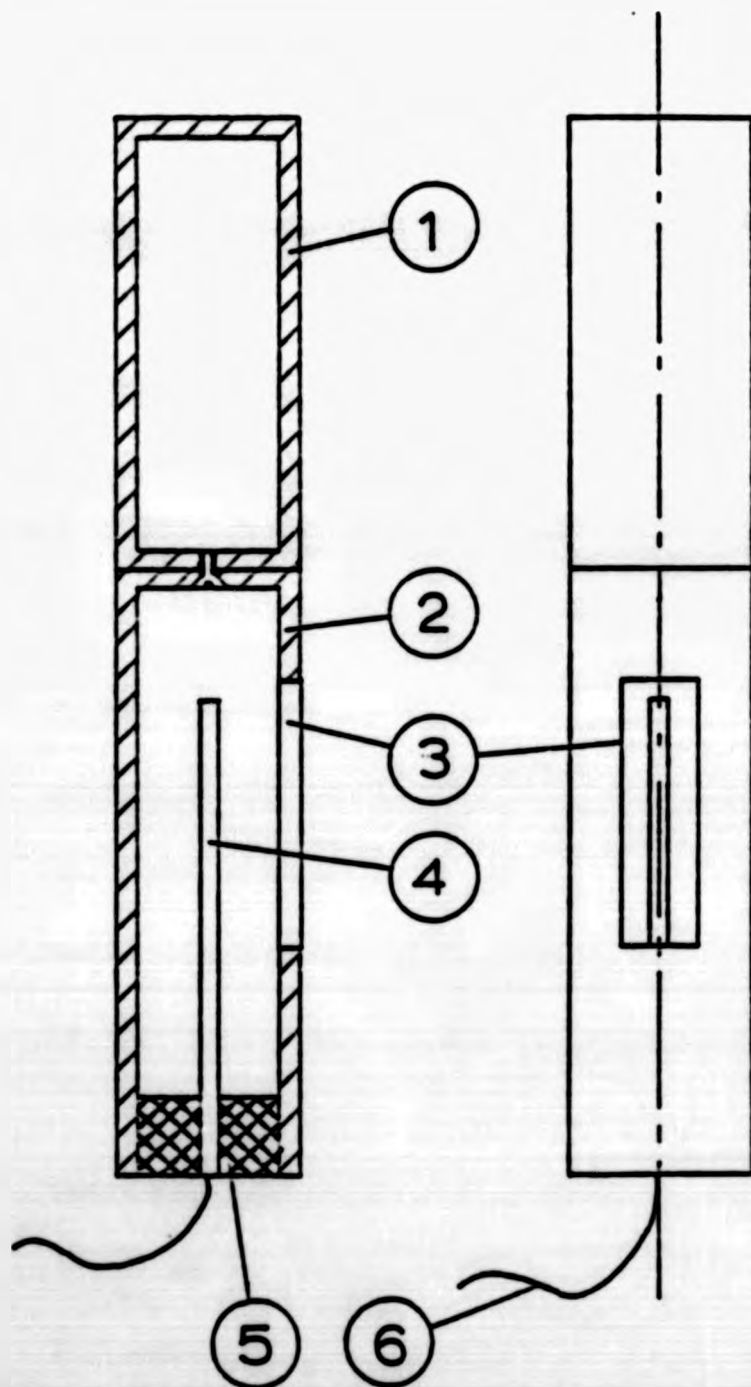


Figure (3-8):

Schematic diagram of the Faraday cup

(a) Section view,  
(b) Front view.

1. Cylindrical holder  
45 mm length and 10mm $\phi$ .
2. Cylinder 30 mm length  
and 10 mm $\phi$
3. Slit 14 mm length  
and 2 mm width
4. Collector 1 mm $\phi$
5. Insulator
6. Collector connection.

separated by a distance  $l$  as shown in figure (3-9) the maximum current which can be transmitted is given by (Simpson and Kuyatt 1963),

$$I_{\max} = 38.5E^{\frac{3}{2}} \left( \frac{d^2}{l^2} \right) \quad 3.9$$

where,  $I_{\max}$  is in  $\mu\text{A}$  and  $E$  is in eV, (and  $d$  and  $l$  in mm). To obtain this maximum current, the electron beam must enter the volume so that in the absence of space charge the beam would focus to a point at the centre of the volume. In the presence of space charge, the profile has a shape as shown in figure (3-9) with a minimum diameter.

The electron gun assembly consisted of four stages. The first stage (extraction stage) was formed by the cathode, a grid and the anode, and the other three stages lens systems to control the intensity and direction of the electron beam. They consisted of three electrostatic einzel lenses L-1, L-2 and L-3 and three pairs of deflection plates D-1, D-2 and D-3.

This arrangement of the electron gun was found when the system was taken over. It was working well for the electron energy of 80 eV, but for lower energies the electron beam tended to be unstable and to split into double beams even shortly after the whole gun had been cleaned. It was therefore decided to reduce the number of small apertures, which are particularly likely to be contaminated, by removing the final stage of the gun.

The new three-stage arrangement of the electron gun which has been used in the present work is shown in figure (3-10 and 3-11). The first stage (extraction stage) is formed by cathode, grid and anode, the second stage is the acceleration and beam forming stage, whereas the third one is a deceleration stage.

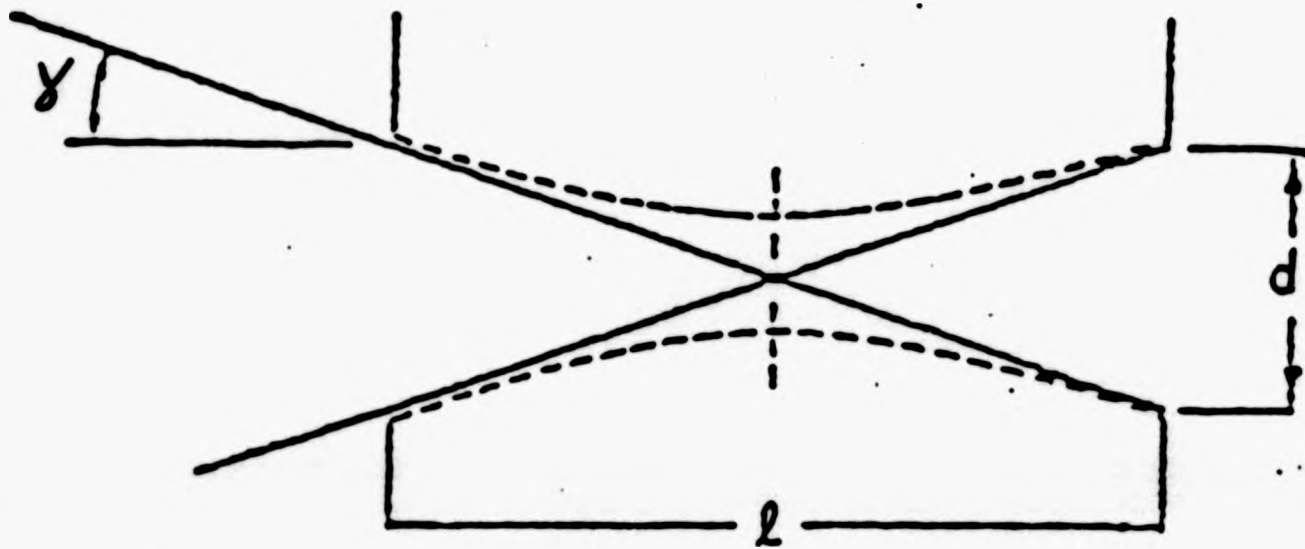


Figure (3-9): Dashed lines show ideal space charge limited beam profile required to saturate a given space.

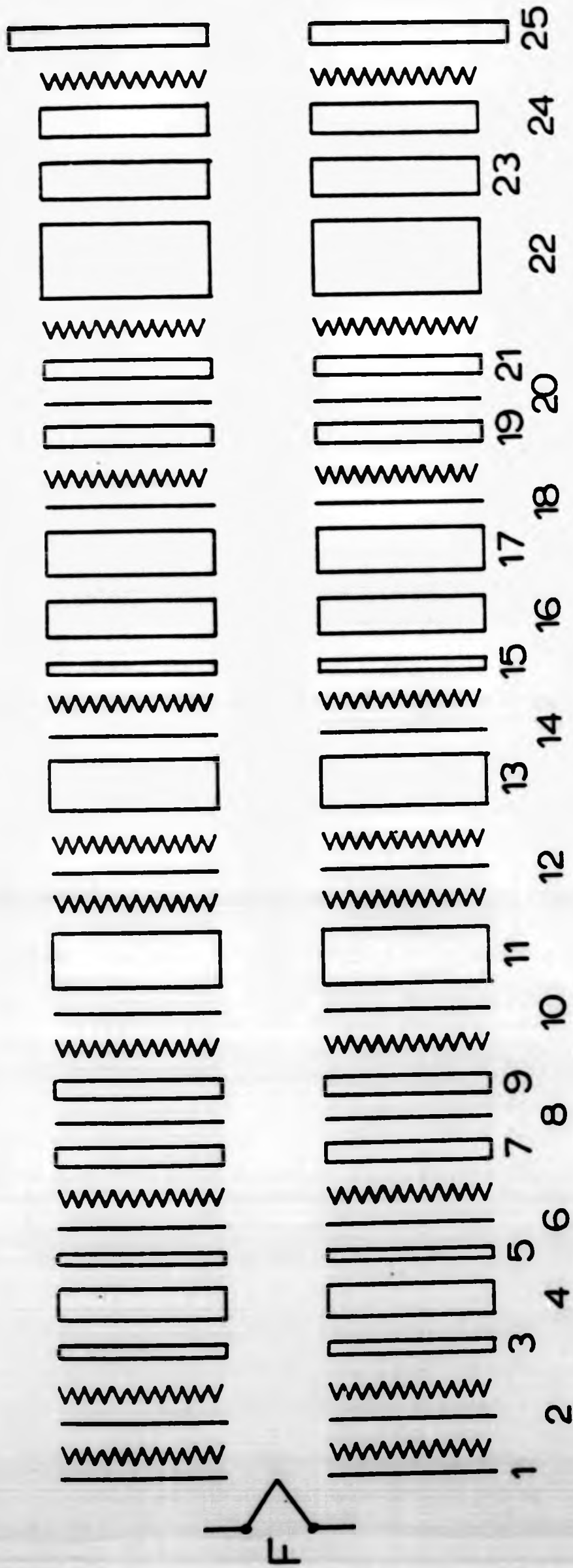


Figure (3-10): Graphical layout of the electron gun assembly showing the arrangement of the electrodes, dimensions (x and y) of the apertures, thickness of the spacer and deflection plates in mm.

- |                     |                     |                      |  |
|---------------------|---------------------|----------------------|--|
| 1. Aperture 0.4 x 5 | 5. Spacer 1.25      | 9. Spacer 2.9        | 13. Spacer 7.9                                 |
| 2. Aperture 0.4 x 5 | 6. Aperture 5 x 10  | 10. Aperture 5 x 10  | 14. Aperture 0.8 x 8                           |
| 3. Spacer 1.25      | 7. Spacer 2.9       | 11. Spacer 8.9       | 15. Spacer 1.9                                 |
| 4. D. plate 6       | 8. Aperture 5 x 10  | 12. Aperture 0.4 x 5 | 16. D. plate 6                                 |
|                     | 17. Spacer          | 21. Spacer 3.4       | 25. Front plate facing the interaction region. |
|                     | 18. Aperture 5 x 10 | 22. Spacer 12        |  |
|                     | 19. Spacer 8.4      | 23. D. plate 6       |  |
|                     | 20. Aperture 5 x 10 | 24. Spacer 5         |  |

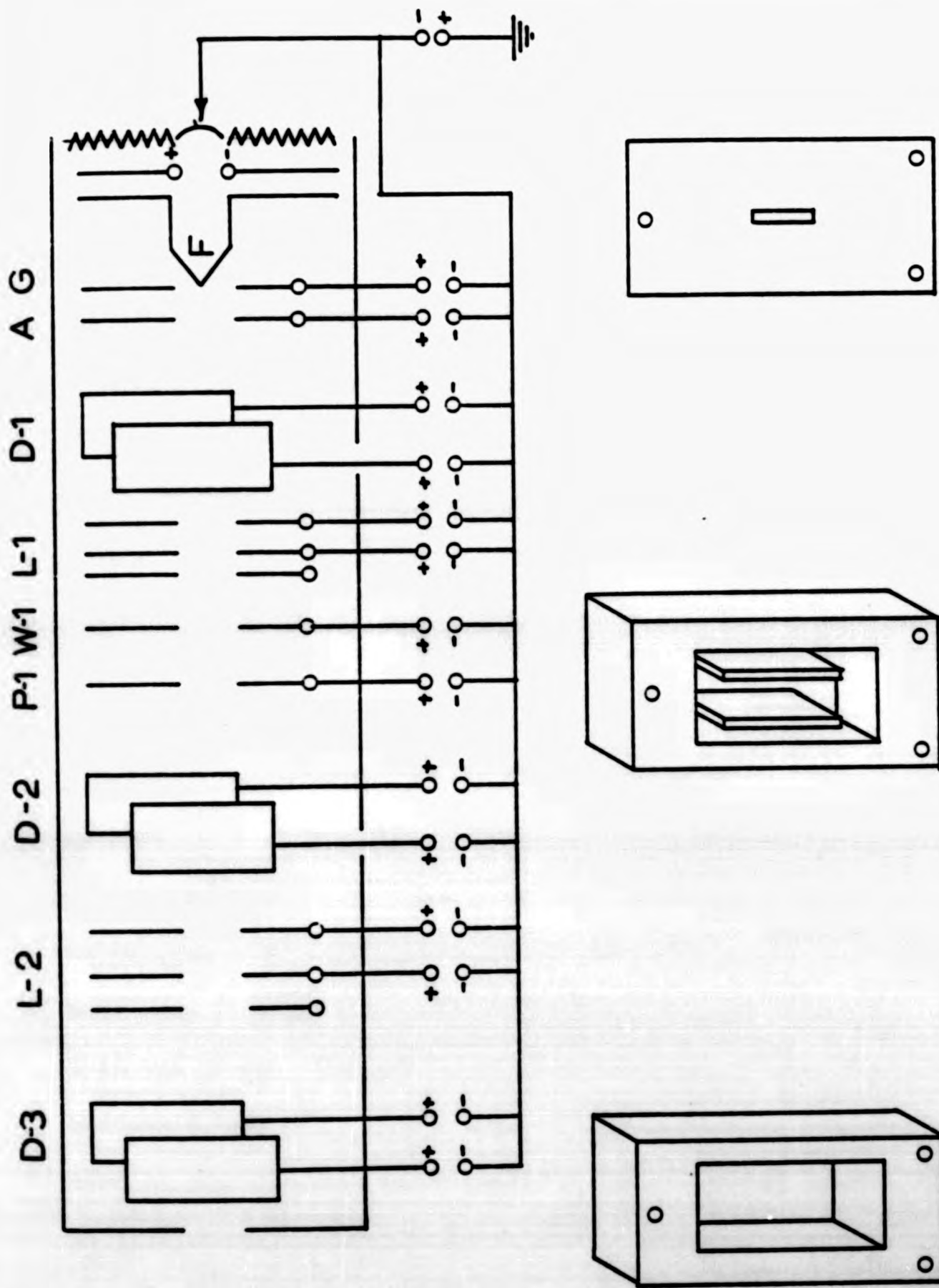


Figure (3-11): Schematic diagram of the electron gun.

The focussing systems consist of two einzel lenses L-1 and L-2 and two pairs of deflection plates D-1 and D-2. An extra pair of deflection plates D-3 was used to correct any misalignment of the electron beam. All elements of the electron gun and of the analyser optics were made rectangular (25 x 50 mm<sup>2</sup>) and slits of widths between 0.4 mm and 5 mm and heights between 5 mm and 10 mm were used as apertures throughout. This should match the interaction region to the height of the analyser and thus increase the sensitivity of the system. The elements of the electron gun were held in position by three 3 mm ceramic tubes which pass through all elements. They are clamped and mounted to the base plate by three stainless steel rods, threaded M2, which are inserted inside the ceramic tubes. The complete layout with dimensions is shown in figures (3-10) and (3-11).

Due to the use of very thin PTFE insulators (0.1 mm thick) for the isolation of the electrodes fig.(3-10) in the electron gun, there were electrical shorts and current leakage problems. These problems were solved by using mica (0.2 mm thick) insulators instead of PTFE.

The electrostatic lens elements were made from 0.1 mm thick molybdenum sheet, while the spacers and the deflection plates were made from duraluminium. The thickness of the spacers varies between 1.25 and 12 mm. The apertures of the electrostatic lens elements are between 0.4 mm and 5 mm wide and between 0.4 and 10 mm long, the size of the exit slit is 8 x 2 mm<sup>2</sup>. Mica and PTFE layers were used as insulation between the electrodes.

The filament was made from 0.1 mm $\phi$  tungsten wire and heated by a constant current power supply (5A, 20V). During the present work, 1.25A was used to heat the filament. The filament could be replaced easily without affecting the rest of the electron gun assembly by unscrewing the plate on the back of the gun.

All connections of the electron-gun elements except those of the filament were made with PTFE-insulated, stainless steel wire of 0.2 mm $\phi$ . The wires were bunched together and carefully shielded with copper braid. The electron gun assembly was housed in an aluminium shield and any metal surfaces near the interaction region were sooted to reduce reflections of electrons.

The potential distribution panel has twelve 10-turn helipot (100k $\Omega$ , 5W) connected in parallel to provide appropriate potentials to the elements in the electron gun. The power to this distribution panel was provided by a 0-425 volts power supply (Kepco, ABC 425M).

The voltages required for the deflection plates were derived from three separate power supplies using pairs of resistors to balance the plate voltages with respect to the electron potential. Fig. (3-12) shows the connections of the distribution panel and of the deflection plates in the electron gun.

If there is a short circuit between the electrodes of the electron gun or the 127 $^{\circ}$  electron analyser the increased current might damage the potentiometer, especially when it is set near its extreme values. To avoid this, guard resistors of 42 k $\Omega$  each have been used in series with the electrode connections.

### 3.5. Atomic Beam Source

The atomic beam emerging from the source should ideally be strongly peaked in the forward direction. A simple aperture source has the disadvantage of a broad cosine intensity distribution. The number of particles per second effusing into a solid angle  $d\omega$  at an angle  $\theta_0$  with respect to the normal of the aperture is (Ramsey, 1963)

$$N(\theta)d\omega = \frac{\bar{n}V A}{4\pi} \cos(\theta)d\omega \quad 3.10$$

where

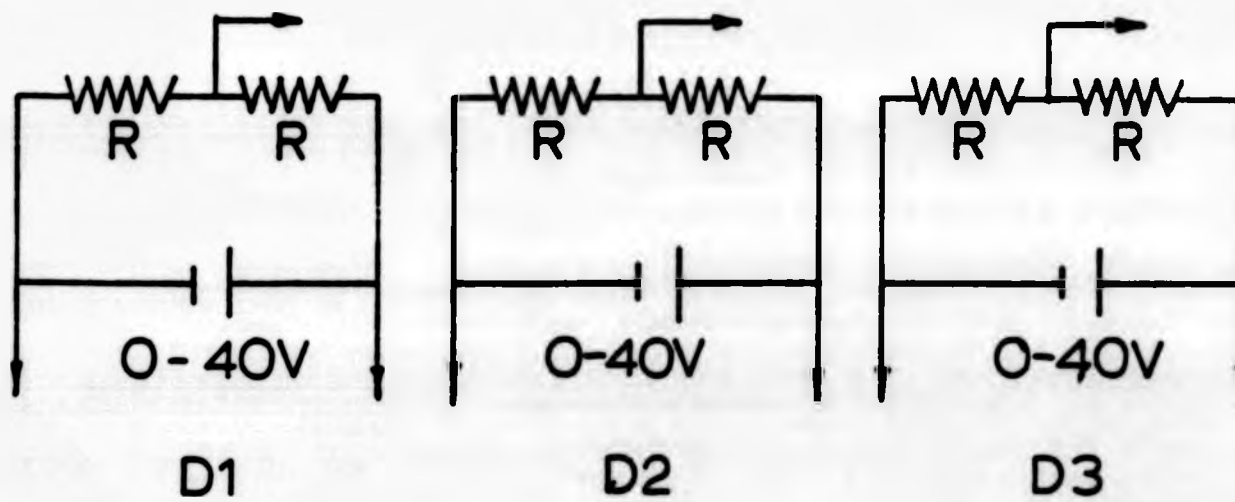
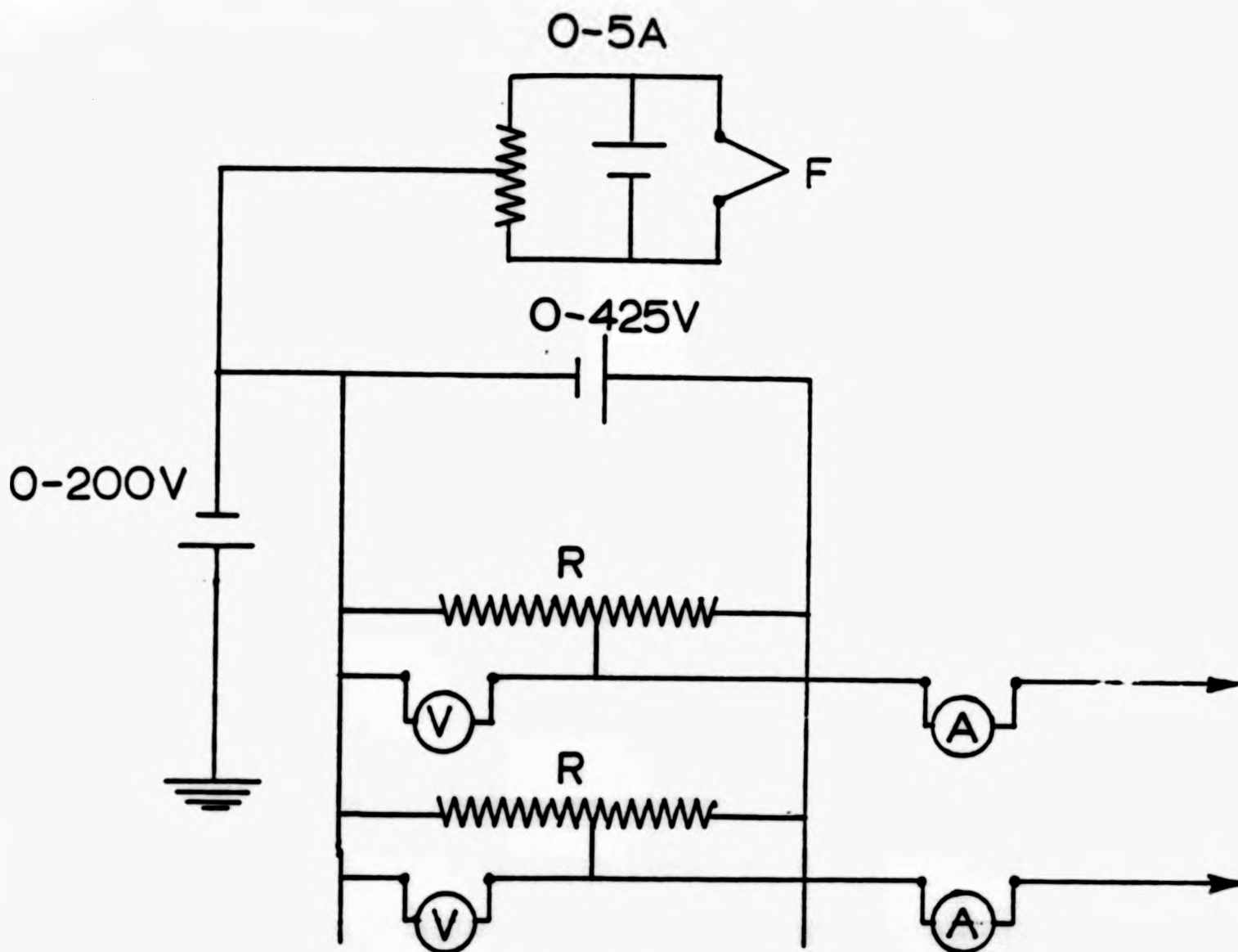


Figure (3-12): Schematic diagram of the voltage power supplies for the elements of the electron gun, 127° electron analyser assembly and the deflection plates.

$N(\theta) d\omega$  is the number of particles per second effusing into solid angle  $d\omega$  from the source slit.

$n$  is the number of particles per volume in the enclosure.

$\bar{v}$  is the average velocity of the particles.

and  $A$  is the area of the source slit.

The total number of particles escaping through the aperture in all directions can be found by integrating equation (3-10) over the solid angle ( $d\omega = 2\pi \sin\theta d\theta$  where the integration goes from  $\theta = 0$  to  $\frac{\pi}{2}$ ), resulting in  $N = \frac{1}{4} n \bar{v} A$ .

The collimation properties of long channels have been studied theoretically by Clousing (1930) and experimentally by Becker (1961). Giordmaine and Wang (1960) showed that the beam properties are strongly dependent on the pressure conditions within the channel.

According to the relationship between the mean free path  $\lambda$  inside the tube, the tube radius  $a$  and its length  $l$ , different results for the beam intensity and angular distribution are obtained. It is assumed throughout that  $a \gg l$ , i.e. that the tube is long.

1. The limiting case at low gas pressure is that of molecular flow ( $\lambda \gg l$ ). In this case, collisions between atoms can be neglected and the tube is called "transparent". This case is the simplest from the theoretical point of view and gives the highest collimation, but the throughput is limited by the condition  $\lambda \gg l$ . The beam collimation is determined by the

$N(\theta) d\omega$  is the number of particles per second effusing into solid angle  $d\omega$  from the source slit.

$n$  is the number of particles per volume in the enclosure.

$\bar{v}$  is the average velocity of the particles.

and  $A$  is the area of the source slit.

The total number of particles escaping through the aperture in all directions can be found by integrating equation (3-10) over the solid angle ( $d\omega = 2\pi \sin\theta d\theta$  where the integration goes from  $\theta = 0$  to  $\frac{\pi}{2}$ ), resulting in  $N = \frac{1}{4} n\bar{v} A$ .

The collimation properties of long channels have been studied theoretically by Clousing (1930) and experimentally by Becker (1961). Giordmaine and Wang (1960) showed that the beam properties are strongly dependent on the pressure conditions within the channel.

According to the relationship between the mean free path  $\lambda$  inside the tube, the tube radius  $a$  and its length  $l$ , different results for the beam intensity and angular distribution are obtained. It is assumed throughout that  $a \gg l$ , i.e. that the tube is long.

1. The limiting case at low gas pressure is that of molecular flow ( $\lambda \gg l$ ). In this case, collisions between atoms can be neglected and the tube is called "transparent". This case is the simplest from the theoretical point of view and gives the highest collimation, but the throughput is limited by the condition  $\lambda \gg l$ . The beam collimation is determined by the

geometry of the tube.

2. At higher pressure, collisions between the atoms occur and play a major role in determining the beam characteristics. In the case  $\lambda \ll \ell$ , but with  $\lambda > a$  at the low pressure end of the tube, the beam intensity can still be calculated. This is called intermediate flow, which is the most important for practical applications.

Giordmaine and Wang (1960) calculated the beam intensity on the axis  $I(\theta=0)$ , under the assumption of intermediate flow for a long tube and found

$$I(\theta = 0) = \frac{1}{\sqrt{288}} \left( \frac{3 \bar{v} a N}{\pi} \right)^{\frac{1}{2}} \text{ molec sterad}^{-1} \text{ sec}^{-1} \quad 3.12$$

where  $N$  is the total flow rate,  $\delta$  is the atomic diameter and  $\bar{v}$  is the average velocity of the particle in the beam. The beam density  $I(d)$  in the interaction region at a distance  $d$  from the source, is proportional to  $\frac{1}{d^2}$ .

The average velocity of the particles in the beam is given by Ramsey (1956)

$$\bar{v} = \left( \frac{9\pi k T N_a}{8A} \right)^{\frac{1}{2}} \text{ cm sec}^{-1} \quad 3.13$$

where

- $k$  is the Boltzman constant
- $T$  is the absolute temperature
- $N_a$  is the Avogadro number, and
- $A$  is the atomic weight.

In an equilibrium state the total effusion rate  $N$  is related to pressure  $P_0$  in Torr and the overall effective pumping speed  $S_0$  in litres  $\text{sec}^{-1}$

$$N = 3.5 \times 10^{19} \cdot S_0 \cdot P_0 \text{ atoms sec}^{-1} \quad 3.14$$

The numerical factor converts the flow rate in Torr l sec<sup>-1</sup> into molecules sec<sup>-1</sup>.

In the present experiment the tube diameter was 0.5 mm and the length was 50 mm. The base pressure  $1.0 \times 10^{-7}$  Torr and the load pressure with gas injected up to  $1.4 \cdot 10^{-6}$  Torr. Using an overall pumping speed of  $540 \text{ l s}^{-1}$  for air, the flow rate is according to equation (3.14).

$$\begin{aligned} N &= 3.5 \cdot 10^{19} \cdot 540 \cdot 1.4 \times 10^{-6} \\ &= 2.7 \cdot 10^{16} \text{ atoms sec}^{-1} . \end{aligned}$$

To calculate the beam density  $\rho$  in the interaction region at a distance equal of 0.5 cm from the end of the tube substitute the following values of the various parameters in equation (3.12)

$$\begin{aligned} \delta &= 2.82 \cdot 10^{-8} \text{ cm} \\ v &= 2.28 \cdot 10^4 \text{ cm sec}^{-1} \\ a &= 0.025 \text{ cm} \\ N &= 2.7 \cdot 10^{16} \text{ atoms sec}^{-1} \\ I &= 1.42 \cdot 10^{16} \text{ atoms cm}^{-2} \text{ sec}^{-1} \\ \rho &= \frac{I}{v} = 2.61 \cdot 10^{12} \text{ atoms cm}^{-3} \\ &= 6.2 \cdot 10^{11} \text{ atoms cm}^{-3} \text{ for } N_2 \end{aligned}$$

In the present experiment helium is used instead of air. Taking into account the correction of the ion-gauge reading for helium, the increased pumping speed (estimated to be two times that of air), and the difference in the atom radius and the mean velocity compared with  $N_2$ , the helium flux  $I$  and the density  $\rho$  in the interaction region at a distance of 0.5 cm from the end of the tube are estimated to be,

$$I = 1.0 \cdot 10^{19} \text{ atoms cm}^{-2} \text{ sec}^{-1}$$

and  $\rho = 1.5 \cdot 10^{13} \text{ atoms cm}^{-3}$ .

### 3.6. The Optical System for the Polarization Measurements

#### 3.6.1. Introduction

A new optical system has been built to measure the polarization correlation in this experiment. This system is drawn schematically in fig. (3-13). It consists of a lens of 50 mm $\phi$  and a focal length of 75 mm, which was fixed inside the excitation chamber above (and parallel to) the scattering plane, a mica quarter wave plate of 20 mm $\phi$  for  $\lambda=501.6$  nm (Melles Griot type 02 WRN003), a linear polarizer of 30.2 mm $\phi$  (Melles Griot type 03 FPG003), an interference filter with a peak transparency of 56% (type MDTE DD01), and a photomultiplier tube (EMI 9883QB).

All the components apart from the lens are fixed to the end flange opposite to the main turntable flange. The quarter wave plate was fixed outside the vacuum chamber next to the quartz window and was removed for linear polarization measurements. The linear polarizer and the interference filter were mounted inside the brass housing in front of the photomultiplier.

All the components of the photon detector assembly (except the  $\frac{\lambda}{4}$  plate), were mounted together and rotated about their axis to set the transmission axis of the linear polarizer to angles between 0 and 180°. The angle  $\alpha$ , of the linear polarizer axis is measured with respect to the incident electron beam direction in the same sense as the scattered electron angle  $\theta_e$ . In case of circular polarization measurements, the  $\frac{\lambda}{4}$  plate was inserted in front of the linear polarizer (slow axis of the  $\lambda/4$  plate parallel to the electron beam direction) outside

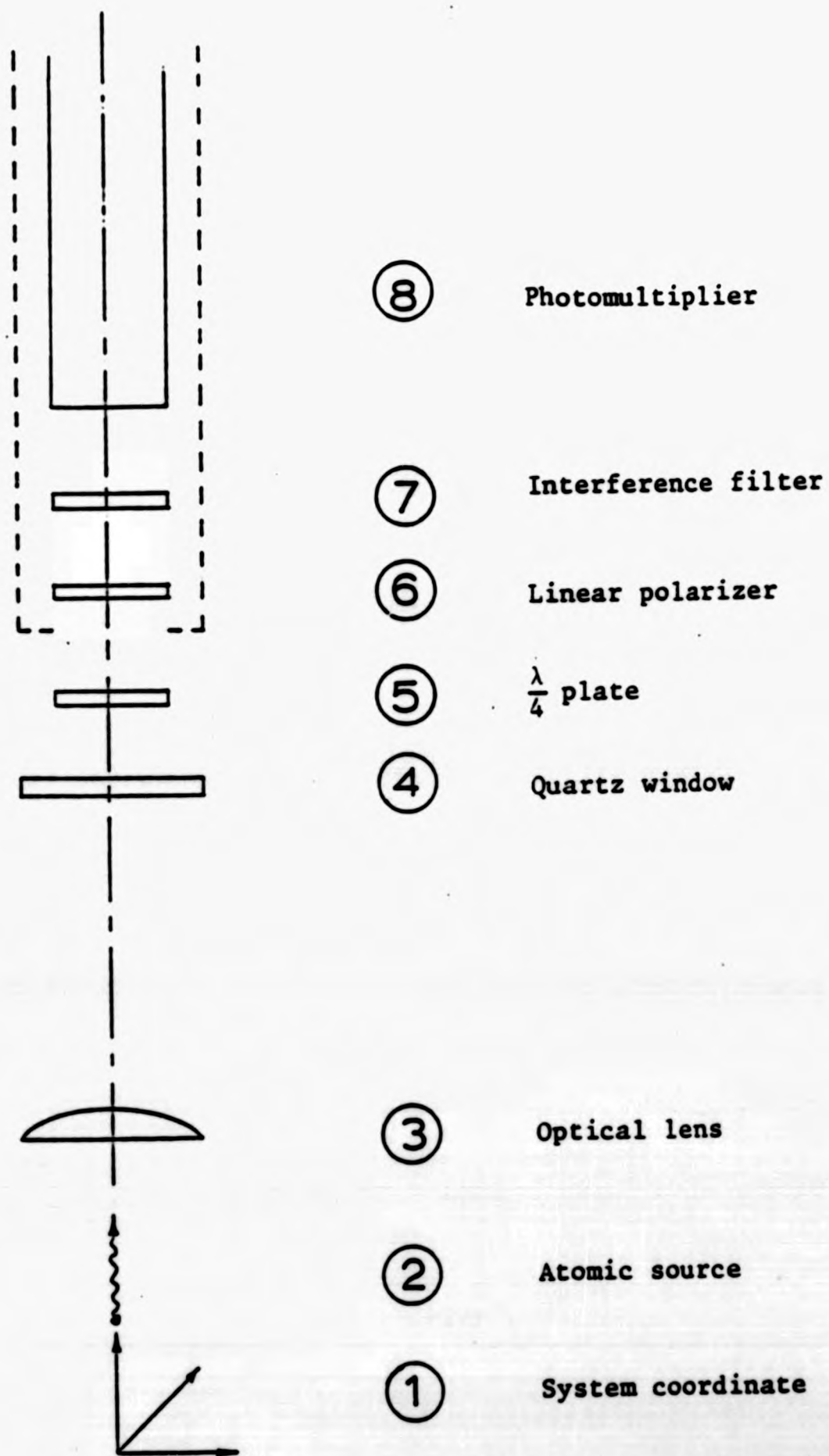


Figure (3-13): Schematic diagram of the optical system.

the brass housing of the photomultiplier tube. Figure (3-14) shows a schematic diagram of the brass housing and the mounting.

The coordinate system has been chosen so that the direction of observation of the light is along the y-axis, which is perpendicular to the scattering plane (z-x plane). The Stokes parameters  $\eta_1$ ,  $\eta_2$  and  $\eta_3$  associated with the linear and circular polarization measurements are defined with respect to this detector system.

### 3.6.2. Alignment

To measure the light, an accurate alignment of all optical components is necessary.

As shown in fig. (3-13), a plane-concave lens of 50 mm $\phi$  and 75 mm focal length has been fixed inside the vacuum chamber in a position parallel to the scattering plane. The other components of the optical system were fixed to the flange facing the scattering plane.

To set the alignment of the light beam, a light source was fixed in the centre of the interaction region (on the top of the helium nozzle); the lens position was then adjusted such that the image of the source was  $\approx 3$  cm beyond the quartz window. This position of the optical lens (98 mm from the source point) gives an image magnification of 3.

A photon detector has been mounted outside the vacuum chamber, the interaction region being viewed through a quartz window.

### 3.6.3. The Photomultiplier

For the polarization correlation measurement, a photomultiplier tube EMI 9883 QB, cathode  $\phi$  46 mm) was used to detect the radiation emitted from the excited atoms. The EMI 9883 tube has a bi-alkali cathode and fourteen dynode stages. The first dynode is specially

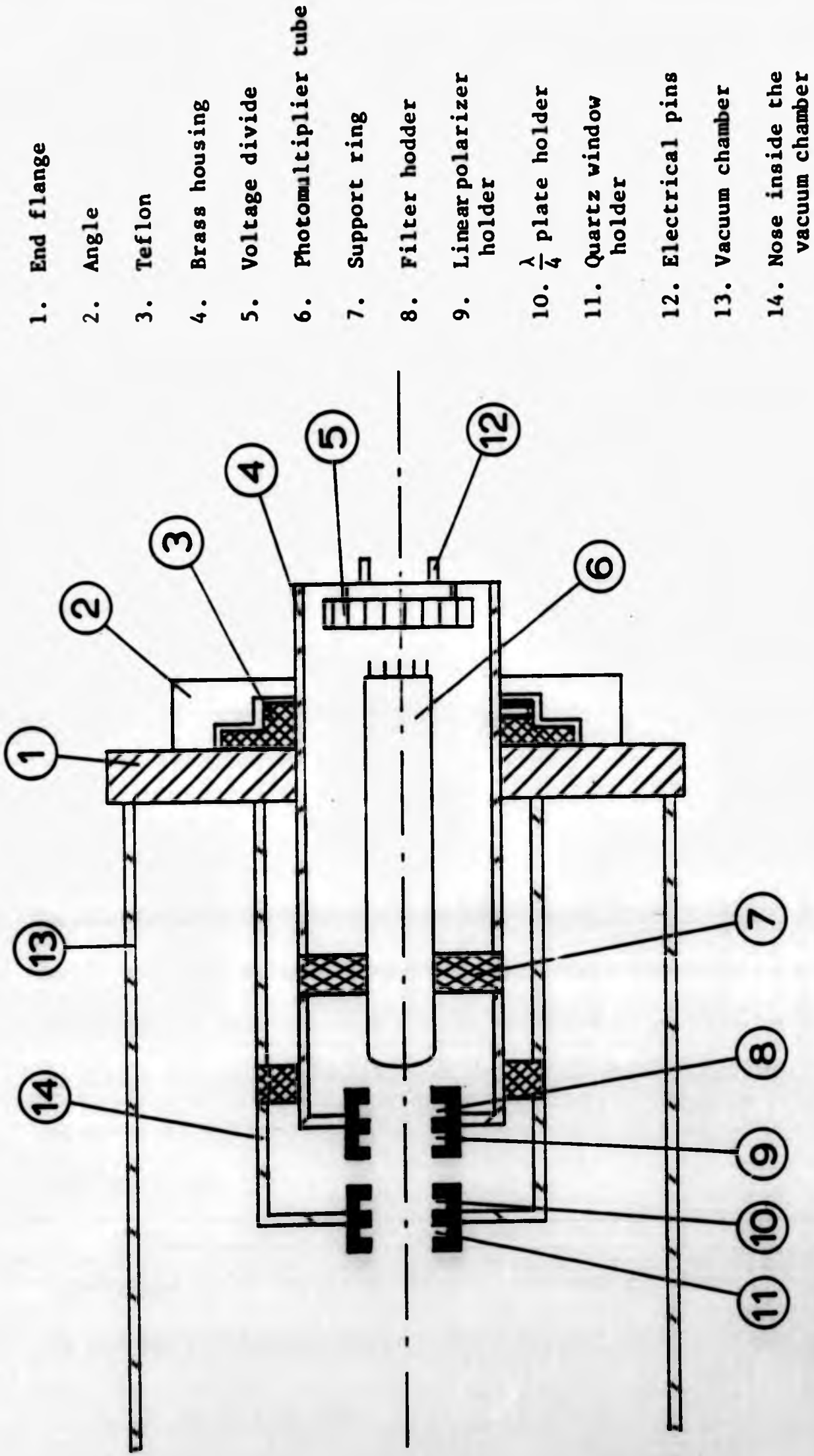


Figure (3-14): Schematic diagram of the brass housing and the mounting.

prepared to give a high secondary emission for the photo-electrons and to give improved single electron resolution.

The quantum efficiency of a photocathode to light of wavelength  $\lambda$  is defined as the number of photoelectrons emitted from the photocathode per incident photon. This ratio is usually expressed as a percentage. According to the manufacturer's catalogue the quantum efficiency of the photocathode used in the EMI 9883 tube is approximately 15% for light of the wavelength 501.6 nm.

The typical pulse height measured at the operating voltage of 2100 volts was 0.25 volt. The pulse height distribution is shown in figure (3-15) and the pulse shape in figure (3-16). The rise time (10% to 90%) of the output pulses is approximately 2 ns.

#### 3.6.4. The Voltage Divider

The photomultiplier must be correctly biased. This can be achieved by using an independent voltage supply for each stage, but it is more convenient to use a voltage divider network, consisting of a series of resistors between earth and high potential. The current flow in this divider network establishes a series of potentials which are applied to the dynodes and focussing elements of the photomultiplier. These potentials create the electrostatic fields required to focus the photo electrons on the first dynode and to accelerate the electron cascade between successive dynodes thereby providing current amplification.

Using an operating voltage of 2200 V, the gain of the photomultiplier is of the order of  $10^7$ . The charge induced on the anode by a single electron emitted from the cathode is given by

$$\begin{aligned} Q &= e \cdot \text{gain} \\ &= 1.6 \cdot 10^{-19} \cdot 10^7 = 1.6 \cdot 10^{-12} \text{ C.} \end{aligned} \quad 3.15$$

The average anode current  $I_a$  for an assumed maximum count rate of

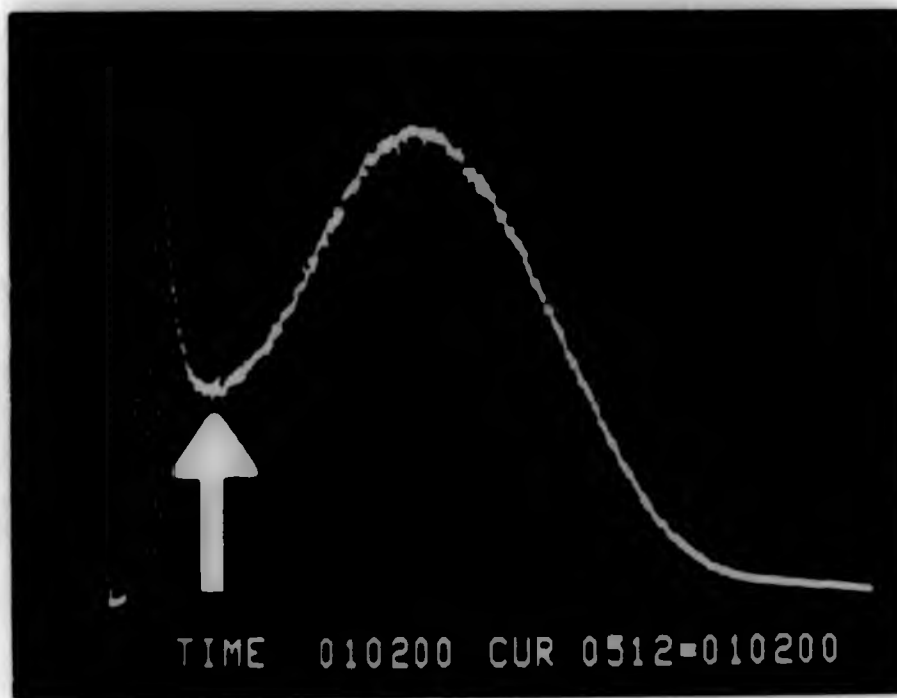


Figure (3-15): The pulse height spectrum of the photomultiplier (EMI 9883 BQ) showing a clear single electron peak. Discriminator level was set at the low point of the distribution as indicated by the arrow.

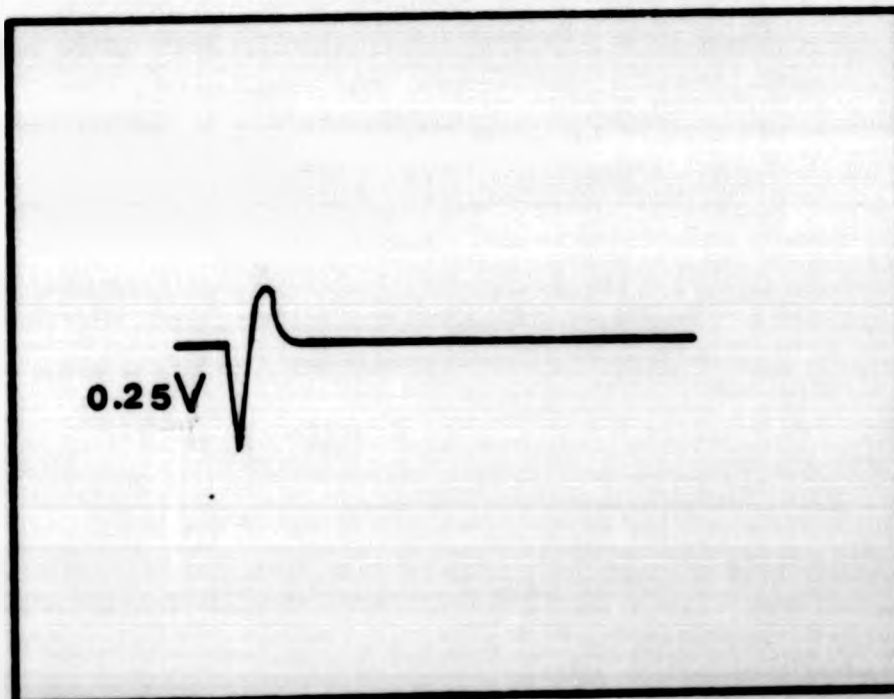


Figure (3-16): Photomultiplier signal shape, measured by oscilloscope (454A), rise time  $\approx$  2 ns.

1MHz is  $1.6 \times 10^{-6}$  A, and the maximum anode current  $I_D$  during a pulse lasting approximately  $5 \cdot 10^{-9}$  sec is  $0.32 \cdot 10^{-3}$  A. A voltage divider current of  $0.026 \cdot 10^{-3}$  A has been chosen which is compatible with the average anode current and causes little heating of the resistor chain (total power  $I_D^2 R = 0.03$  watt).

In order to cope with the large transient current during the pulses without voltage breakdown, 1nF capacitors have been inserted in parallel to the chain over the last 4 dynode stages.

The multiplier EMI 9883 has been specially designed to provide good pulse height resolution for single electrons ejected from the cathode by photons. Such single electron resolution requires large magnification in the first stage of the multiplier, and a maximum  $V(K-D_1)$  of 600V is specified. In the present set up  $V(K-D_1)$  was chosen to be 300V.

The transit time spread is inversely proportional to the inter-dynode voltage (Poultney 1972). Hence this should be as large as possible, consistent with the prevention of breakthrough, to achieve minimum possible rise time. This also gives maximum possible gain.

It should be noted that besides the pulse rise time, there is another factor which will affect time resolution. This is the "jitter" in the transit times of successive photoelectrons due to their different possible trajectories. These differences arise predominantly from the variation in position and velocity of the photoelectron as it is emitted from the photocathode. This is another reason to use a large  $K-D_1$  voltage.

Figure (3-17) shows a schematic diagram of the voltage divider used in the present experiment.

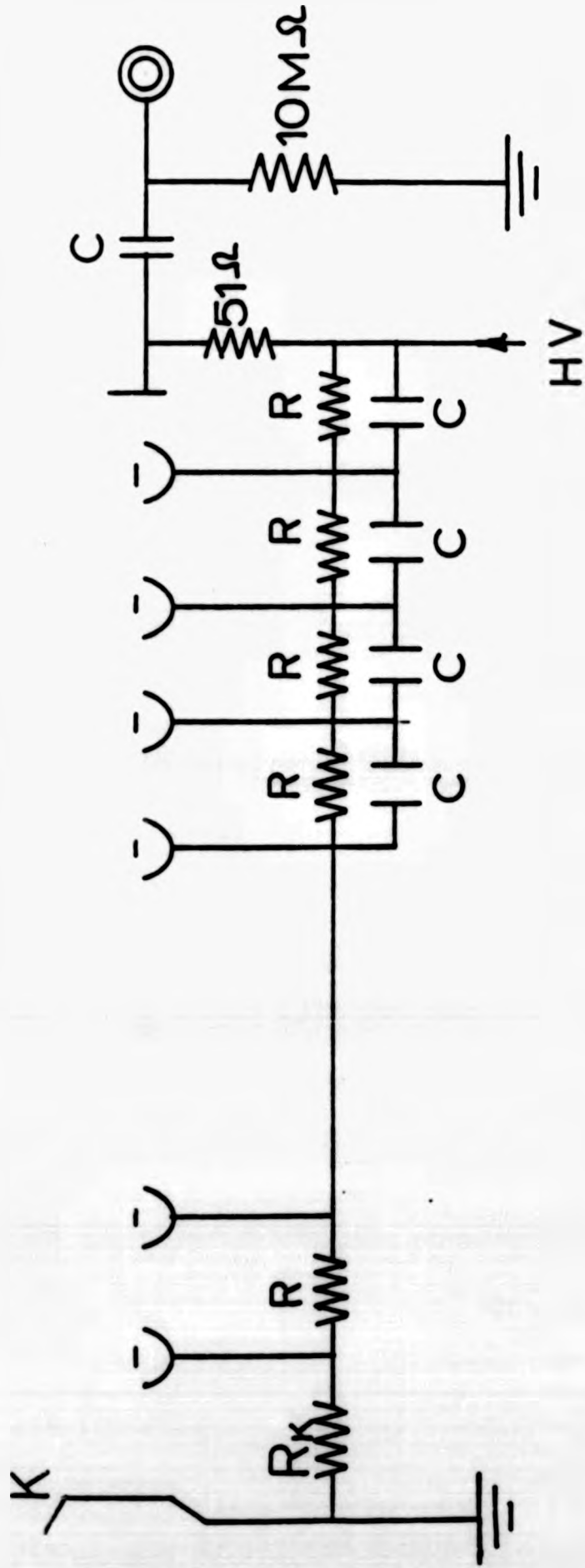


Figure (3-17): Voltage divider circuit for photon counting applications using tube type (EMI 9883 BQ).

- R<sub>k</sub> = 15.6 MΩ
- R = 5.6 MΩ
- C = 1nf

### 3.7. Detection of VUV Photons and Scattered Electrons

#### 3.7.1. Introduction

Two channel electron multipliers [CEM] were used in the angular correlation measurements, one to detect the scattered electrons having passed the  $127^\circ$  analyser assembly and the other to detect the radiation emitted by the excited atoms.

Fig. (3-18 and 19) show schematic diagrams of the channeltron multiplier for photons and for electrons respectively. All earth connections are joined inside the detector housing and one connection is lead outside.

#### 3.7.2. VUV Photon Detection

In the angular correlation measurements the radiation emitted following the collision process was detected by a channeltron multiplier used as a photon detector. Three grids, each made up of four tungsten wires  $0.1 \text{ mm}\phi$  (transparency  $\approx 90\%$  per grid), were mounted at the entrance of the detector housing to prevent charged particles from entering the CEM. Grid 1 was connected to earth, grid 2 to +10 volts and grid 3 to -135 volts. The channeltron multiplier and decoupling circuit were housed inside an aluminium cylinder which was fixed to one layer of the turntable assembly. The HV to the detector was provided by 6KV power supply (Fluke model 408B) through a filter network as shown in fig. (3-18).

The detector was normally operated at 3200 volts. Because of its low efficiency at wavelengths above 100 nm it was used for the detection of uv photons emitted in the decay of the  $2^1\text{P}$  and  $3^1\text{P}$  states of helium radiating at 58.45 nm and 53.7 nm respectively.

#### 3.7.3. Scattered Electron Detection

The channel electron multiplier used to detect the scattered electrons is held in a PTFE block and placed 1 mm from the last slit of the output optics of the analyser. Keeping the channeltron close to the slit ensured that most of the electrons were

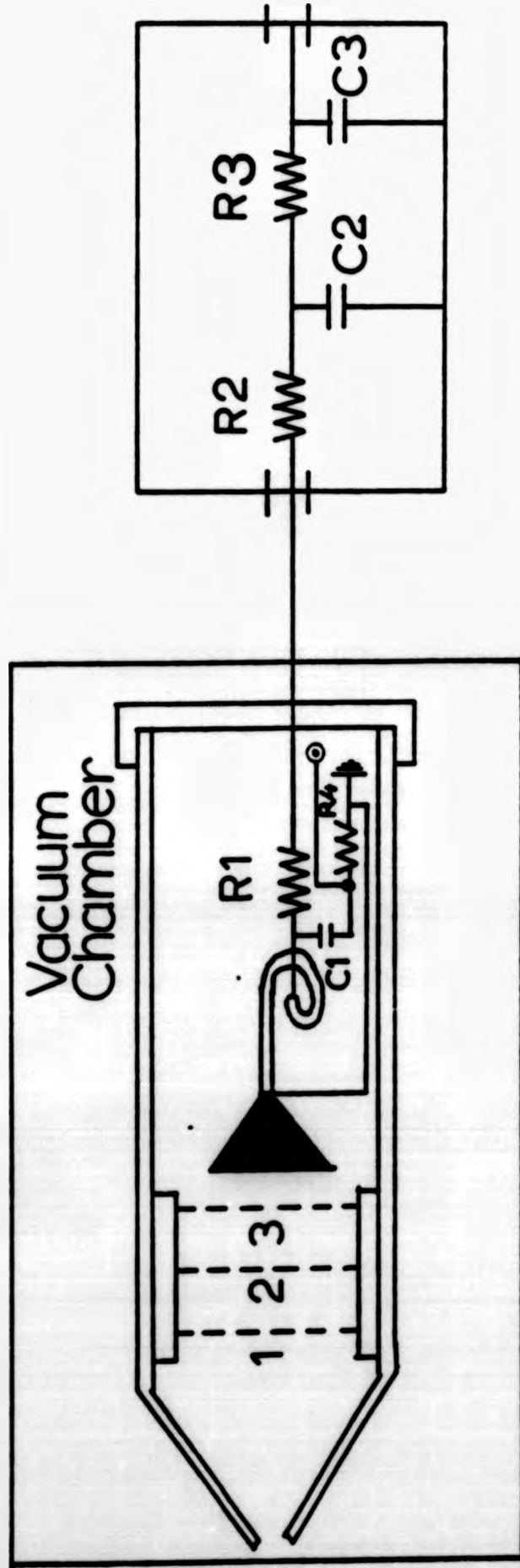


Figure (3-18): Schematic diagram of the VUV photon detector showing the cone, the cover of the photon multiplier, the three grids, the channeltron connection and the filter network circuit.

$C_1 = C_2 = C_3 = 0.1 \text{ pF}$ ,  $7.5 \text{ kV}$ .

$R_1 = 1 \text{ M}\Omega$

$R_2 = R_3 = 250 \text{ k}\Omega$

$R_4 = 820 \Omega$

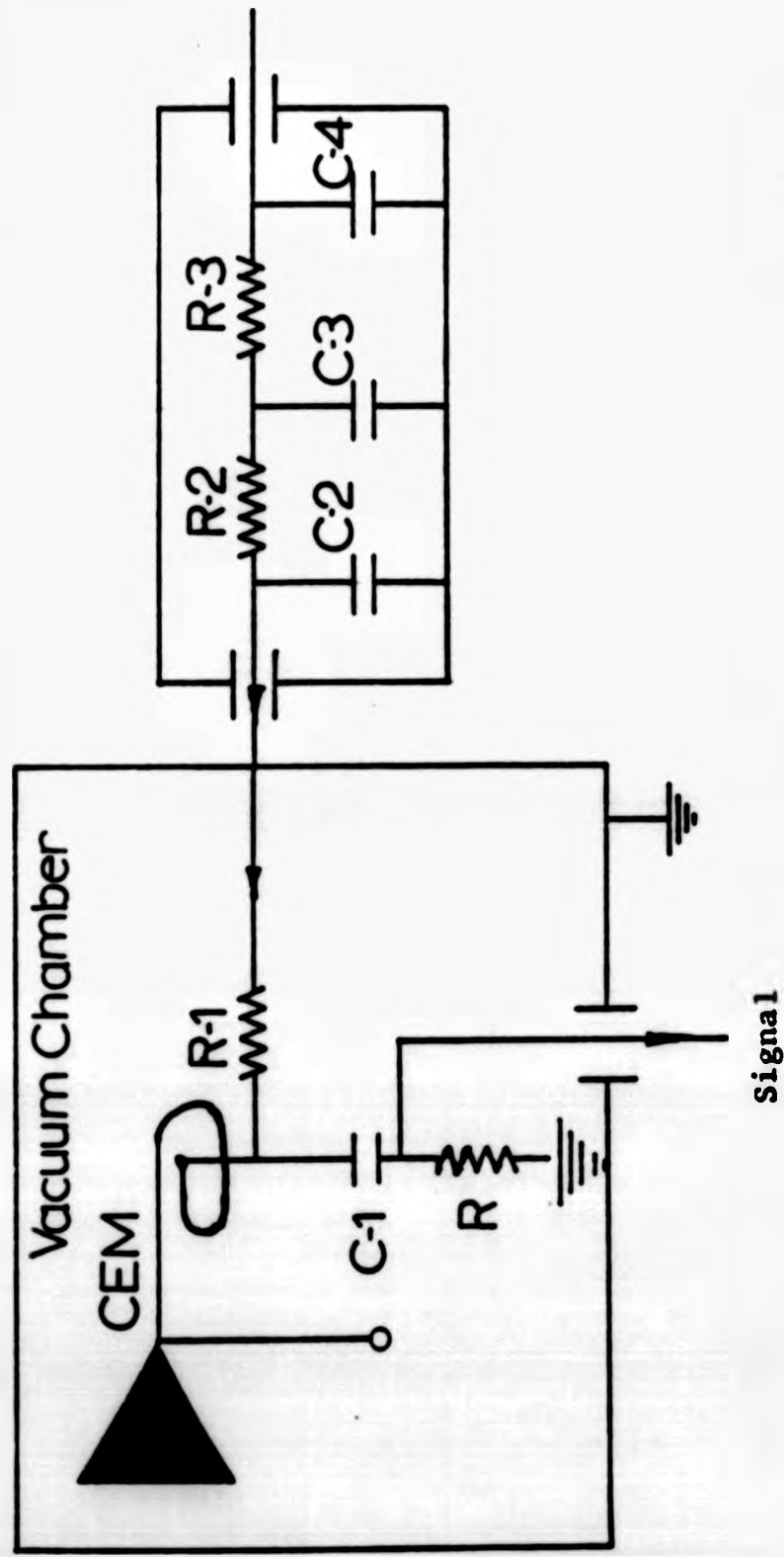


Figure (3-19): A schematic diagram of electrical circuit of the channel electron multiplier used as scattered electron detector, the filter network circuit and the output signal connections.

$C_1 = C_2 = C_3 = C_4 = 0.1 \text{ pF}$  and  $7.5 \text{ kV}$ .

$R_1 = 1 \text{ M}\Omega$

$R_2 = R_3 = 250 \text{ k}\Omega$

$R = 820\Omega$

collected by the detector and at the same time prevented stray electrons from entering the channel electron multiplier. The front of the electron detector is biased to accelerate the electrons to energies giving best detection efficiency.

The high voltage for the channel electron multiplier was provided by a 6 kV power supply [Fluke Model 408B] through a filter network  $C_2C_3R_2R_3$  connected to the high voltage electrical feedthrough. A capacitance  $C_1$  was used to block the H.V. from the signal line and the resistance  $R$  is the working resistance of the circuit.

Figure (3-19) shows a schematic diagram of the filter network and the channel electron multiplier connections.

### 3.8. Coincidence Circuit

A block diagram of the timing electronics is shown in fig.(3-20) together with the general layout of the system for angular correlation measurements.

The signal from each detector (electron and photon) is amplified by fast amplifiers (dual bipolar linear amplifier Le Croy Model 333) and fed into a constant fraction timing discriminator "CFD" (ORTEC, Model 473). The electron timing pulse from the CFD starts the ramp of a time-to-amplitude converter "TAC" (ORTEC Model 467), and the photon timing pulse, suitably delayed, is used to stop the ramp. The amplitude of the TAC output signal is proportional to the time difference between the stop and start pulses. A multichannel analyzer (NORLAND INO TECH 5300) is used to record the resulting pulse height spectrum from the TAC. All the timing electronics was placed at a short distance from the vacuum chamber to avoid pick-up noise.

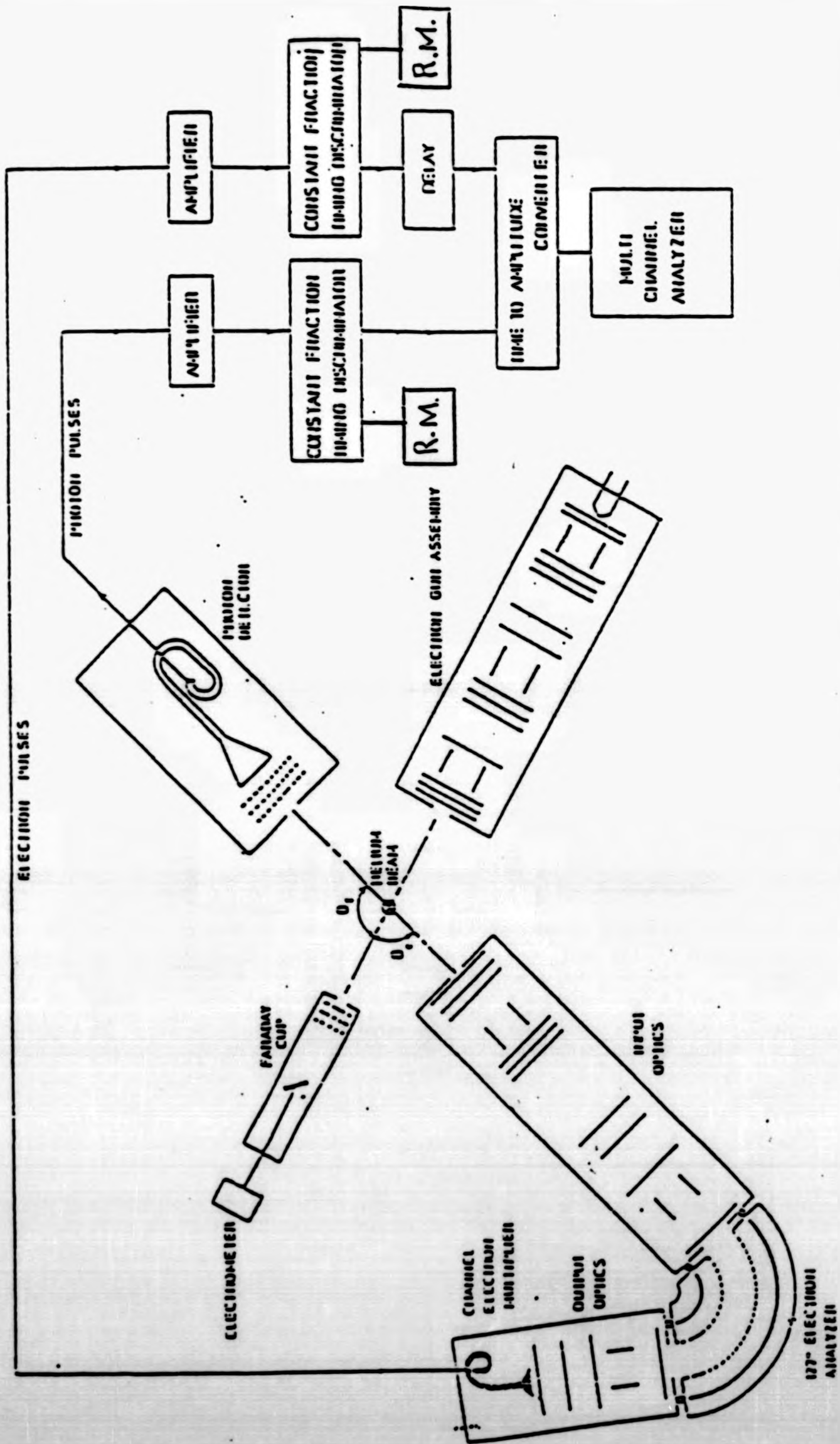


Figure (3-20): Schematic diagram of the apparatus for electron-photon angular correlation measurements.

### 3.9. Interlock System

To ensure safe operation the apparatus is controlled by an interlock system which acts when either the pressure inside the vacuum chamber rises or the temperature in the diffstack pump increases due to water failure. Any such failure causes a complete shutdown of the system. This shutdown involves the isolation of the vacuum system from the pumps and the disconnection of all electrical supplies to the system.

The system remains switched off until the interlock system is reset. The interlock system has responded successfully on several occasions.

CHAPTER IV  
MEASUREMENTS AND DATA ANALYSES

4.1. Electron Signal

4.1.1. The Alignment of the Electron Beam and the Analyser

The alignment of the electron gun, Faraday cup, 127° electron analyser and the helium nozzle is carried out visibly as follows:

- A. Insert a piece of wire of 0.2 mm $\phi$  into the gas nozzle to mark the centre of the interaction region.
- B. Remove the cathode plate from the electron gun and look through the apertures of the gun to the target from the filament side. Adjust the gun so that the target can be seen exactly in the centre of the rectangular slits.
- C. Place the 127° electron analyser in straight-through position opposite the electron gun (i.e.  $\theta_e=0$ ) and look through the hole in the back plate of the analyser. Adjust the analyser mount in such a way that the centre of the interaction region and at the same time all gun apertures are aligned in the centre of the rectangular apertures of the analyser input optics.
- D. Rotate the analyser over the full angular range and ensure that the wire is always seen in the centre of the analyser apertures.
- E. Place the Faraday cup at 0° and look to its collector from the cathode side. Adjust the Faraday cup in a straight line with the slits of the electron gun intercepting the target.

4.1.2. Performance of the Electron Gun

The cathode of the electron gun (tungsten wire of 0.1 mm $\phi$ ) was heated by a current of 1.2A. The voltages applied to the electrodes were then optimised by monitoring the electron beam at the focussing stages of the electron gun and finally at the Faraday cup. The

electron beam current measured at the Faraday cup which was biased +15V with respect to earth was typically 0.6  $\mu$ A and the beam diameter  $\approx$  1 mm in the interaction region, with an angular spread of  $2^\circ$  as shown in the figure (4-1)

#### 4.1.3. The 127 $^\circ$ Electron Analyser

The voltages applied to the elements of the analyser input and output were optimized to focus the energy-analysed scattered electrons on to the entrance of the channel electron multiplier which was biased at  $\approx$  100V with respect to earth.

An angular scan of the primary beam current transmitted through the analyser was made as shown in figure (4-2).

#### 4.1.4. Energy Loss Spectrum

The scattered electrons transmitted through the analyser operating at an energy of 9.6 eV were detected by the channel electron multiplier and an elastic spectrum was obtained on the MCA in its multichannel scaling mode, by scanning the reference potential of the analyser with the ramp voltage supplied by MCA.

To obtain the inelastic spectrum, e.g. at an energy of 50 eV, the analyser was tuned to transmit the scattered electrons which had excited the helium atoms and suffered an energy loss of 22.8 eV from the  $3^1P_1$  excitation. The reference potential of the analyser, and with it the potentials of all analyser elements, were varied around this value by the ramp voltage supplied by the MCA, so that the energy loss spectrum was obtained. A check was made with the ratemeter that the count rate varied with the energy of the detected electrons.

The elastic peak and the energy loss spectra are shown in figure (4-3) for electron impact energies of 50 and 160 eV at electron scattering angles  $40^\circ$  and  $71^\circ$ , respectively. The combined

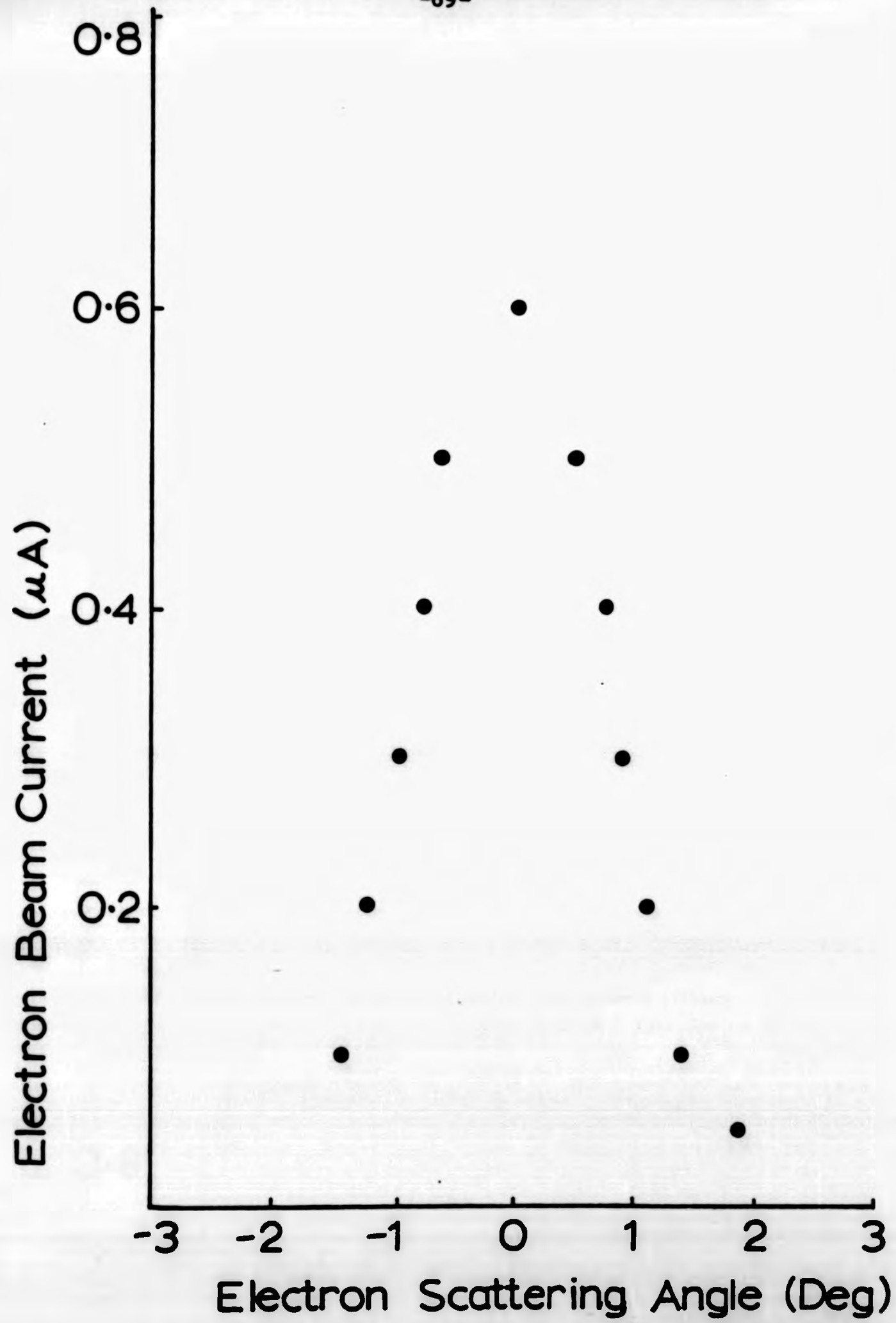


Figure (4-1): Angular distribution of the electron beam measured by the Faraday cup at an incident energy of 80 eV. The FC resolution is  $2^{\circ}$ .

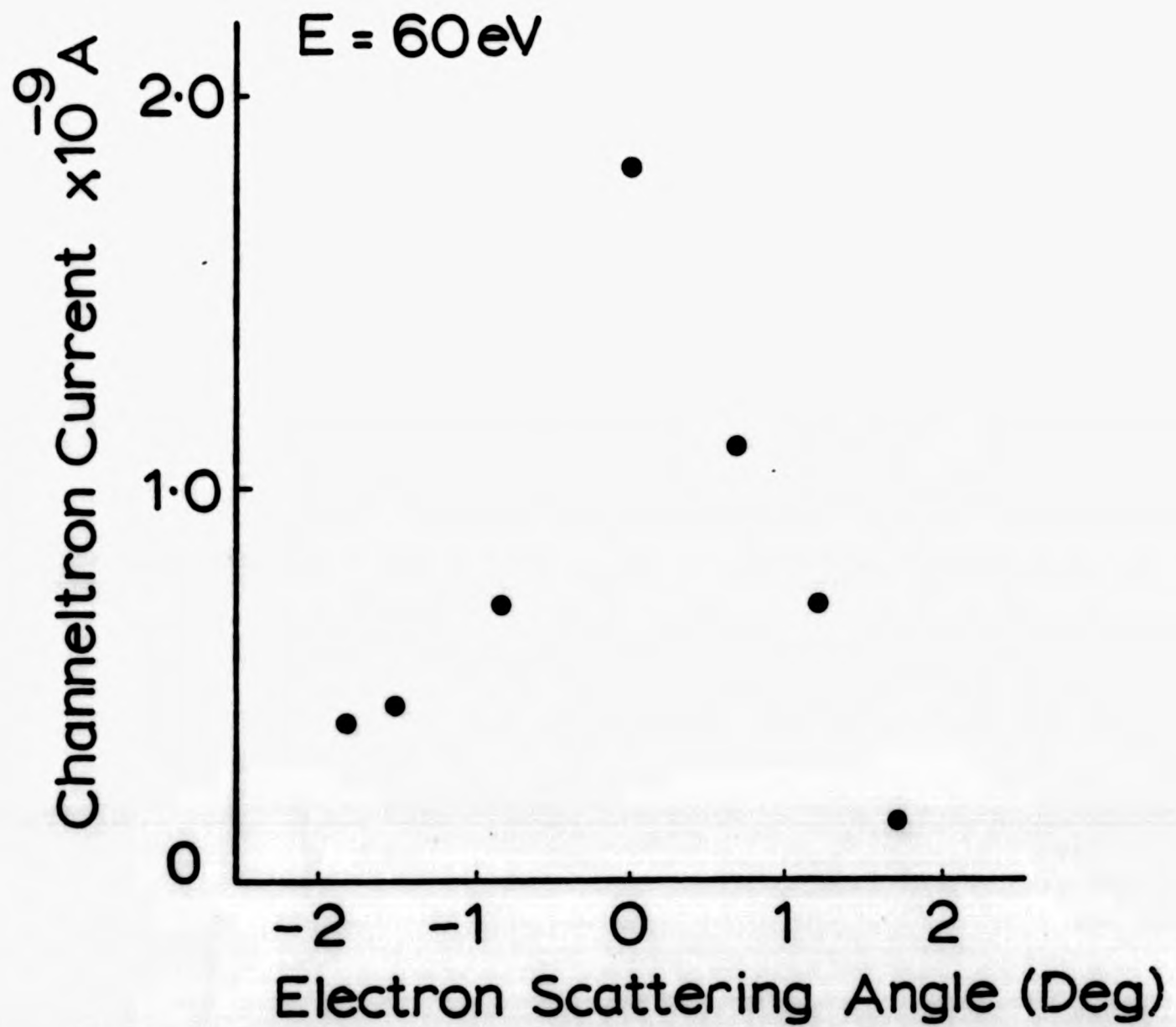


Figure (4-2): Angular distribution of the electron beam measured through the  $127^\circ$  electron analyser assembly.

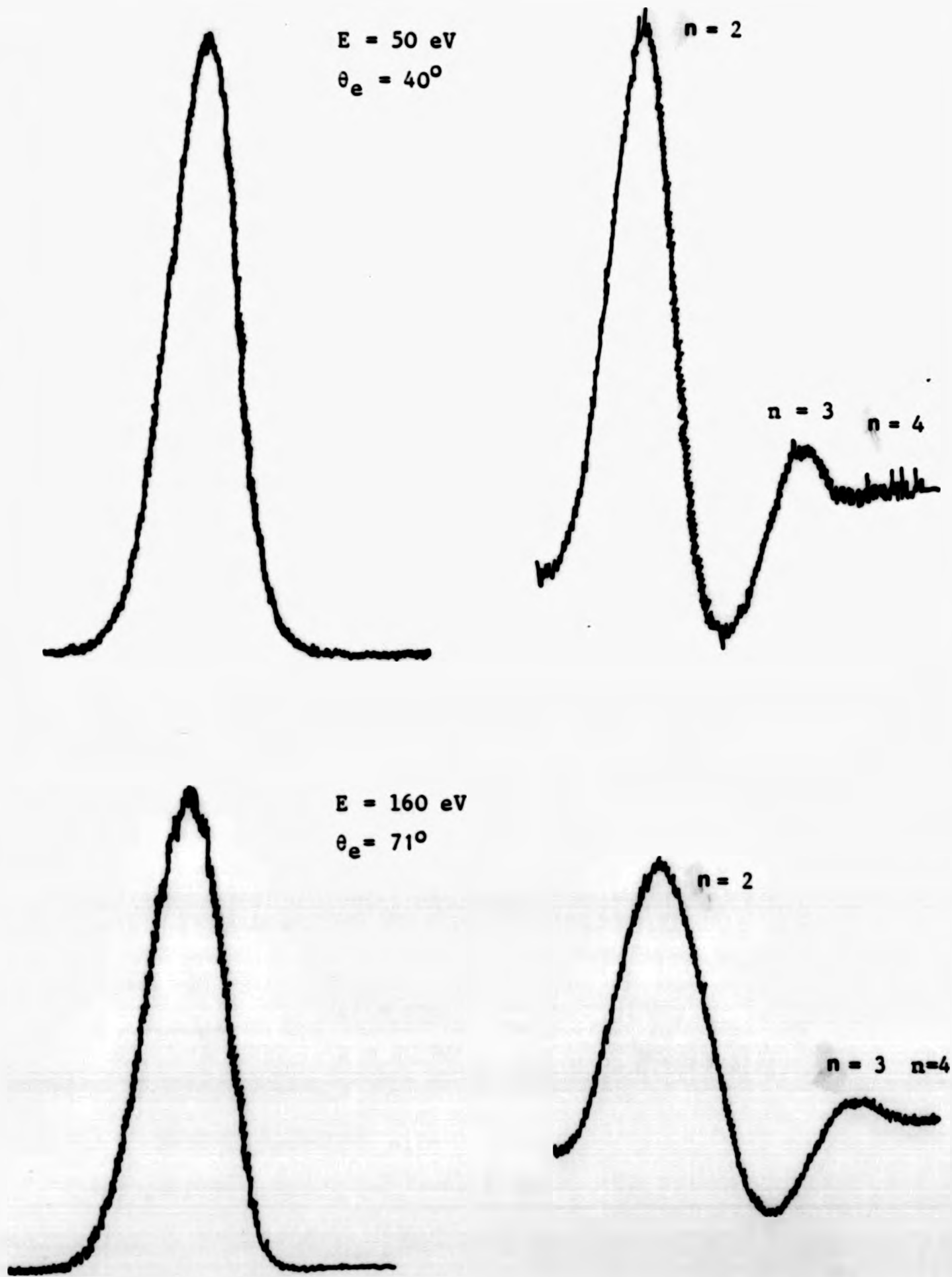


Figure (4-3): Typical elastic and energy loss spectra of helium.

resolution of the electron analyser and the electron gun is obtained by measuring the FWHM of the energy loss peak. This was found to be approximately 0.8 eV Fig.(4-3 ). The larger part of this width is caused by the tungsten filament used as the cathode of the electron gun.

The energy loss spectra shows three peaks corresponding,  $n=2$ , 3 and 4 respectively. In the present work the  $2^1P$  and  $3^1P$  states were studied.

The energy levels of He are shown in figure (4-4).

#### 4.2. Photon Signal

##### 4.2.1. Alignment of the Photon Detector

The alignment of the photon detector for the angular correlation measurements was carried out as follows: The photon detector was placed at  $0^\circ$  (in front of the electron gun) and the entrance aperture of the photon detector was observed from the cathode side. The alignment is correct when the centre of the entrance aperture coincides with the centre of the apertures of the electron gun intercepting the helium nozzle.

The alignment of the optical system for the polarization correlation measurements is described in chapter (3.6.2.).

##### 4.2.2. Photon Detection

Stray photons cause a serious problem in all light intensity measurements. Such photons either come from light sources inside the vacuum chamber or from outside.

The outside effect can be excluded through careful design of the photomultiplier housing. Great care has been taken in the design of the brass housing and its attachment to the system, to keep the photomultiplier tube in complete darkness.

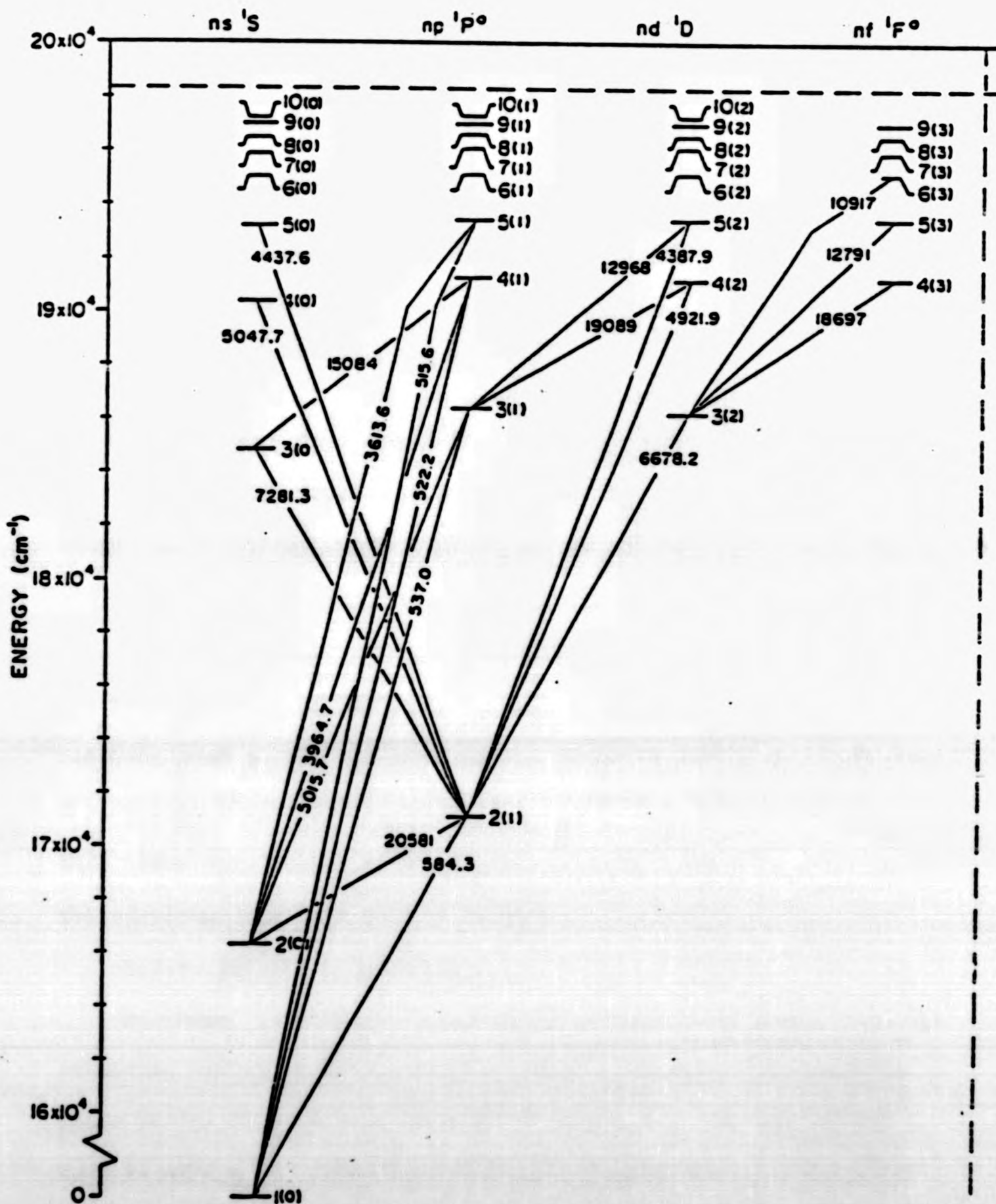


Figure (4-4): Energy level diagram for HeI. Wavelengths in Å.

The two light sources inside the vacuum system are the cathode of the electron gun and the ion gauge filament. To minimize the reflected cathode light, the helium nozzle and the interaction region were carefully sooted, and the gun was adjusted in such a way that any direct light from the cathode would pass just above the top of the helium nozzle. The ion gauge filament was thoroughly shielded. The total dark current was 100 Hz, 52% from the cathode light of the electron gun filament, 27% from the ion gauge filament and 21% from the tube.

#### 4.2.3. Single Photon Polarization

The transmitted light observed in y-direction is expected to be partially polarized either parallel or perpendicular to the direction of the electron beam (z-axis). For 80 eV the polarization should be  $\approx 23\%$  (Moustafa (1968)), so that the minimum single photon count rate is expected for a transmission angle of the polarizer of  $\alpha = 90^\circ$ , and this was checked by measuring the single photon rate for  $\alpha$  between  $0^\circ$  and  $180^\circ$ . The general cosine function (eq. 4.6) has been used to fit our data and the result is shown in Figure (4-5). The minimum single photon count rate is obtained at  $\alpha = 91^\circ$ . This means the setting of the linear polarizer axis with respect to the electron beam direction is correct.

#### 4.2.4. Resonance Radiation

Resonance trapping or imprisonment of radiation occurs when the radiation emitted from the excited atoms is absorbed by ground state atoms before reaching the detector (Moiseiwitsch and Smith 1968). Such an effect may significantly alter the nature of the radiation emitted since a state populated by this process (instead of by direct collision) will re-emit the light with an apparent depolarization of the primary impact radiation and with time delay. To avoid this

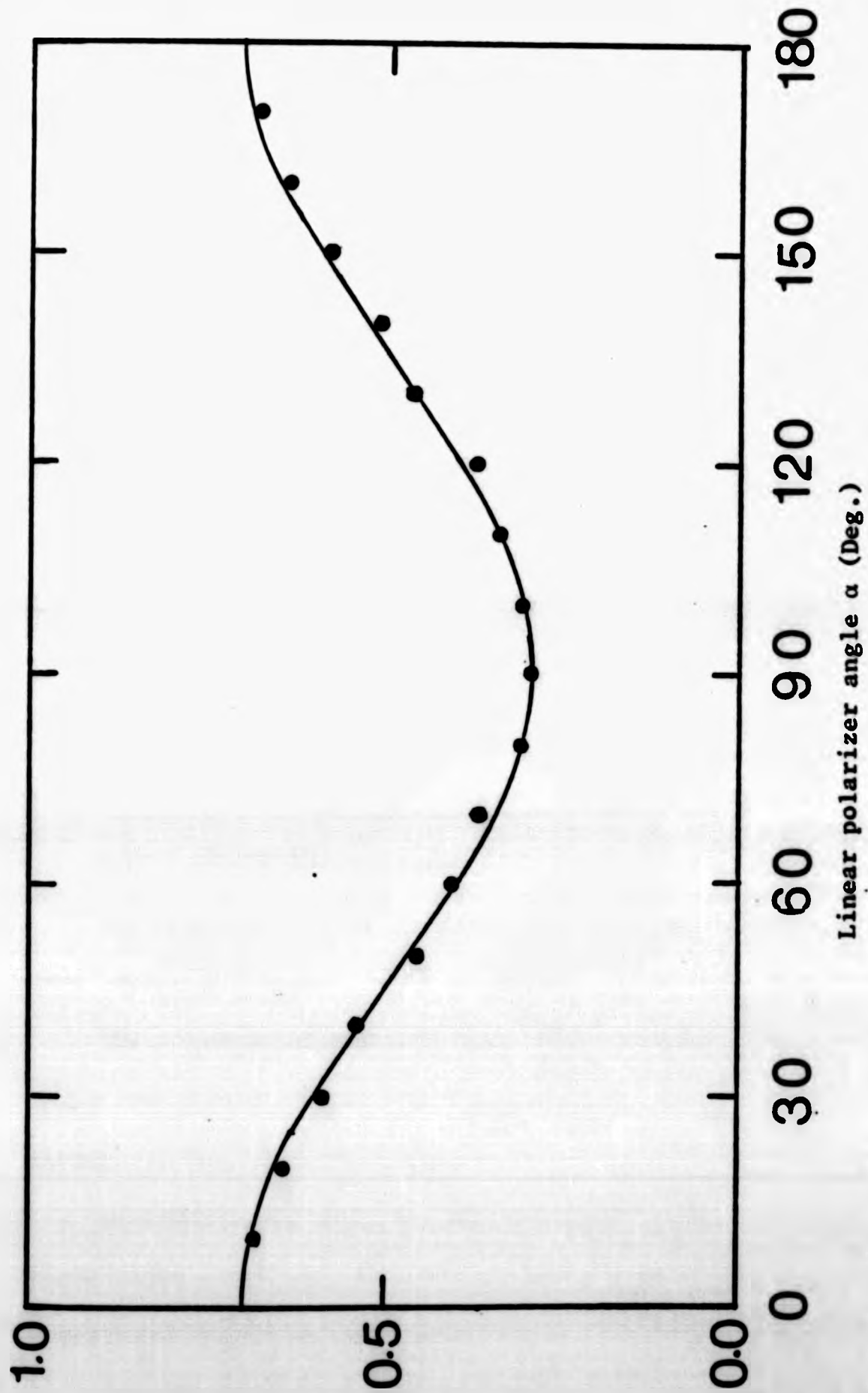


Figure (4-5): Photon singles count rate as a function of the linear polariser angle ( $\alpha$ ),  $E = 80$  eV. The curve is fitted using eq.(4.6) and gives the minimum at  $\alpha=91^\circ$ . The error bars are of the order of the full circles.

process, the gas pressure inside the excitation chamber should be kept in the linear region of the relation between the photon intensity and the gas pressure.

The coincidence signal for the  $3^1P_1$  state of helium has been studied as a function of the gas pressure for a constant incident electron energy of 80 eV and a constant electron scattering angle of  $\theta_e = 40^\circ$ . The measurement covered the pressure range of  $0.3 \cdot 10^{-6}$  Torr to  $2.0 \cdot 10^{-6}$  Torr as shown in fig. (4-6). No reduction of the normalized coincidence rate to the total number of the electrons was found in this range of pressure.

In the polarization correlation measurements the pressure has been kept below  $2.0 \cdot 10^{-6}$  Torr, to avoid any effect on the data collected due to resonance trapping. Any resonance trapping should increase the apparent width of the peak; in our measurements we did not find any change of the width.

#### 4.3. Coincidence Time Spectra and Analysis

##### 4.3.1. Coincidence Signal

The geometry of the electron-photon coincidence experiment has been shown in Figure (2-1).

The electron signal was fed into the start terminal of the TAC, while the photon signal was fed into the stop terminal of the TAC through an appropriate delay.

Electrons and photons from the same event have a definite time correlation resulting in a coincidence peak on a background of uncorrelated chance coincidences.

Typical time correlation spectra obtained from angular correlation measurements for the  $2^1P - 1^1S_0$  are shown in figure (4-7) taken at different electron scattering and

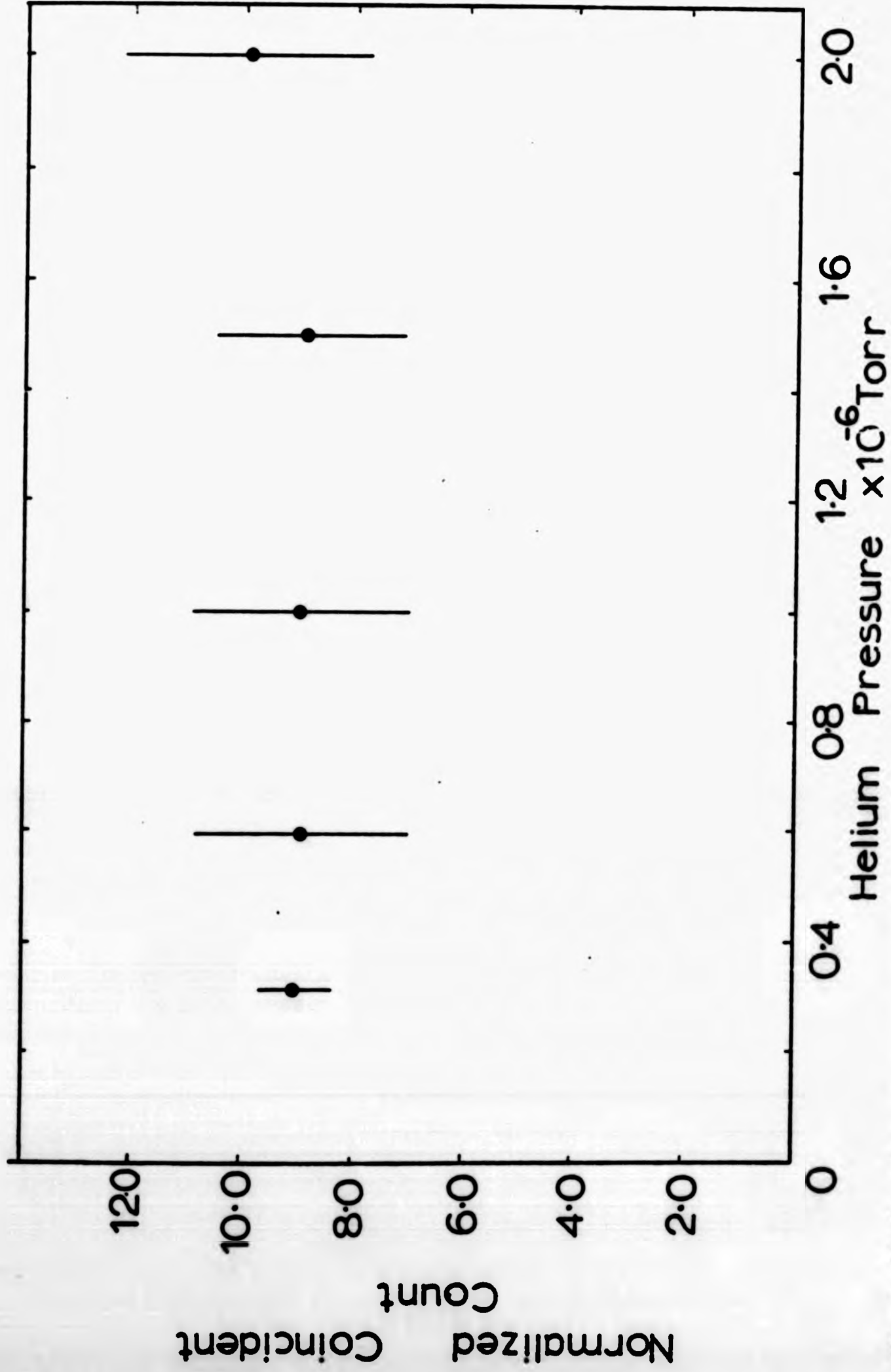
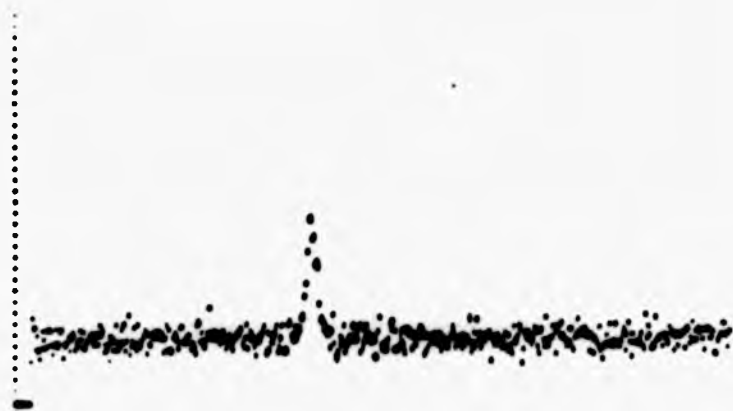


Figure (4-6): Dependence at the coincidence signal (linear polarization measurements) on the pressure at an incident energy of 80 eV for the  $3^1P$  state (error bars indicate  $\pm 1$  standard deviation). Electron scattering angle  $40^\circ$  and polarization angle  $\alpha = \pm 45^\circ$ .



TIME 011890 CUR 0512=011890

$\theta_e = 20^\circ$   
 $\theta_\gamma = 132^\circ$   
 $S = 186 \pm 18$   
 $N = 0.587 \pm 0.058$   
 $R_e = 280 \text{ Hz}$   
 $R_\gamma = 1.6 \text{ KH}$



TIME 054002 CUR 0512=054002

$\theta_e = 37^\circ$   
 $\theta_\gamma = 132^\circ$   
 $S = 1106 \pm 69$   
 $N = 0.253 \pm 0.015$   
 $R_e = 780 \text{ Hz}$   
 $R_\gamma = 2.6 \text{ KH}_2$



TIME 141000 CUR 0512=141000

$\theta_e = 60^\circ$   
 $\theta_\gamma = 80^\circ$   
 $S = 244 \pm 31$   
 $N = 0.144$   
 $R_e = 120 \text{ Hz}$   
 $R_\gamma = 2.4 \text{ KH}_2$



TIME 117825 CUR 0512=117825

$\theta = 102^\circ$   
 $\theta_\gamma = 80^\circ$   
 $S = 146 \pm 36$   
 $N = 0.121 \pm 0.027$   
 $R_e = 100 \text{ Hz}$   
 $R_\gamma = 1.8 \text{ KH}_2$

Figure (4-7): Coincidence line correlation spectra for the He  $2^1P_1 - 1^1S_0$  (58.4 nm) transition (angular correlation measurements) for an electron incident energy of 50 eV.

photon angles.

Coincidence time spectra obtained from electron-photon polarization correlation measurements for the  $3^1P - 2^1S$  transition are shown in figure (4-8) taken at different scattering and linear polarization angles.

The true coincidence peak is spread over several channels by the finite decay time of the excited atoms of a few nsec and the resolution time of the electronic system ( $\leq 5$  nsec).

#### 4.3.2. Coincidence Analysis

The following method was used to calculate the number of true coincidence counts and the error in the number of true coincidences.

Figure (4-9) shows a schematic diagram of the coincidence spectrum in the MCA. It is divided into three regions  $x_2 - x_1$ ,  $x_3 - x_2$  and  $x_4 - x_3$ , with corresponding coincidence counts  $N_1$ ,  $N_2$  and  $N_3$  where,  $N_1$  and  $N_3$  are related to the chance coincidence events.

The number of random coincidences  $B$  under the coincidence peak is given by

$$B = \frac{(N_1 + N_3) (x_3 - x_2)}{(x_2 - x_1) + (x_4 - x_3)} \quad 4.1$$

The number of true coincidences,  $N_T$ , is

$$N_T = N_2 - B \quad 4.2$$

The error  $\delta N_T$  (standard deviation) of the number of real coincidences is given by

$$\delta N_T = \sqrt{N_2 + \left[ \frac{(x_3 - x_2)}{(x_2 - x_1) + (x_4 - x_3)} \right]^2 (N_1 + N_3)} \quad 4.3$$



E = 80 eV  
 $\theta_e = 20^\circ$   
 $\alpha = 65^\circ$   
S =  $248 \pm 27.9$   
N =  $0.66 \pm 0.07$   
 $R_e = 1.9 \text{ KHz}$   
 $R_Y = 420 \text{ Hz}$   
t = 18739

E = 80 eV  
 $\theta_e = 30^\circ$   
 $\alpha = -45^\circ$   
S =  $537 \pm 44$   
N =  $0.66 \pm 0.05$   
 $R_e = 1.6 \text{ KHz}$   
 $R_Y = 620 \text{ Hz}$   
t = 49035



E = 160 eV  
 $\theta_e = 60^\circ$   
 $\alpha = +45^\circ$   
S =  $111.1 \pm 32.9$   
N =  $0.55 \pm 0.16$   
 $R_e = 140 \text{ Hz}$   
 $R_Y = 830 \text{ Hz}$   
t = 180377

E = 120 eV  
 $\theta_e = 40^\circ$   
 $\alpha = -45^\circ$   
S =  $55.8 \pm 29.1$   
N =  $0.94 \pm 0.49$   
 $R_e = 720 \text{ Hz}$   
 $R_Y = 670 \text{ Hz}$   
t = 67729

Figure (4-8): Correlation spectra of the He  $3^1P - 2^1S$  (501.6 nm) transition (polarization correlation measurements).

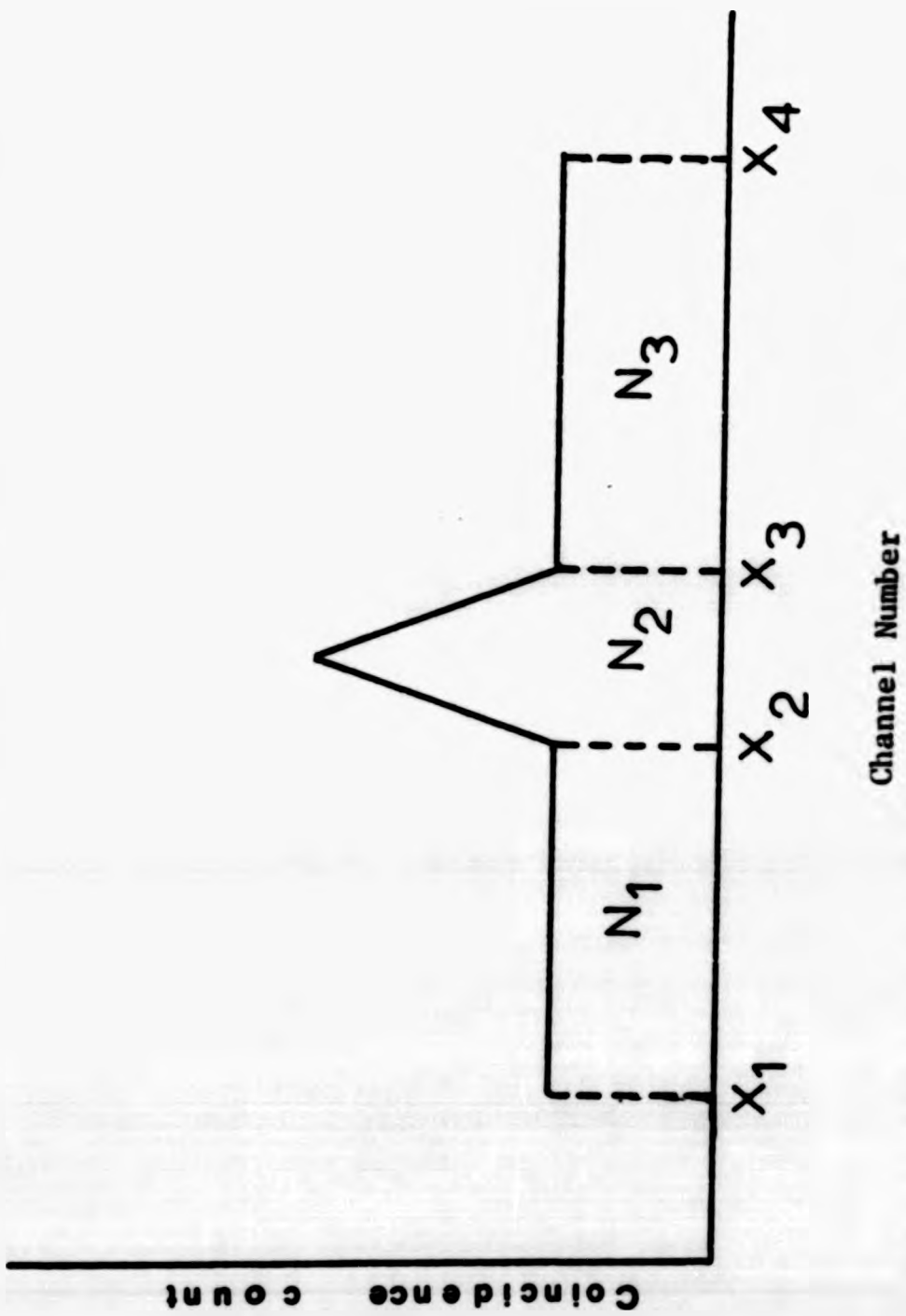


Figure (4-9): Data acquisition for coincidence analysis

The numbers  $N_T$  and  $\delta N_T$  were normalised to the total number of scattered electrons,  $N_e$ , collected during each run so that the effects of fluctuations of the electron beam current, the target density and of changes of the electron detector efficiency are largely eliminated. The resulting values of  $\frac{N_T}{N_e}$  and  $\frac{\delta N_T}{N_e}$  have been used to derive the values of  $\lambda$  and  $|\chi|$  in the angular correlation measurements and of the Stokes parameters in the polarization correlation measurements. Where appropriate, computer fitting routines have been employed.

#### 4.4. Analysis of the Angular Correlation Data

A series of nine coincidence spectra measured at different photon angles was used to determine the angular correlation curve for one scattering angle. Approximately 24 hours of data accumulation yielded one coincidence time spectrum at large scattering angles. The total number of coincidences corresponding to the measured coincidence peak is determined from the area under the peak in a time spectrum as described in (Chapter 4.3).

From the normalised coincidence rates as a function of the photon detector angle the excitation parameters  $\lambda$  and  $|\chi|$  for each angular correlation curve (see 5.1) are determined by fitting equation (2.15) to the experimental data.

The results reported in figure (4-10a and b) are weighted averages of several measured values according to the following equation

$$\mu = \frac{\sum x_i / \sigma_i^2}{\sum 1 / \sigma_i^2} \quad 4.4$$

In the calculation of the error in the averaged values we take into account the errors of the separate values. The uncertainty in the

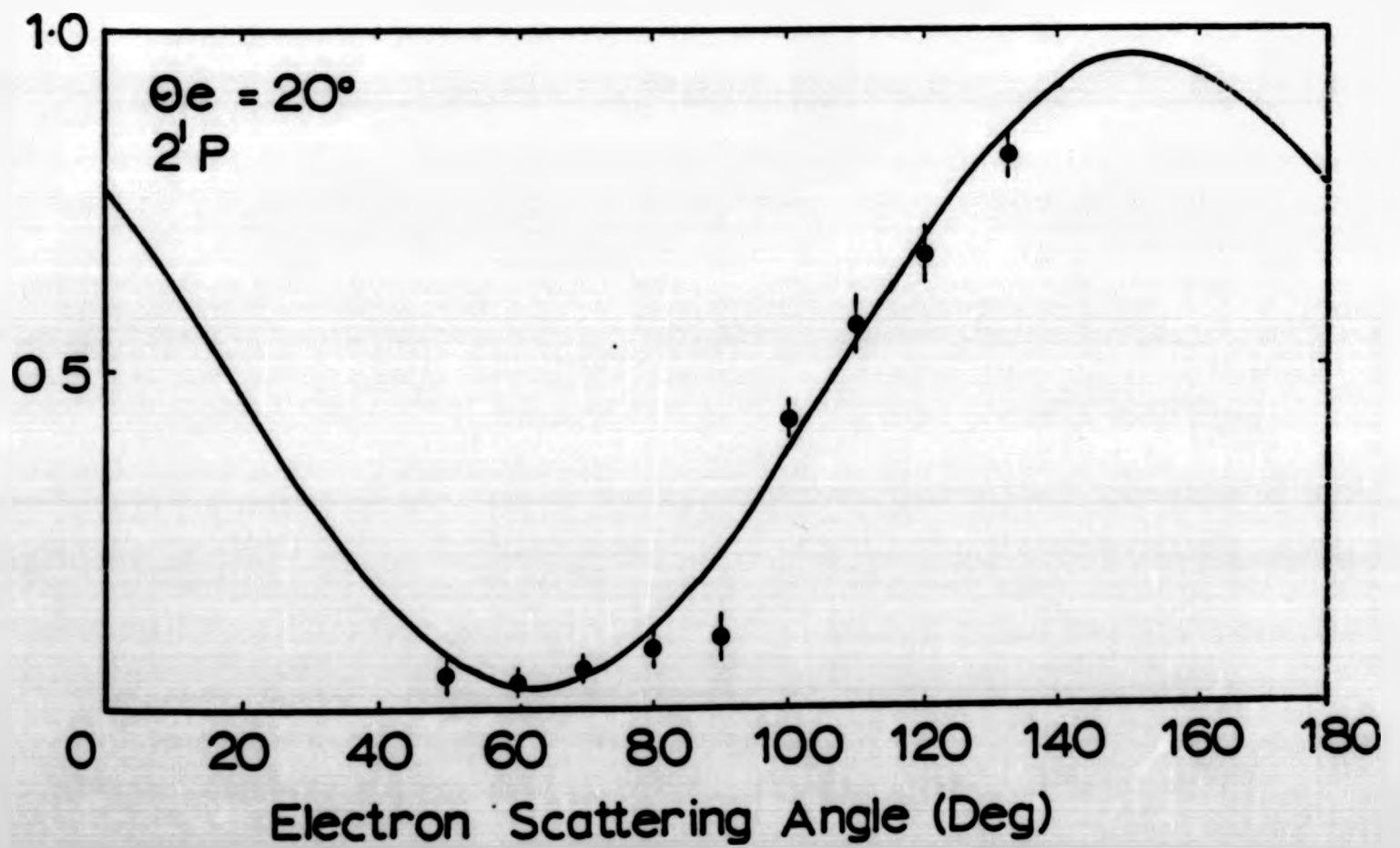
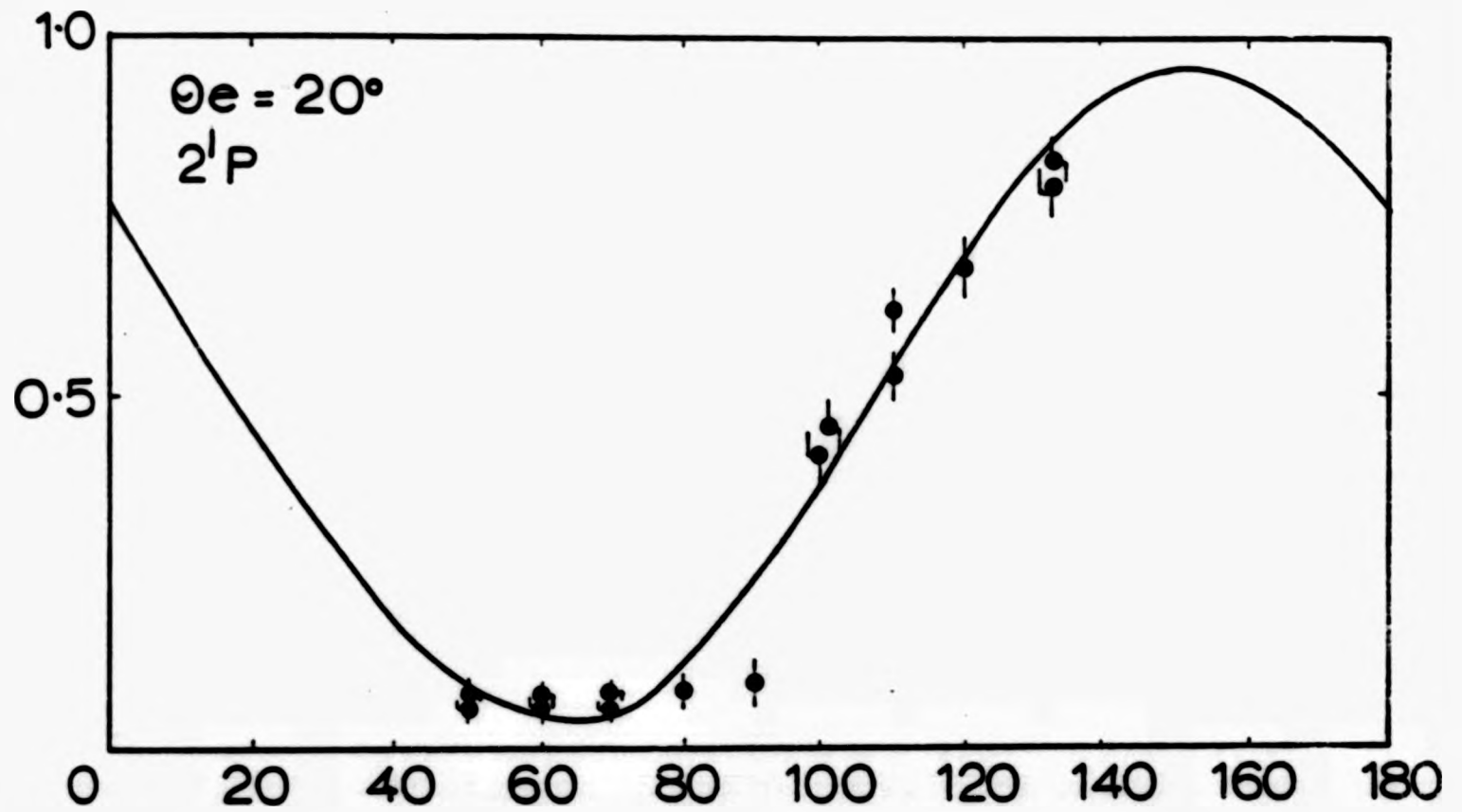


Figure (4-10): Typical electron photon angular correlation results in helium showing the normalized coincidence count rate as a function of electrons scattering angle, (a) all measured values, (b) average values.

mean  $\mu$  (equation 4.4) is estimated as follows

$$\sigma_{\mu} = \left( \frac{1}{\sum \frac{1}{\sigma_i^2}} \right)^{\frac{1}{2}} \quad 4.5$$

As an example of the present angular correlation measurements the weighted average values for  $\theta_e = 20^\circ$  are shown in figure (4-10b).

#### 4.5. Polarization Correlation Analysis

For each scattering angle the light intensity  $I(\alpha)$ , as a function of the angle  $\alpha$  between the transmission axis of the linear polarizer and the electron beam direction, is derived from the area under the coincidence peak (evaluated according to chapter 4.3.1. and normalised to the total number of scattered electrons). The number of true coincidences  $N_T$  represents the light intensity polarised under the angle  $\alpha$  (equation 2.23).

The general function for linear and circular polarization measurements is

$$F = A(1 + B \cos 2\alpha + C \sin 2\alpha) \quad 4.6$$

where B and C represent the values of the Stokes parameters  $\eta_3$  and  $\eta_1$  respectively in the linear polarization measurements and of  $\eta_3$  and  $\eta_2$  respectively in the circular polarization measurements.

Each Stokes parameter is obtained from two linearly independent measurements ( $\alpha$  differing by  $90^\circ$ ) in the same conditions. The measurements for each polarizer setting, i.e.  $I(\alpha)$ , at large electron scattering angles took approximately 24h.  $I_{RHC}$  and  $I_{LHC}$  are obtained from similar measurements at  $\alpha = \pm 45^\circ$  after a  $\frac{\lambda}{4}$  had been inserted with its marked axis (slow axis) parallel to the electron beam axis in front of the linear polarizer.

#### 4.5.1. Linear Polarization Measurements

The linear polarization measurements are obtained without the  $\frac{\lambda}{4}$  plate in the optical system. The angle  $\alpha$  of the linear analyser is measured from the positive Z-axis (the electron beam direction) in the same sense as the scattered electron angle. In most cases the Stokes parameters  $\eta_1$  and  $\eta_3$  (chapter 5.2) were derived directly from the measured coincidence rates  $I(45)$ ,  $I(135)$ ,  $I(0)$  and  $I(90)$  using equations (2-20 and 2-21), but in some cases measurements were taken for approximately eight values of  $\alpha$  and the results were fitted to the general function equation (4-6). The excitation parameters  $\lambda$  and  $|\chi|$  were derived from the measured Stokes parameters  $\eta_1$  and  $\eta_3$  as follows

$$\eta_1 = \frac{I(45) - I(135)}{I(45) + I(135)} = -2 \sqrt{\lambda(1-\lambda)} \cos\chi \quad 4.7$$

$$\eta_3 = \frac{I(0) - I(90)}{I(0) + I(90)} = 2\lambda - 1 \quad 4.8$$

Figure (4-11a and b) show typical electron-photon polarization correlation curves for the  $3^1P_1$  state of helium for the electron scattering angle  $50^\circ$  at incident electron energies of 80 and 120 eV respectively.

The background was the most difficult problem in the present measurements, especially at low energies and small scattering angles. At an incident electron energy of 50 eV the electron-photon polarization measurements could only be carried out for  $\theta_e > 45^\circ$  which is just outside the background electron range.

#### 4.5.2. Circular Polarization Analysis

Figure (2-3) showed a schematic diagram of the photon observation in the y direction which is perpendicular to the scattering plane (z-x plane), and of the arrangement of the optical system used in this experiment.

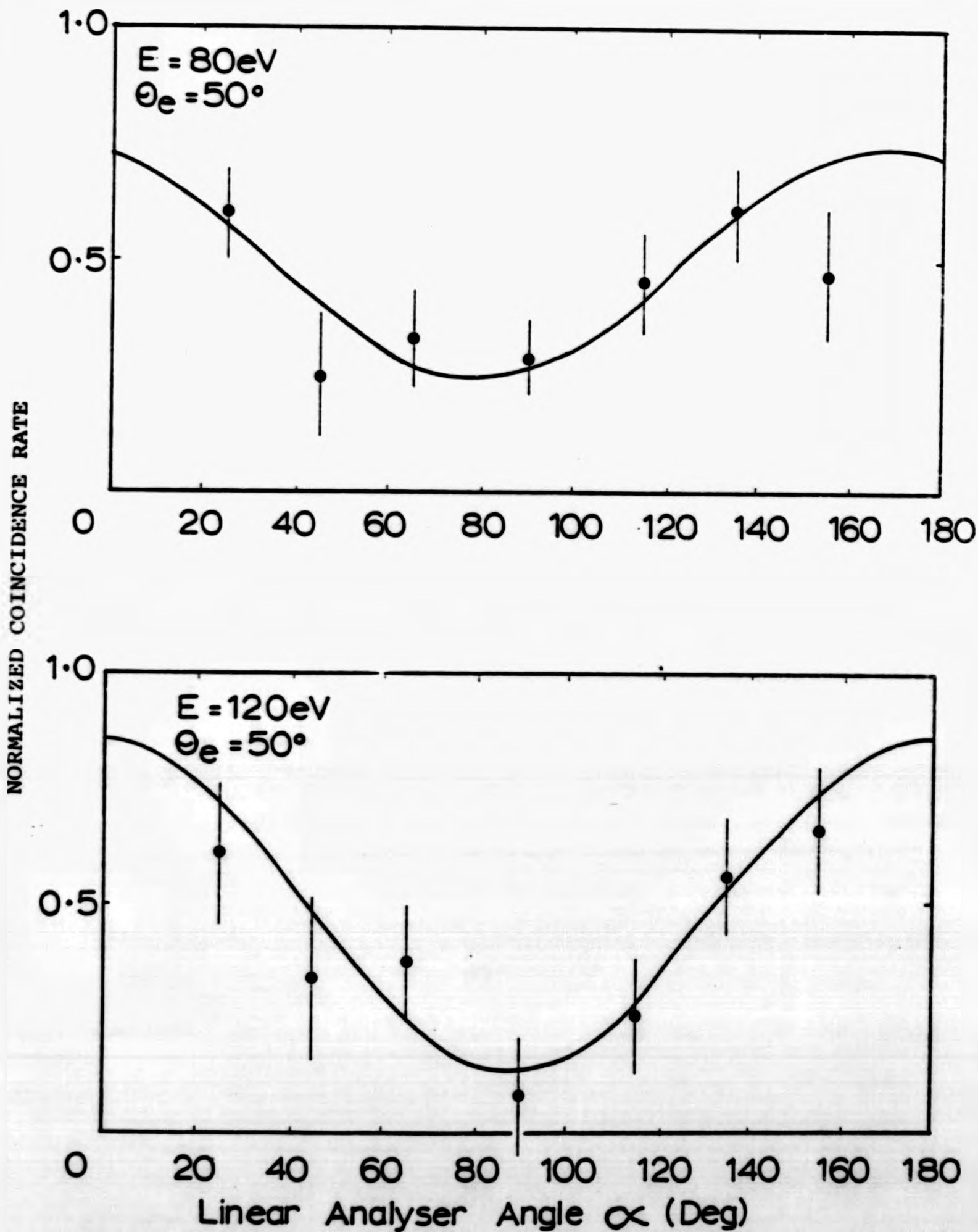


Figure (4-11): Typical electron-photon polarization correlation results in helium have the normalized coincidence count rate as a function of the linear polarizer angle  $\alpha$  for different incident energies for the electron scattering angle  $\theta_e = 50^\circ$ .

In order to create right hand circularly polarized light, the direction of the  $\vec{E}$  vector of linearly polarized light has to have an angle of  $+45^\circ$  with the slow axis (z-direction) of the  $\frac{\lambda}{4}$  plate. The light can be split into two components with equal amplitude along the z and x directions (figure 4-12a). The z- and x-components will be in phase then they enter the  $\frac{\lambda}{4}$  plate and the x-component is ahead of the z-components by  $90^\circ$  (one quarter wave) on exit from the  $\frac{\lambda}{4}$  plate. Thus the superposition of the two components leads to a clockwise rotation of the  $\vec{E}$  vector with constant amplitude (right hand circularly polarized light). Conversely, if the  $\vec{E}$  vector makes an angle of  $135^\circ$  with the slow axis of the  $\frac{\lambda}{4}$  plate (figure 4-12b), it will split into two components along the z- and x-directions which now are  $180^\circ$  out of phase when they enter the  $\frac{\lambda}{4}$  plate. The  $\frac{\lambda}{4}$  plate adds  $\delta = 90^\circ$  to the x-component and hence the x-component will be ahead of the z-component by  $270^\circ$ . Thus the superposition of the two components leads to anti-clockwise rotation of the  $\vec{E}$  vector with constant amplitude (left hand circularly polarized light).

For the analysis of right hand circularly polarized light, suppose the circular polarized light to be coming out of the plane of the paper (y-direction). The direction of revolution of the  $\vec{E}$  vector is clockwise. It can be decomposed into two orthogonal components along x and z, the x-component being a quarter of a period in front of the z-component. Suppose now the components transmitted through the  $\frac{\lambda}{4}$  plate (figure 4-12c). After retardation the x-component is  $\delta = 180^\circ$  ahead of the z-component and the superposition of the two components will give linearly polarized light with the  $\vec{E}$  vector at  $+135^\circ$  with respect to the z-axis.

Thus, light passing through the linear polarizer with its transmission axis at  $\alpha = 135^\circ$  was right hand circularly polarized light when it entered the  $\frac{\lambda}{4}$  plate and light passing through the

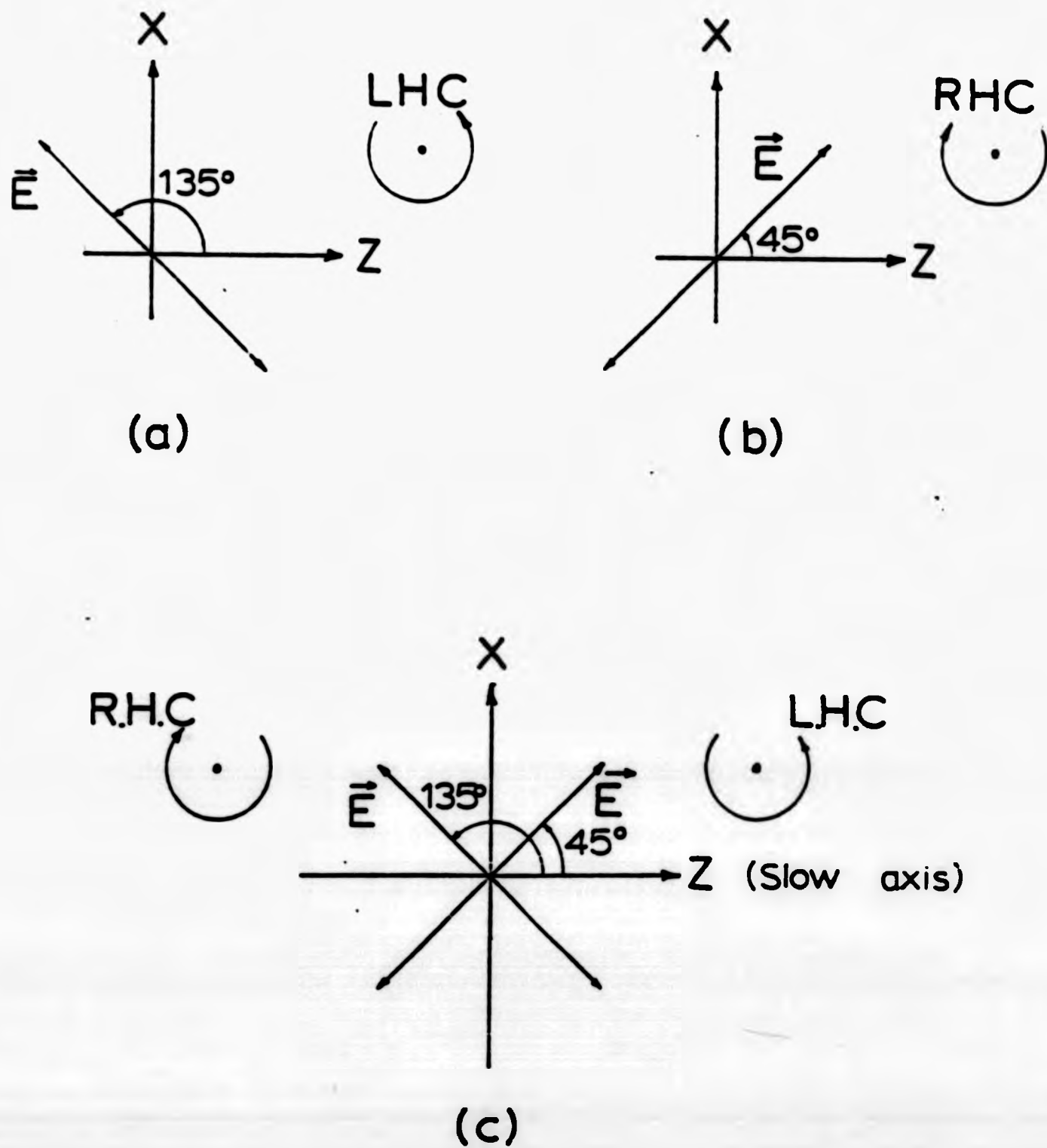


Figure (4-12): Creation and analysis of circularly polarized light.

(a) and (b) showing the  $\vec{E}$  vector incident on the  $\frac{\lambda}{4}$  plate and the resultant circular polarization,

(c) showing the circular polarization incident on the  $\frac{\lambda}{4}$  plate and the resultant  $\vec{E}$  vector on exit from the  $\frac{\lambda}{4}$  plate.

linear polarizer at  $\alpha = 45^\circ$  was left hand circularly polarized light.

## CHAPTER V

## RESULTS AND DISCUSSION

5.1. Angular Correlation Measurements

The angular correlation measurements in the present work have been carried out on the  $2^1P$  and  $3^1P$  states of helium for the electron impact energy of 50 eV.

Figures (5-1 to 5-5) show the angular correlation curves for the  $2^1P$  state, measured at different electron scattering angles. Figures (5-6 to 5-8) show angular correlation curves for the  $3^1P$  state. The full curves represent least squares fits to the experimental points using equation 2.15 as fitting function. The computer fits provide values for  $\lambda$  and  $|\chi|$  and these are tabulated in Table (5.1) as a function of the electron scattering angle for the  $2^1P$  and  $3^1P$  states. Also included are the values of  $\theta_{\min}$ , the moduli of the orientation vector  $|O_{1-}^{\text{col}}|$ , where  $O_{1-}^{\text{col}} = -[\lambda(1-\lambda)]^{\frac{1}{2}} \sin\chi$  and the values of the components of the alignment tensor  $A^{\text{col}}$  which are given as follows

$$A_0^{\text{col}} = (1-3\lambda)/2 \quad 5.1$$

$$A_{1+}^{\text{col}} = -(\lambda(1-\lambda))^{\frac{1}{2}} \cos \quad 5.2$$

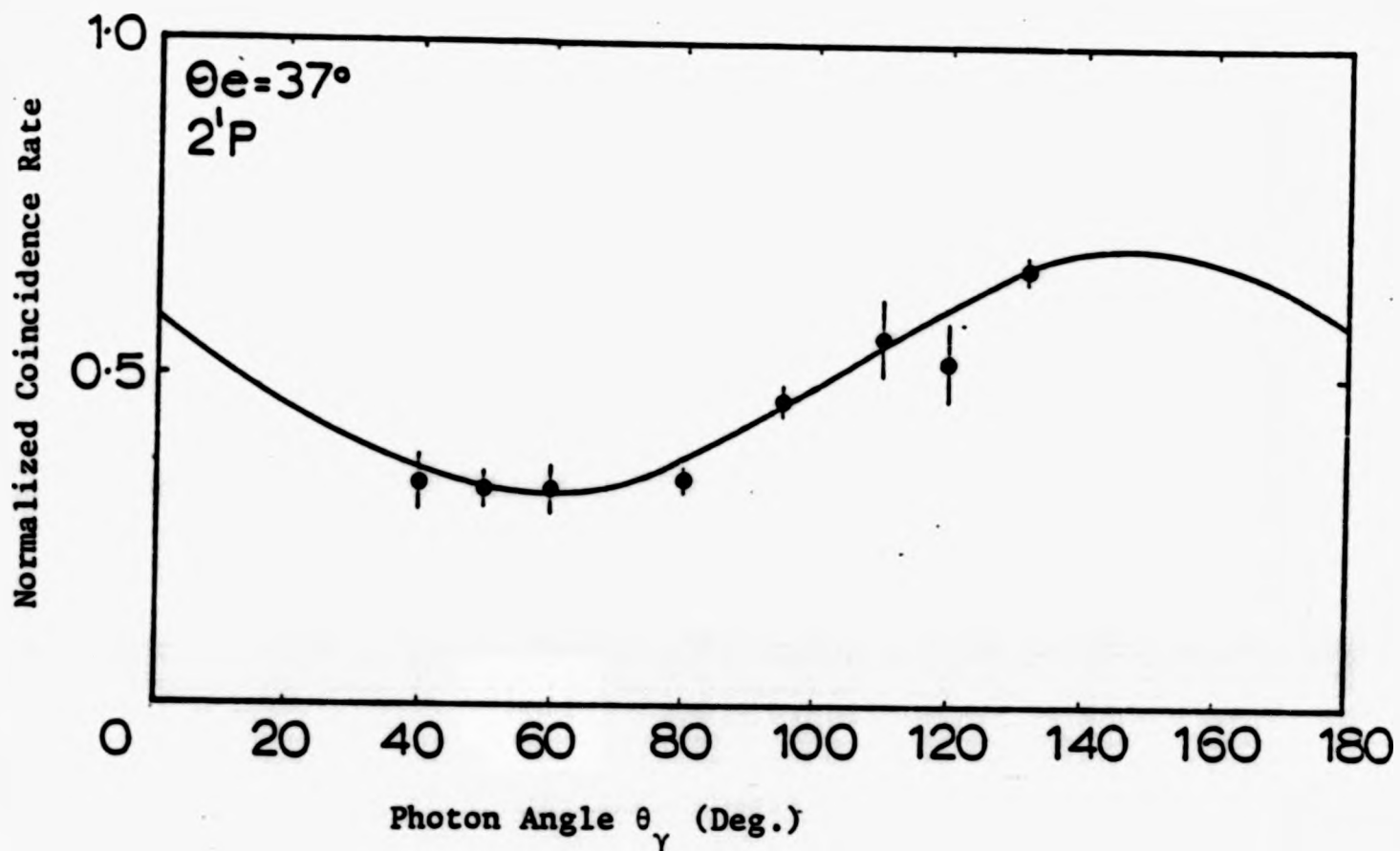
and  $A_{2+}^{\text{col}} = (\lambda-1)/2 \quad 5.3$

The measured values of  $\lambda$  for the  $2^1P$  state are shown in figure (5-9) together with previous experimental results of Eminyán et al. (1974), Tan et al. (1977) and MacAdams et al. (1980) and with theoretical calculations of Thomas et al. (1974) at 55.5 eV. Apart from the value at  $\theta_e = 20^\circ$  our points agree well with the experimental results of MacAdams et al. (1980).

Table (5-1): The excitation parameters of the  $2^1S_0$  and  $3^1P_1$  states in helium for incident energy 50 eV

Excited State	Electron Scatter- ing Angle (Deg.)	$\lambda \pm \Delta\lambda$	$X \pm \Delta X$	$ O_{1-}^{col} $	$ A_0^{col} $	$ A_{1+}^{col} $	$ A_{2+}^{col} $	$\theta_{min}$ (Deg.)
$2^1P$	20	0.220±0.034	0.438±0.130	-0.175±0.049	0.170±0.051	0.374±0.029	-0.781±0.040	53.324±1.152
	37	0.411±0.019	1.235±0.027	-0.464±0.005	-0.116±0.028	0.161±0.012	-0.589±0.019	61.197±0.883
	50	0.557±0.087	1.537±0.240	-0.829±0.008	-0.335±0.130	0.027±0.199	-0.443±0.087	16.044±0.315
	60	0.850±0.166	2.074±0.476	-0.312±0.164	-0.775±0.249	-0.172±0.168	-0.150±0.166	-26.185±2.200
	82	0.703±0.239	1.890±0.420	-0.433±0.117	-0.554±0.358	-0.143±0.184	-0.297±0.239	-35.232±4.572
	102	0.444±0.090	2.091±0.121	-0.430±0.029	-0.166±0.135	-0.236±0.052	-0.556±0.090	-77.222±0.586
$3^1P$	35	0.380±0.111	1.033±0.353	-0.465±0.050	-0.070±0.166	-0.137±0.154	-0.62 ±0.111	63.414±2.882
	45	0.668±0.100	1.728±0.084	-0.464±0.035	-0.502±0.150	-0.073±0.039	-0.332±0.100	-23.619±0.312
	55	0.726±0.270	1.838±0.318	-0.387±0.141	-0.589±0.405	0.220±0.190	-0.274±0.270	27.519±3.397

Figure (5-1)



Figures (5-1 to 5-5):

Electron-photon angular correlation results for the  $2^1P$  state in helium showing the normalized coincidence count rate as a function of photon scattering angle for electron scattering angles of  $37^\circ$ ,  $50^\circ$ ,  $60^\circ$ ,  $82^\circ$  and  $102^\circ$ , at an incident electron energy 50 eV. The solid line curves are chi-squared optimization of equation (2.15) to the experimental data. Error bars indicate  $\pm 1$  standard deviation.

Figure (5-2)

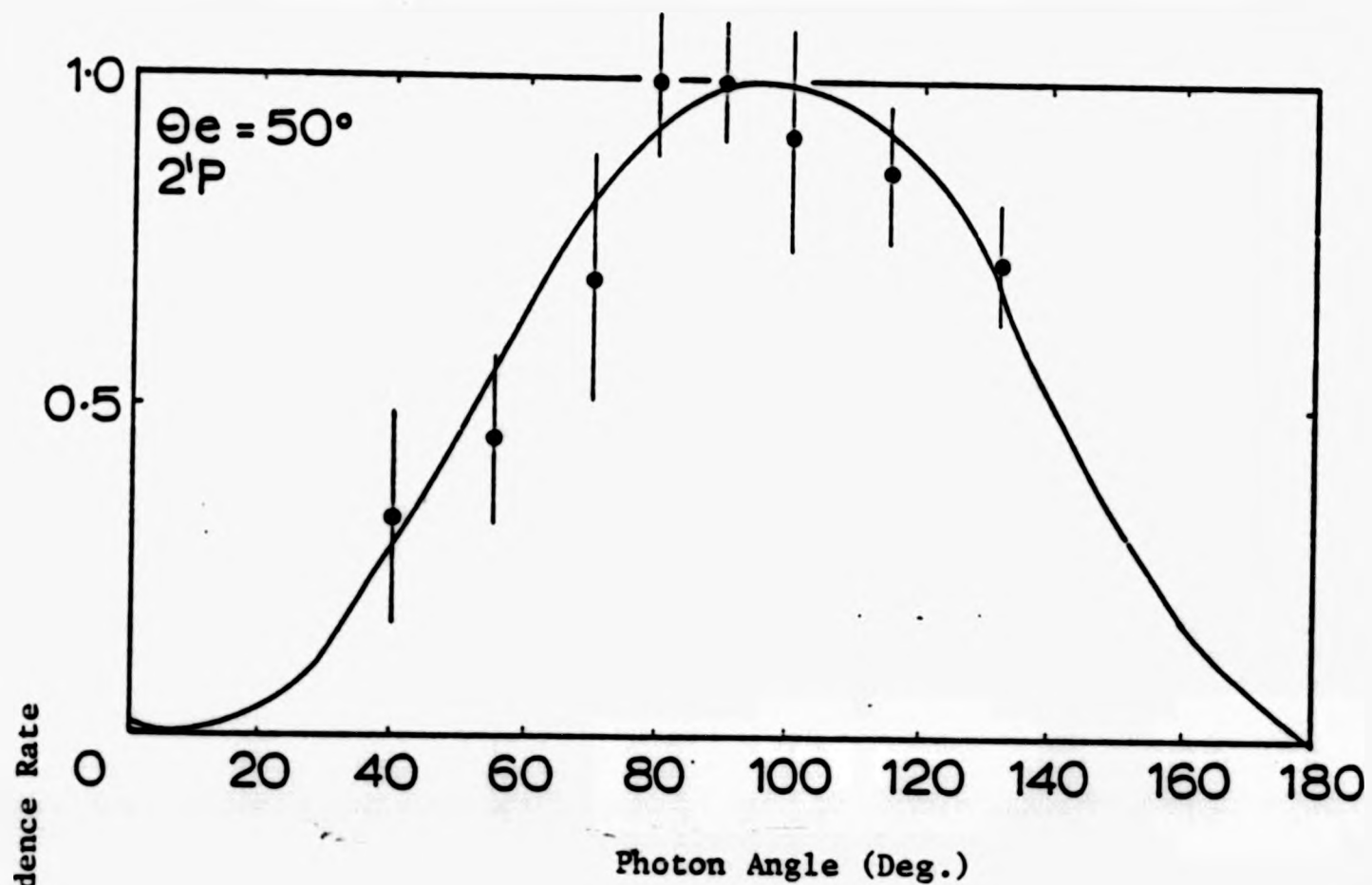


Figure (5-3)

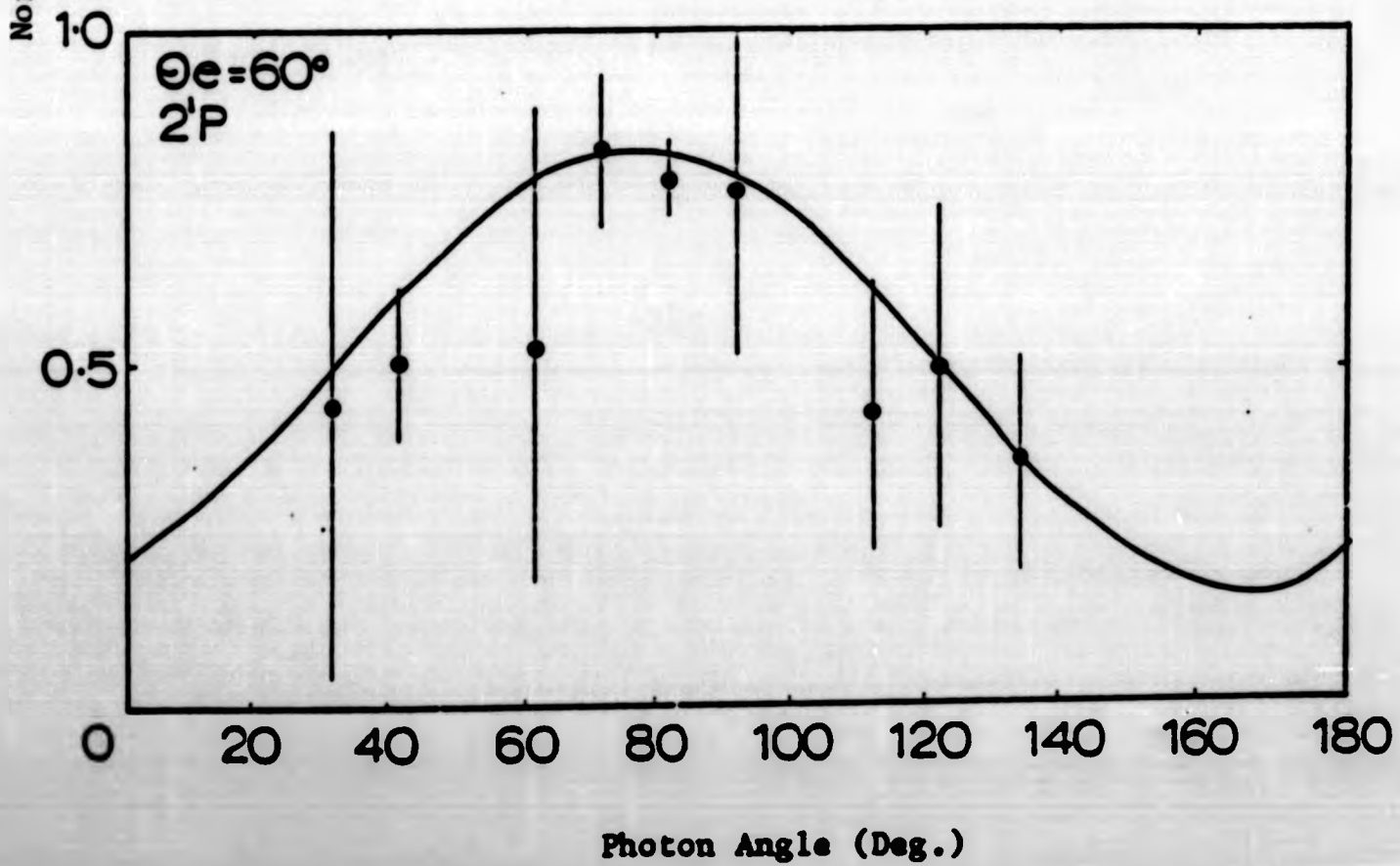


Figure (5-4)

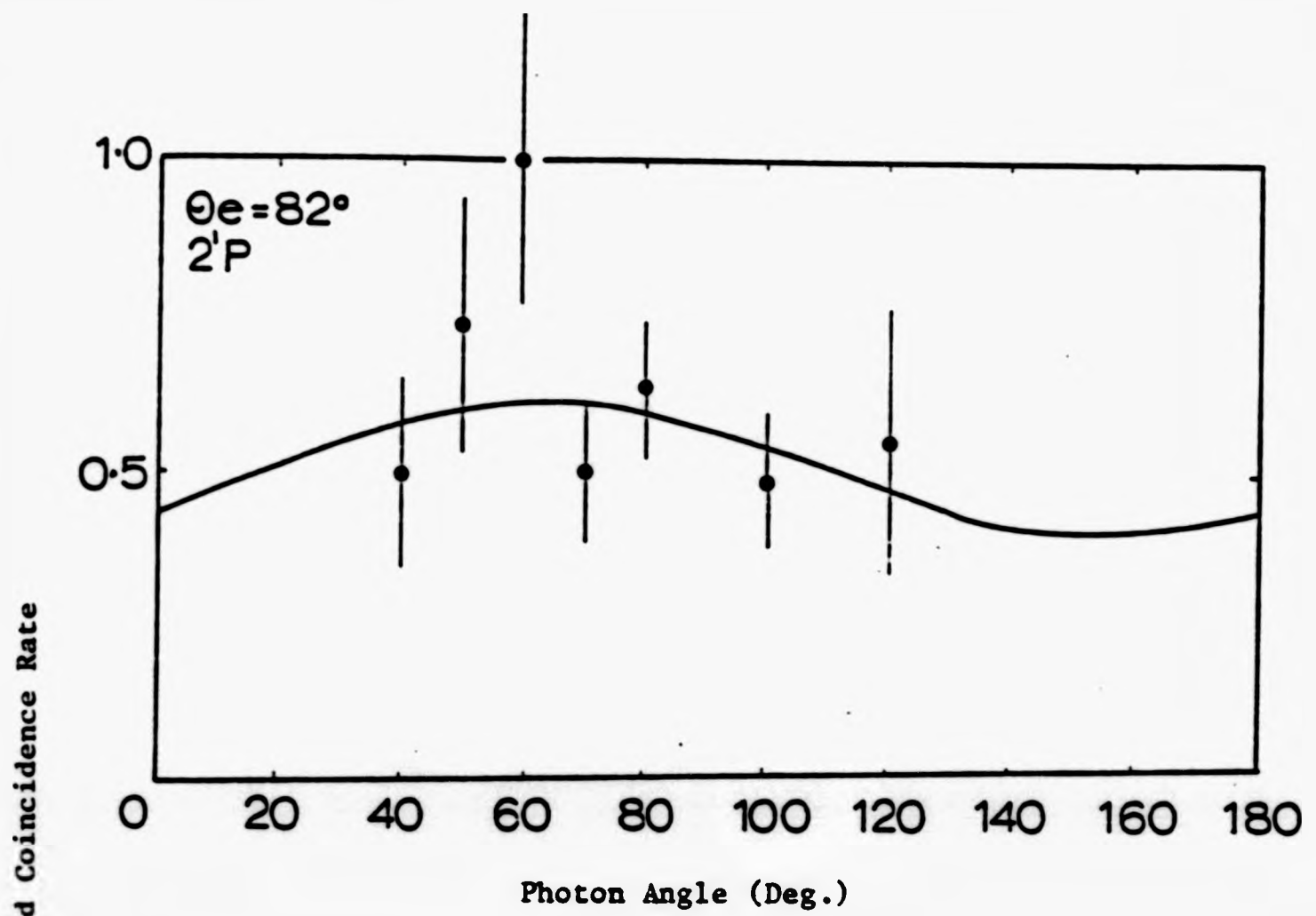


Figure (5-5)

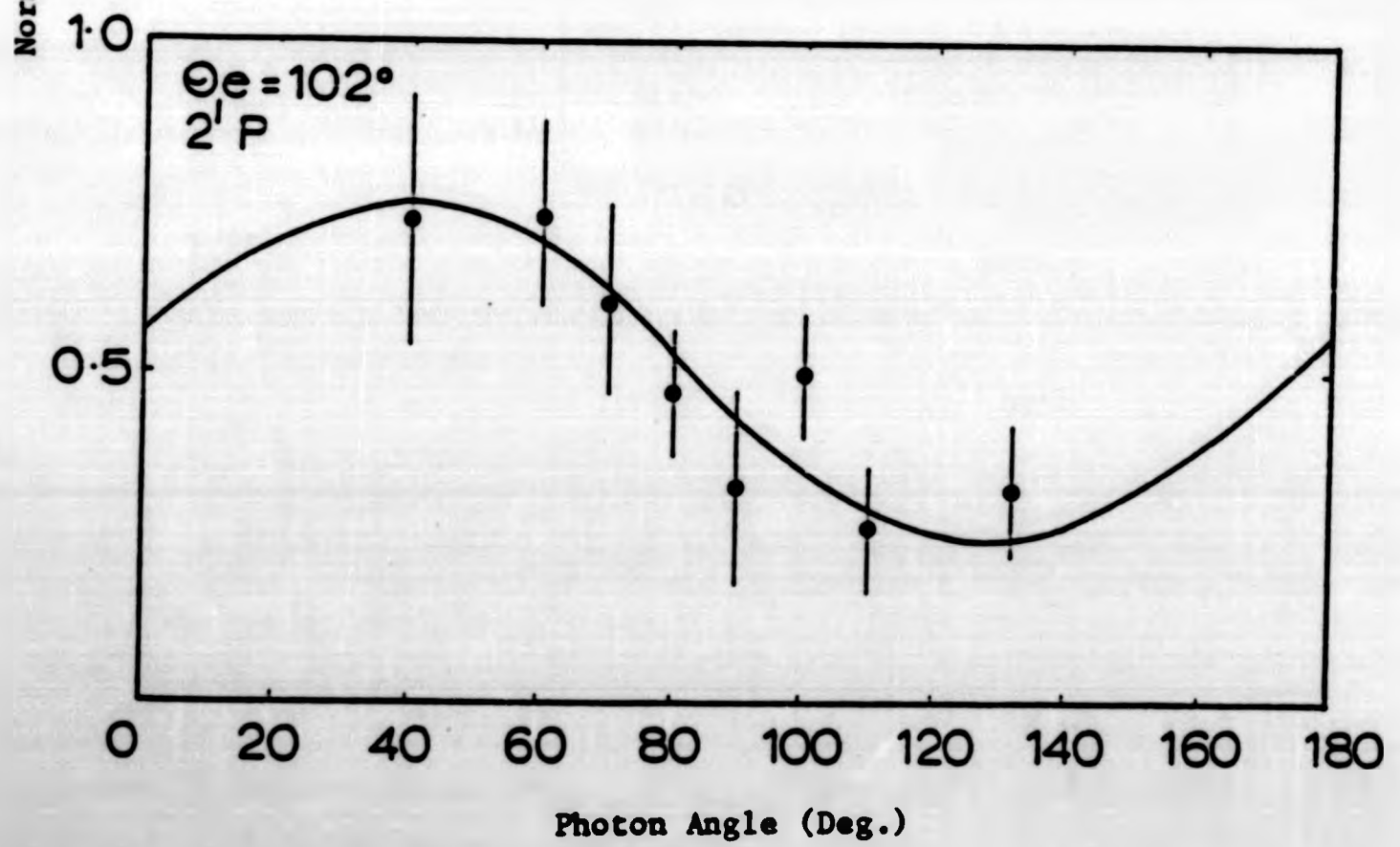
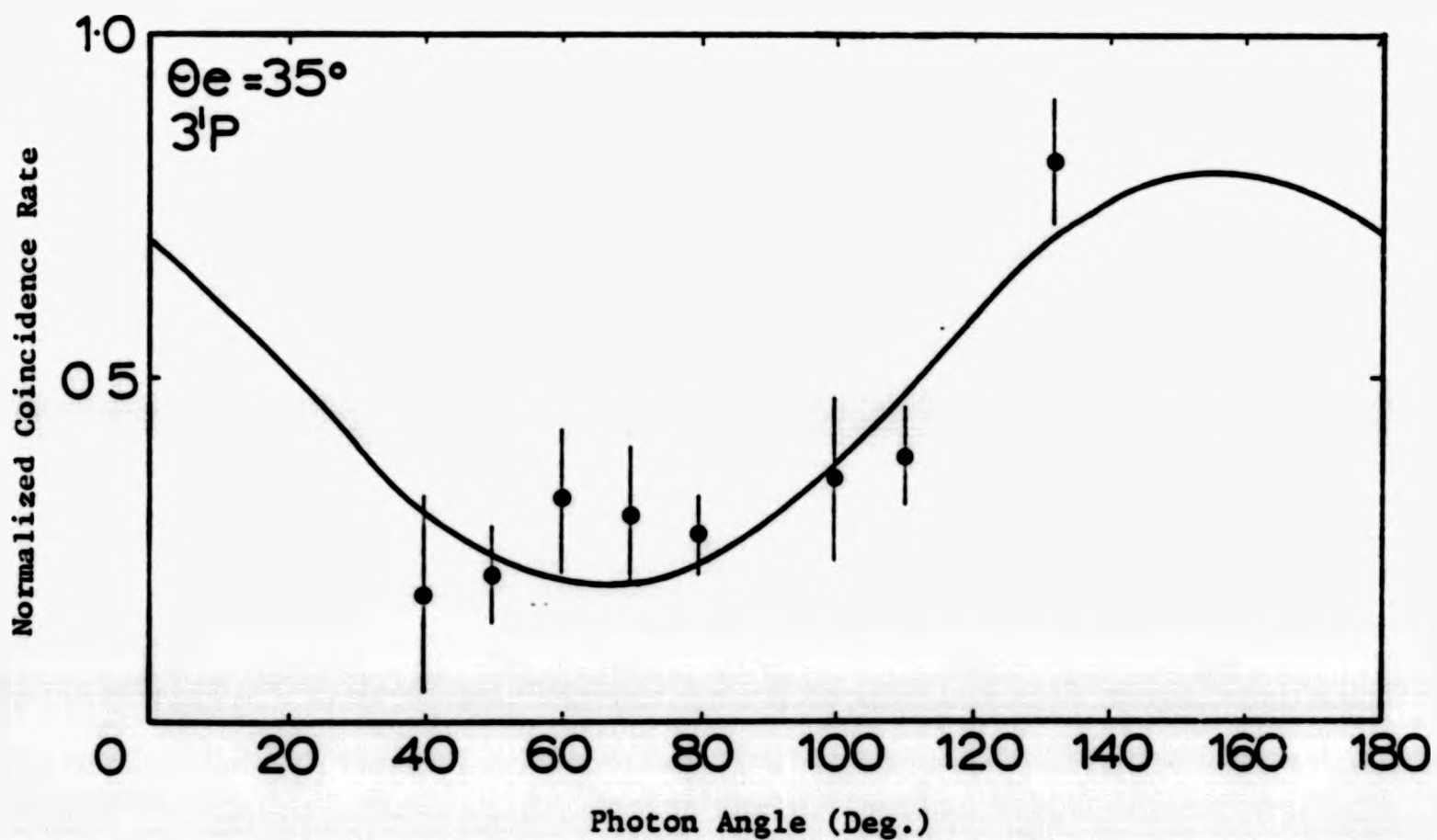


Figure (5-6)



Figures (5-6 to 5-8):

Electron photon angular correlations for the  $3^1P$  state in helium showing the normalized coincidence count rate as a function of photon scattering angle for electron scattering angles of  $35^\circ$ ,  $45^\circ$  and  $55^\circ$ , at an incident electron energy 50 eV. The solid line curves are chi-squared optimization of equation (2.15) to the experimental data.

Error bars indicate  $\pm 1$  standard deviation.

Figure (5-7)

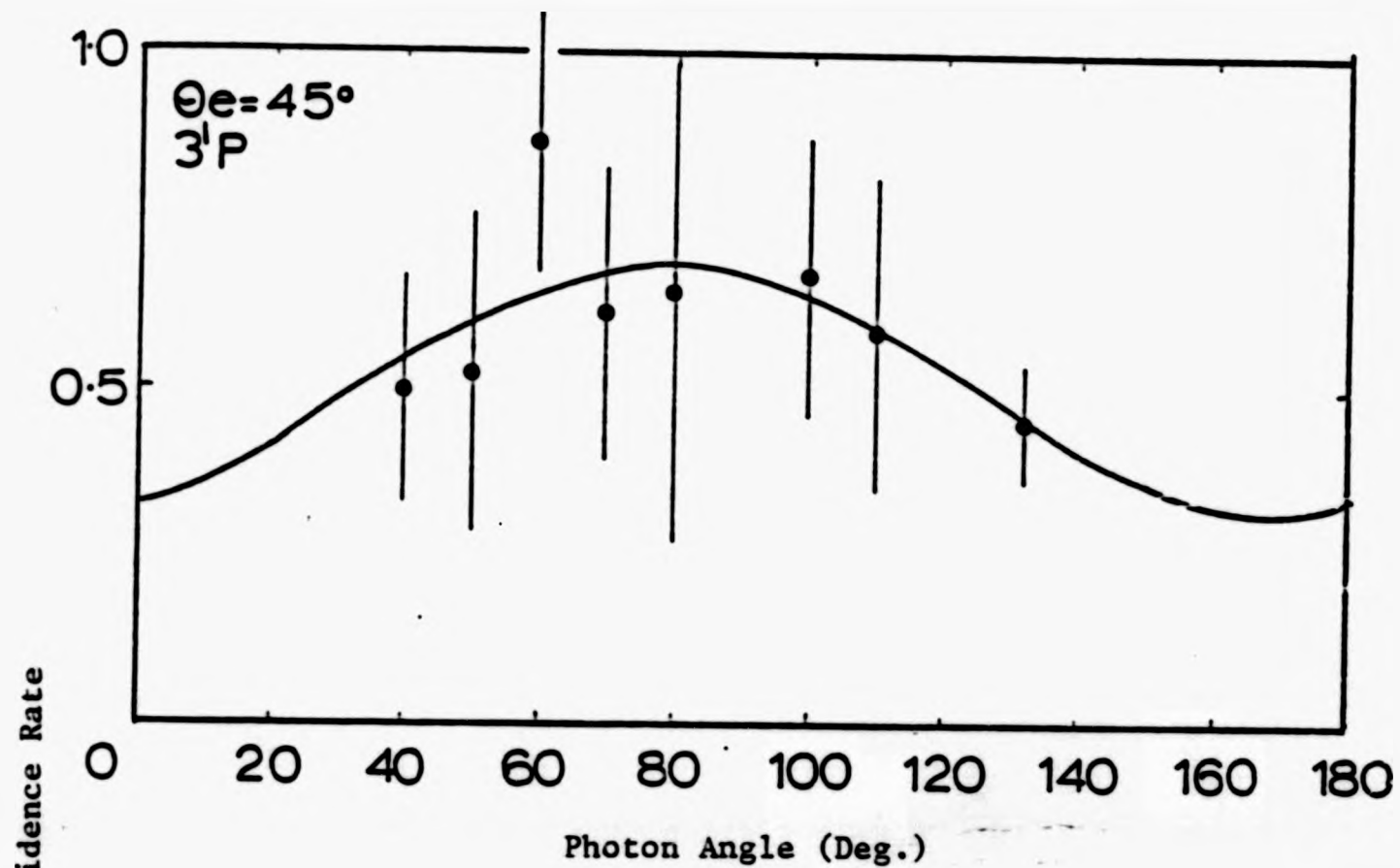
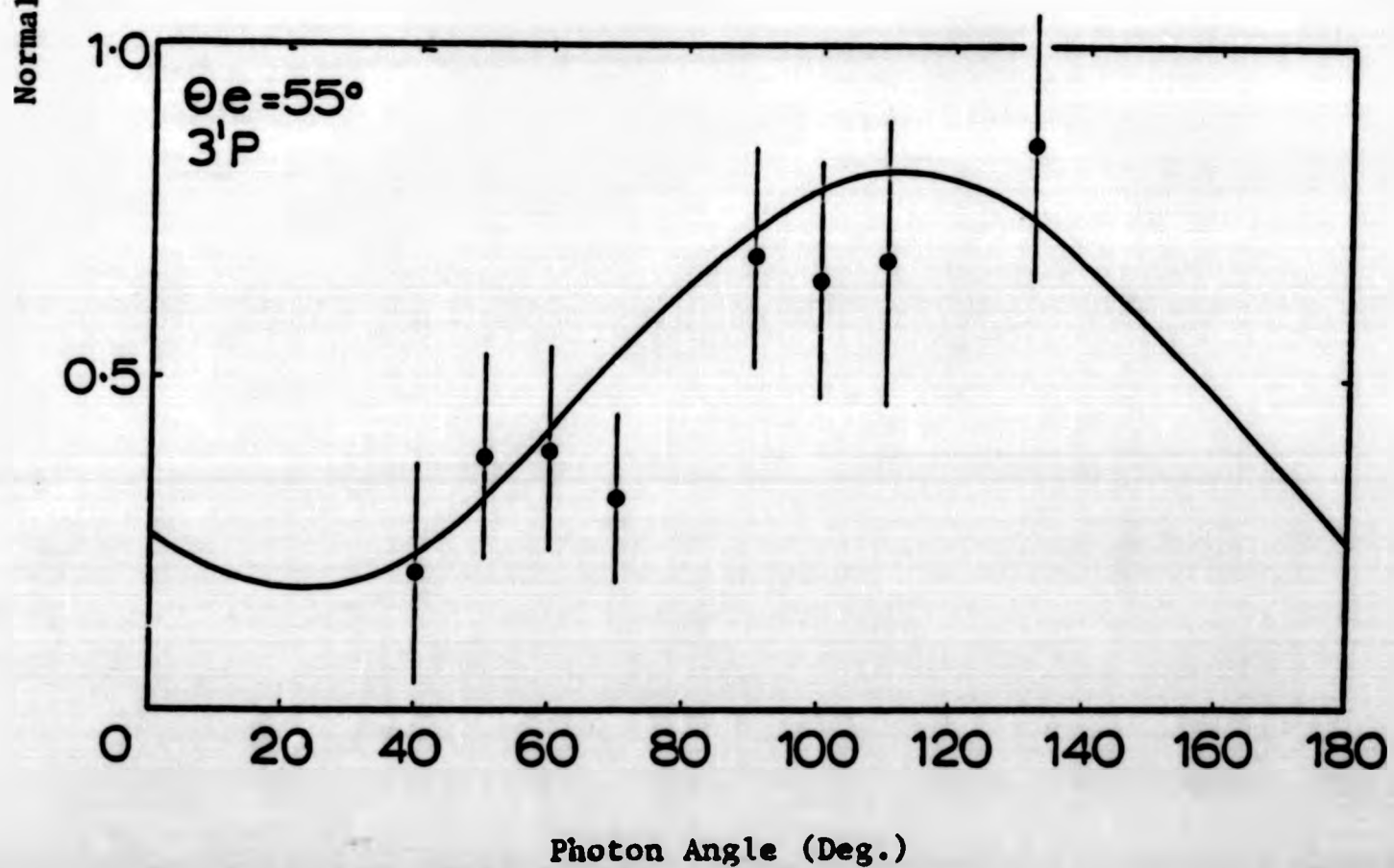


Figure (5-8)



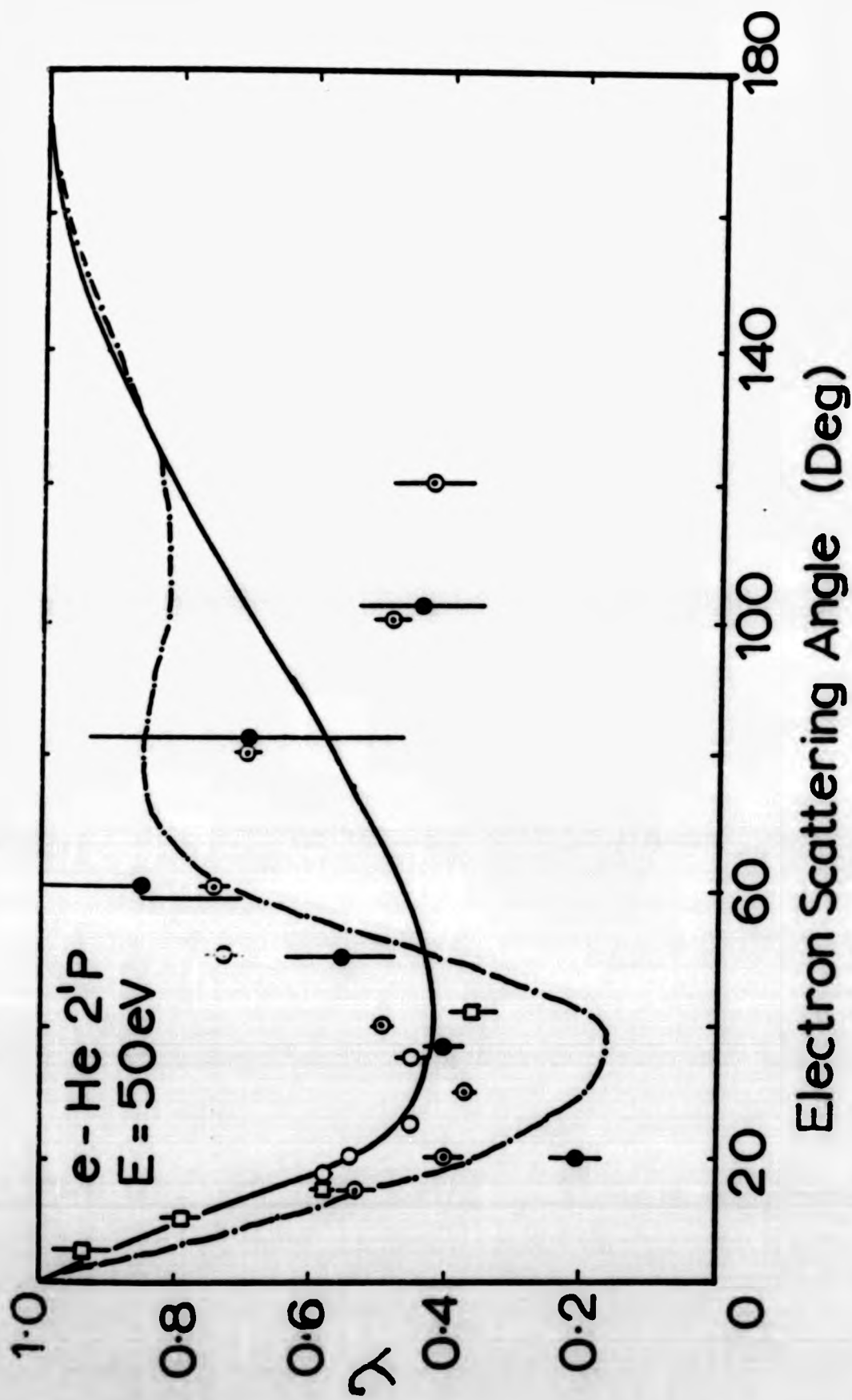


Figure (5-9): Variation of  $\lambda$  as a function of the electron scattering angle.  
● present values; □ Tan et al.(1977); ○ Eminyan et al.(1974);  
○ MacAdams et al. at 51.2 eV (1980); — FBA;  
- · - · - ·, Thomas et al. at 55.5 eV (1974).

Figure (5-10) shows the experimental values of  $\lambda$  for the  $3^1P$  state at an incident electron energy of 50 eV. For comparison  $\lambda$  values derived from present linear polarization measurements (see 4.5.1) are shown for the electron scattering angles  $35^\circ$ ,  $45^\circ$  and  $55^\circ$ . The present results are compared with experimental results of Eminyany et al. (1975) and with theoretical calculations of Meneses et al. (1980) and Scott et al. (1976). Apart from the scattering angle  $35^\circ$ , there is good agreement between the values of  $\lambda$  obtained in the present work and our results link well to the other experimental points.

Figure (5-11) shows the variation of  $|\chi|$  for the  $2^1P$  state as a function of the scattering angle. Again our results are compared with those of Eminyany et al. (1974) at energy 50 eV and of MacAdams et al. (1980) at energy 51.2 eV. The results agree over the whole range of electron scattering angles, considering that the error bars represent one standard deviation.

Figure (5-12) shows the variation of  $|\chi|$  for the  $3^1P$  state as a function of the electron scattering angle along with some of the values derived from the linear polarization measurements. The present results are compared with experimental values of Eminyany (1975) and with the theoretical calculations of Meneses et al. (1980) and Scott et al. (1976). Within the range of scattering angles there is good agreement between the present results and the theoretical curves.

## 5.2. Electron-Photon Polarization Correlations

### 5.2.1. Linear Polarization Measurements

The measurement of the linear polarization correlations in the present work has been described in chapter (4.5.2).

The Stokes parameters  $\eta_1$  and  $\eta_3$  for the linear polarization correlation are derived using the equations (2.34 and 2.33) and the

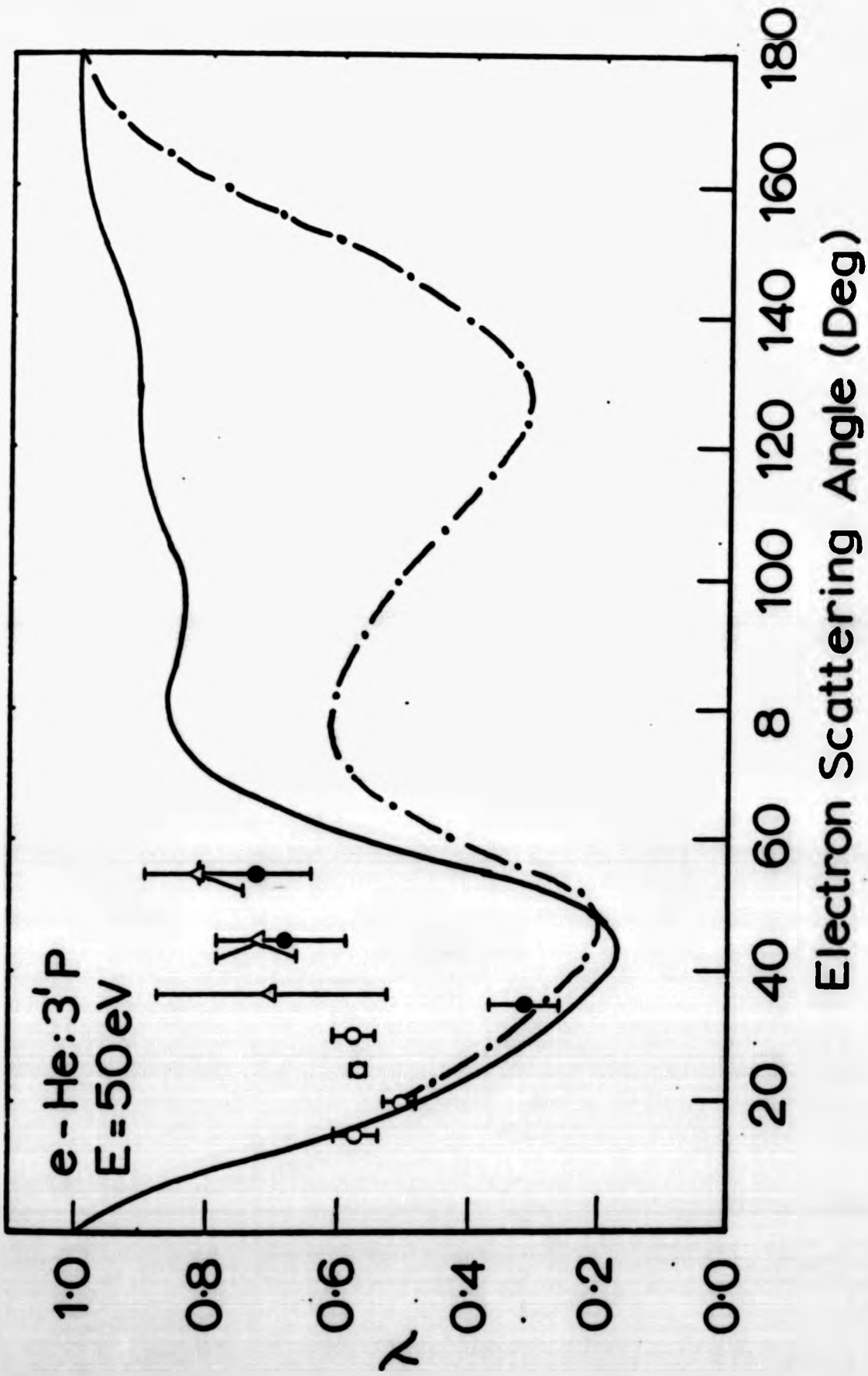
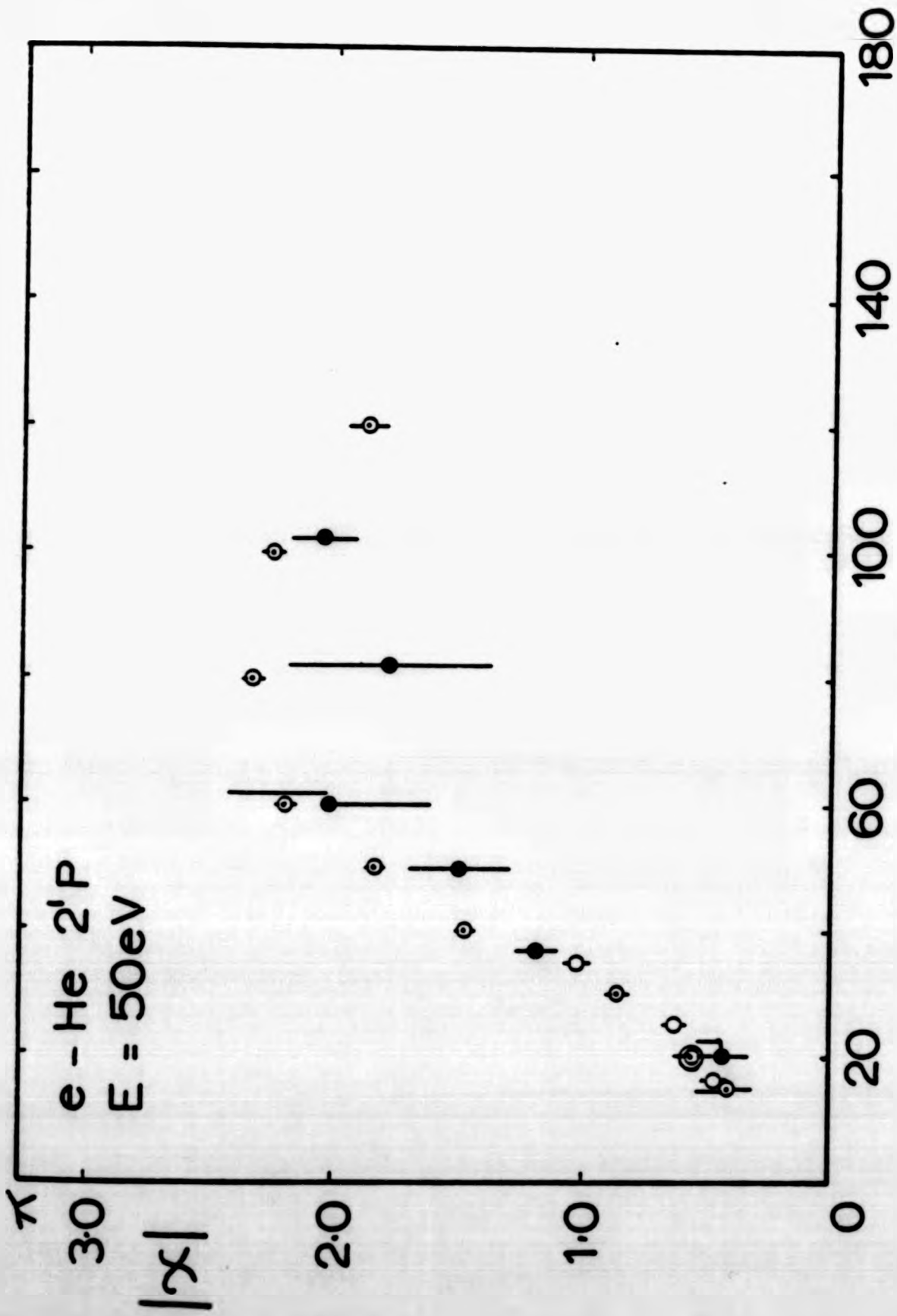


Figure (5-10):  $\lambda$  for the  $3^1P$  state of helium as a function of the electron scattering angle for 50 eV;  $\bullet$  present angular correlation results;  $\Delta$  present linear polarization correlation results for small scattering angles.  $\circ$  Eminyan et al. (1975) (Angular correlation results). — Theoretical calculation of Meneses et al. (1980). - · - Theoretical calculation of Scott et al. (1976).



Electron Scattering Angle (Deg)

Figure (5-11): Variation of  $|\chi|$  for the  $2^1P$  state as a function of the electron scattering angle for 50 eV. ● present data; ○ Eminyay et al. at 50 eV, ⊙ MacAdams et al. at 51.2 eV.

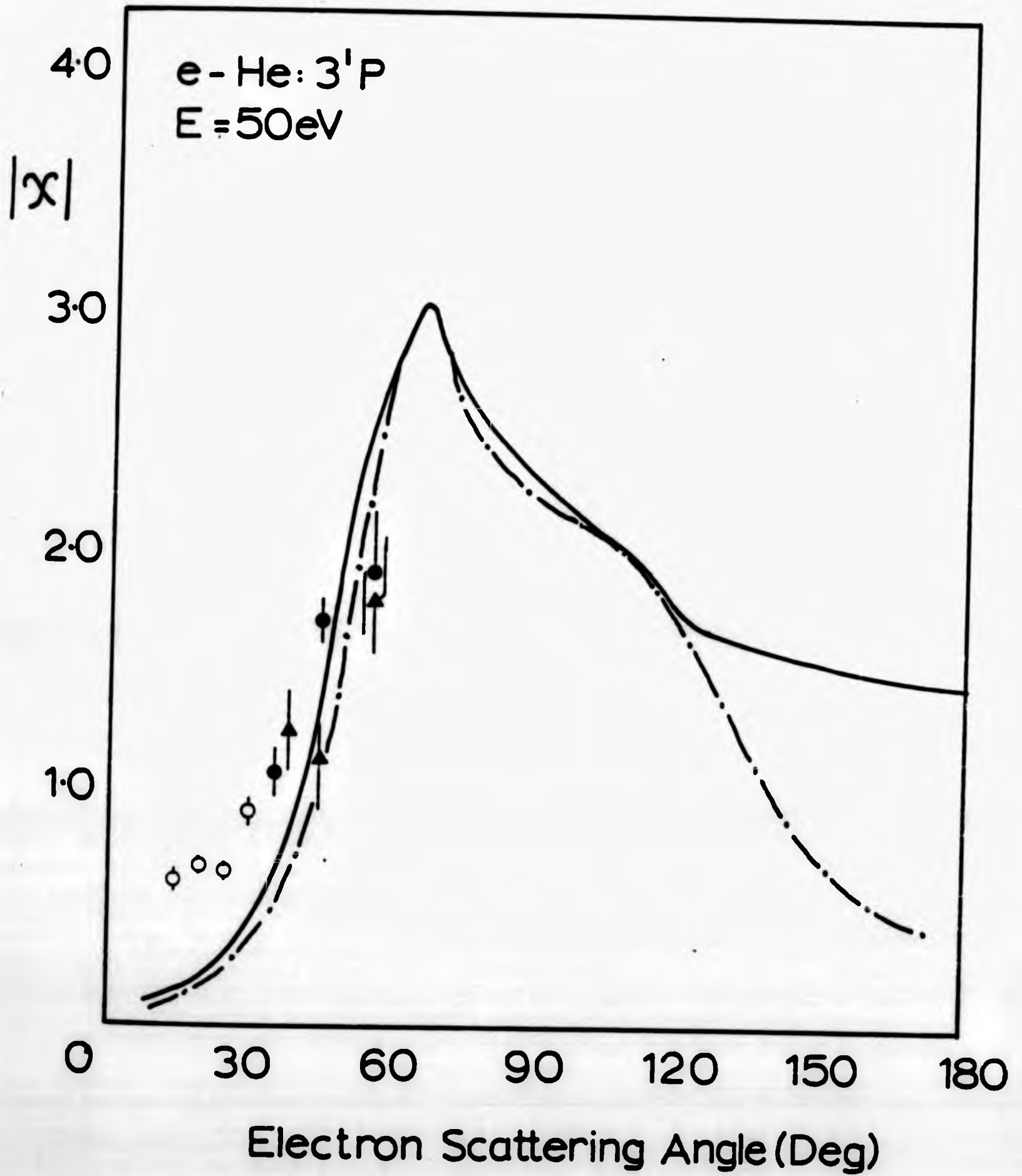


Figure (5-12): Variation of  $|\chi|$  for the  $3^1P$  state as a function of the electron scattering angle for 50 eV. ● present values (Angular correlation measurements). ▲ present data (linear polarization measurements), ○ Eminyay et al. (1975), — Meneses et al. (1980); - · - · - Scott et al. (1976).

measured values are listed in tables (5-2 to 5-5).

Figures (5-13 and 5-14) show the results of the linear polarization measurements at incident electron energies 50, 80, 120 and 160 eV.

The only other measurements are carried out for 80 eV at small electron scattering angles (Standage and Kleinpoppen, 1976 and Beyer et al. 1984). These results are shown in figures (5-13 and 5-14) along with the present values.

### 5.2.2. Circular Polarization Results

The circular polarization measurements were carried out by inserting the quarter wave plate in the optical system with its slow axis parallel to the electron beam direction. The corresponding values of the Stokes parameter  $\eta_2$  are determined by using equation (5.35) and the values for all measured energies are listed in tables (5-2 to 5-5) and shown in figure (5-15).

The results of  $\eta_2$  at 80 eV are compared with experimental results at small scattering angles by Standage and Kleinpoppen (1976) and Beyer et al. (1984).

The curves in figure (5-15) show that the circular polarization approaches the maximum value for all measured energies at the electron scattering angle of  $45^\circ \pm 5^\circ$ . The figure also confirms that there is a sign change of the circular polarization for all measured energies and thus clarifies this point which had been much disputed over the last few years (Madison et al. (1983), and Andersen et al. (1984 and 1985)).

The circular polarization is linked to the orientation parameter  $O_{1-}^{col}$ , and the orbital angular momentum  $\langle L_y \rangle$  by  $\eta_2 = -2O_{1-}^{col} = \langle L_y \rangle$ , where  $\langle L_y \rangle$  is the only non-zero component of orbital angular momentum transferred to the atom during the collision. The values of the

Table (5-2), E = 50 eV

$\theta_e^\circ$	$\eta_1 = \frac{I(45) - I(135)}{I(45) + I(135)}$	$\eta_3 = \frac{I(0) - I(90)}{I(0) + I(90)}$	$\eta_2 = \frac{I_{RHC} - I_{LHC}}{I_{RHC} + I_{LHC}}$
38	-0.249 ± 0.123	0.429 ± 0.369	-0.444 ± 0.139
45	-0.405 ± 0.135	0.452 ± 0.128	-0.527 ± 0.163
55	0.189 ± 0.252	0.608 ± 0.173	-0.090 ± 0.280
65	0.432 ± 0.436	0.733 ± 0.363	-0.112 ± 0.278
75	0.264 ± 0.273	0.555 ± 0.210	-0.054 ± 0.228
85	0.328 ± 0.464	0.474 ± 0.687	0.182 ± 0.280
95			0.104 ± 0.426
105	0.560 ± 0.289	0.396 ± 0.160	0.567 ± 0.172

Measured Stokes parameters for the  $3^1P$  state in helium for electron incident energy 50 eV.

Table (5-3), E = 80 eV

$\theta_e$	$\eta_1 = \frac{I(45) - I(135)}{I(45) + I(135)}$	$\eta_3 = \frac{I(0) - I(90)}{I(0) + I(90)}$	$\eta_2 = \frac{I_{RHC} - I_{LHC}}{I_{RHC} + I_{LHC}}$
27.5		-0.462 ± 0.079	-0.465 ± 0.066
35	-0.713 ± 0.572	-0.343 ± 0.112	-0.572 ± 0.106
40	-0.425 ± 0.407	-0.045 ± 0.140	-0.759 ± 0.083
50	0.276 ± 0.265	0.533 ± 0.156	-0.558 ± 0.112
60	0.218 ± 0.256	0.180 ± 0.365	-0.298 ± 0.108
70	0.231 ± 0.345	0.916 ± 0.418	-0.169 ± 0.127
80	0.493 ± 0.222	0.716 ± 0.246	0.282 ± 0.142
90	0.823 ± 0.411	0.499 ± 0.286	0.559 ± 0.211

Measured Stokes parameter for the  $3^1P$  state in helium, for electron incidence energy 80 eV.

Table (5-4), E = 120 eV

$\theta_e$	$\eta_1 = \frac{I(45) - I(135)}{I(45) + I(135)}$	$\eta_3 = \frac{I(0) - I(90)}{I(0) + I(90)}$	$\eta_2 = \frac{I_{RHC} - I_{LHC}}{I_{RHC} + I_{LHC}}$
35	$-0.325 \pm 0.168$	$0.090 \pm 0.112$	$-0.381 \pm 0.251$
40	$-0.259 \pm 0.112$	$0.189 \pm 0.096$	$-0.496 \pm 0.106$
50	$0.005 \pm 0.192$	$0.717 \pm 0.108$	$-0.374 \pm 0.182$
60	$0.741 \pm 0.397$	$0.780 \pm 0.220$	$0.242 \pm 0.216$
70	$0.538 \pm 0.467$	$0.891 \pm 0.216$	$0.308 \pm 0.248$
80	$0.684 \pm 0.514$	$0.501 \pm 0.286$	$0.714 \pm 0.514$
90	$0.230 \pm 0.367$	$-0.274 \pm 0.443$	$0.882 \pm 0.485$

Measured Stokes parameters for the  $3^1P$  state in helium, for the electron incident energy 120 eV.

Table (5-5), E = 160 eV

$\theta_e$	$\eta_1 = \frac{I(45) - I(135)}{I(45) + I(135)}$	$\eta_3 = \frac{I(0) - I(90)}{I(0) + I(90)}$	$\eta_2 = \frac{I_{RHC} - I_{LHC}}{I_{RHC} + I_{LHC}}$
28	$0.441 \pm 0.217$	$0.293 \pm 0.143$	$-0.451 \pm 0.163$
35	$0.290 \pm 0.223$	$0.320 \pm 0.210$	$-0.464 \pm 0.342$
40	$0.156 \pm 0.147$	$0.597 \pm 0.203$	$-0.746 \pm 0.486$
45	$0.138 \pm 0.288$	$0.696 \pm 0.422$	$0.287 \pm 0.629$
50	$0.219 \pm 0.348$	$0.576 \pm 0.361$	$0.292 \pm 0.244$
55	$0.598 \pm 0.406$	$0.581 \pm 0.418$	$0.643 \pm 0.307$
60	$0.739 \pm 0.212$	$0.582 \pm 0.274$	$0.807 \pm 0.438$
70			$0.598 \pm 0.230$
80			$0.444 \pm 0.294$
90			$0.715 \pm 0.365$
100			$0.537 \pm 0.365$
108			$0.311 \pm 0.251$

Measured Stokes parameters for the  $3^1P$  state in helium, for electron incident energy 160 eV.

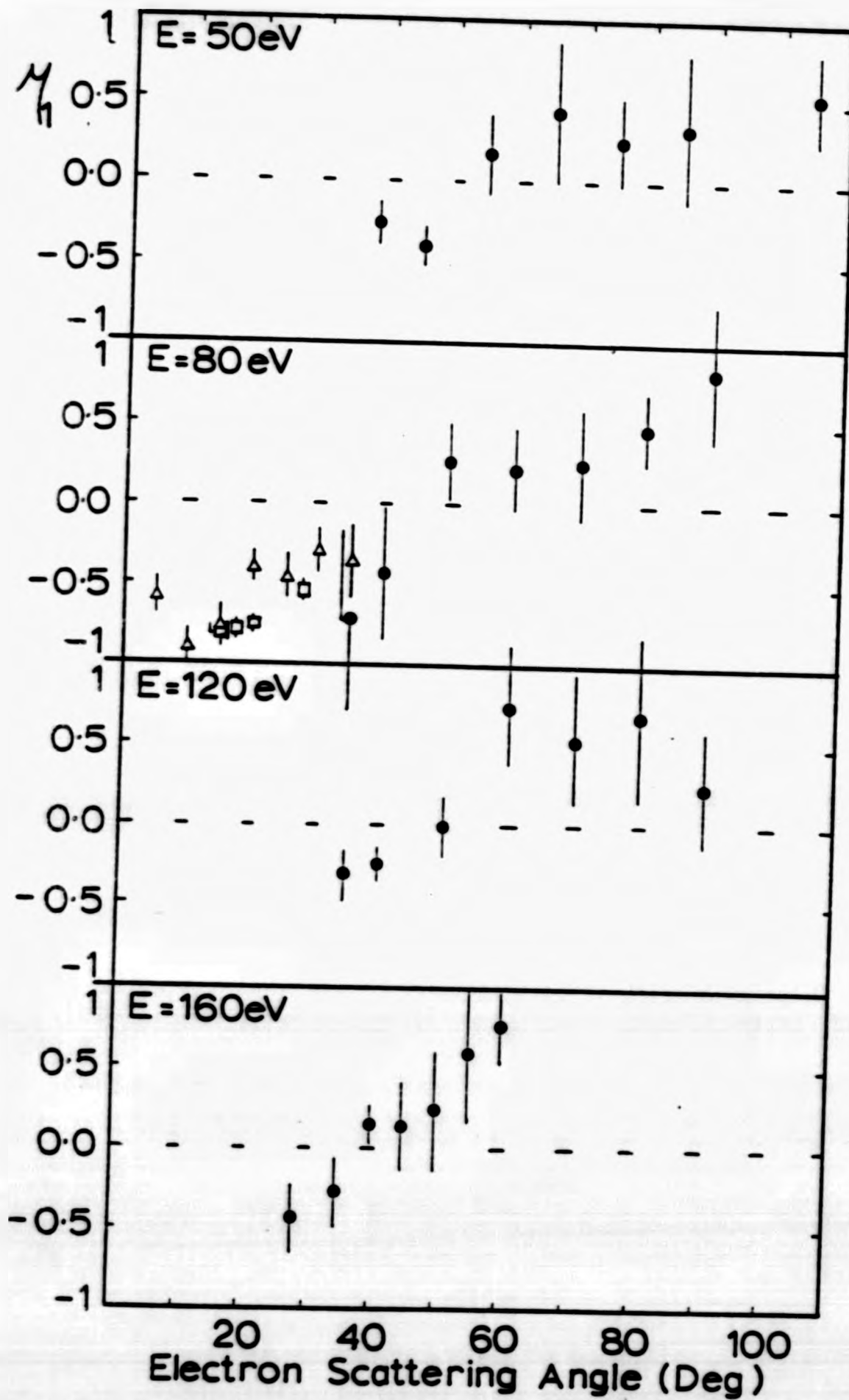


Figure (5-13): The linear polarization Stokes parameter  $\eta_1$  as a function of the electron scattering angle for the measured impact energies. The present values ● are compared with previous linear polarization measurements at 80 eV by Standage and Kleinpoppen (1976) □ and Beyer (1984) △ .

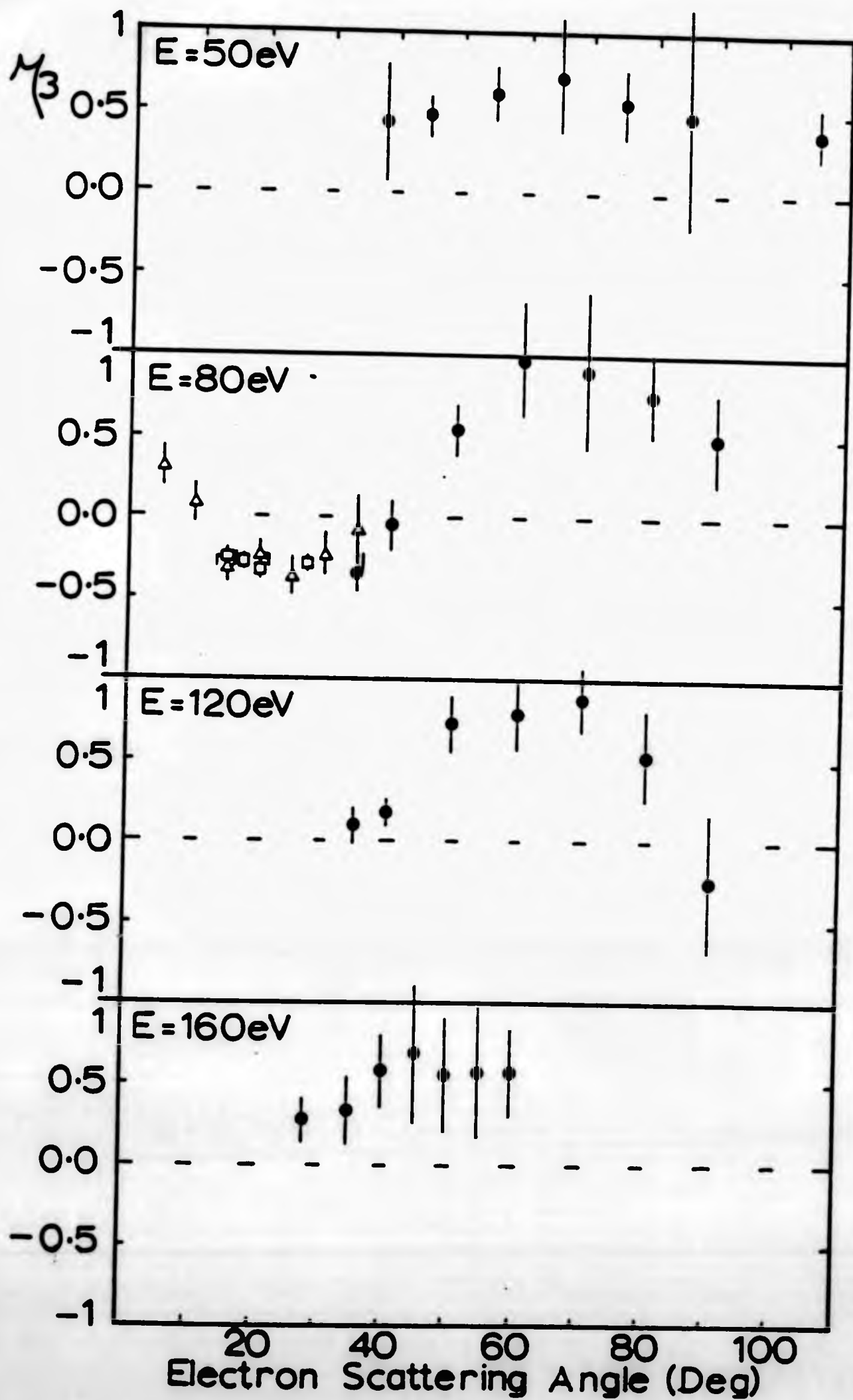


Figure (5-14): Stokes parameter  $\eta_3$ , as a function of the electron scattering angle for the measured impact energies. The present values ●, are compared with previous values at 80 eV by Standage and Kleinpoppen (1976) □, and Beyer (1984) Δ.

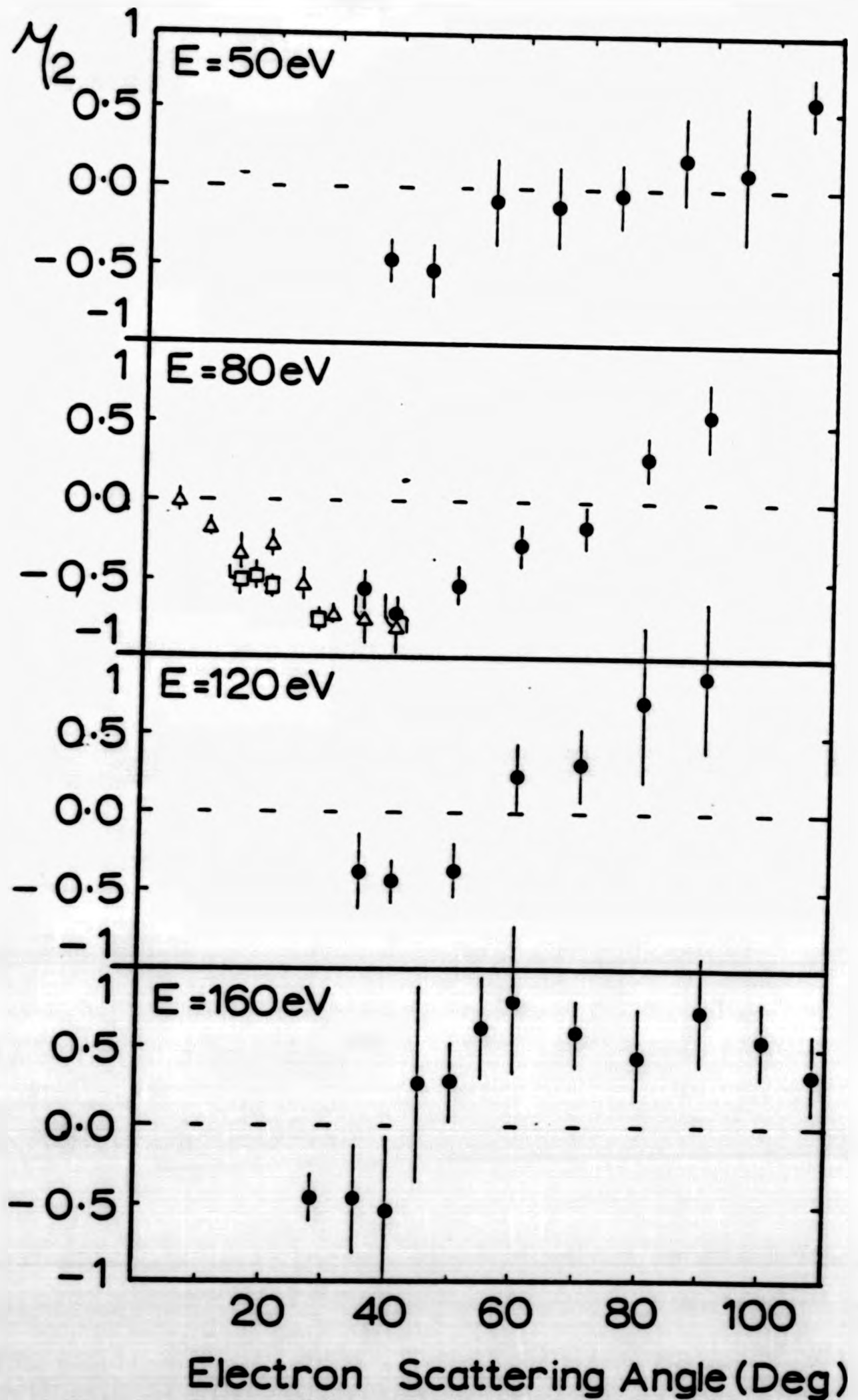


Figure (5-15): The circular polarization Stokes parameter  $\eta_2$  as a function of the electron scattering angle for the measured impact energies. The present values  $\bullet$  are compared with previous circular polarization results  $\eta_2$  at 80 eV by Standage and Kleinpoppen (1976)  $\square$ , and Beyer (1984)  $\Delta$ .

scattering angle at which the present results show the sign change of  $\langle L_y \rangle$  are listed in table (5-6) and drawn in figure (5-16) as a function of the incident electron energy. The measurements show that the scattering angle at which the sign changes decreases with increasing energy in line with the expectation from theoretical calculations (Madison, 1983). Furthermore, within the measured energy range there appears to be a linear relation between the angle of the sign change of  $\langle L_y \rangle$  and the incident energy.

The question of the possible sign change of the angular momentum  $\langle L_y \rangle$  had been discussed for several years and a number of related measurements were carried out by other groups concurrently with this work. Williams (1983) confirmed a sign change of the Stokes parameter  $\eta_2$  somewhere between the two electron scattering angles  $10^\circ$  and  $90^\circ$  for the  $2^1P$  state of helium at an energy of 81.2 eV. Again on the  $2^1P$  state of helium Beijers et al. (1984) concluded from angular correlation measurements at 80 eV that the sign of the angular momentum changes at  $\theta_e = 65^\circ$ . They speculated that there might be no sign change for the  $3^1P$  state (and did not find any). Recently Khakoo et al. (1985) using the polarization correlation method on the  $2^1P$  state of helium, confirmed the sign change for incident electron energies of 50, 60 and 80 eV.

The behaviour of the angular momentum  $\langle L_y \rangle$  has been linked to the following model. At  $\theta_e = 0$  the Stokes parameter  $\eta_2$  is restricted to zero by angular momentum conservation rules and only the  $M_L = 0$  magnetic sublevel is excited. At  $\theta_e$  around  $45^\circ$   $\eta_2$  nearly equals  $-1$  and this there is a predominance of  $M_L = +1$  excitation. At this angle, the projection of the charge cloud of the excited P state onto the scattering plane is almost circular and rotates counter-clockwise (Anderson et al., 1984).

Table (5-6): Angle of the sign change of  $\langle L_y \rangle$  as a function of incident energy.

Incident Energy	Range of Scattering Angles	Angle of $\langle L \rangle$ - Change
50 eV	35 ————— 105	97 ± 5
80 eV	27.5 ————— 90	75 ± 5
120 eV	45 ————— 90	65 ± 5
160 eV	28 ————— 60	47 ± 5

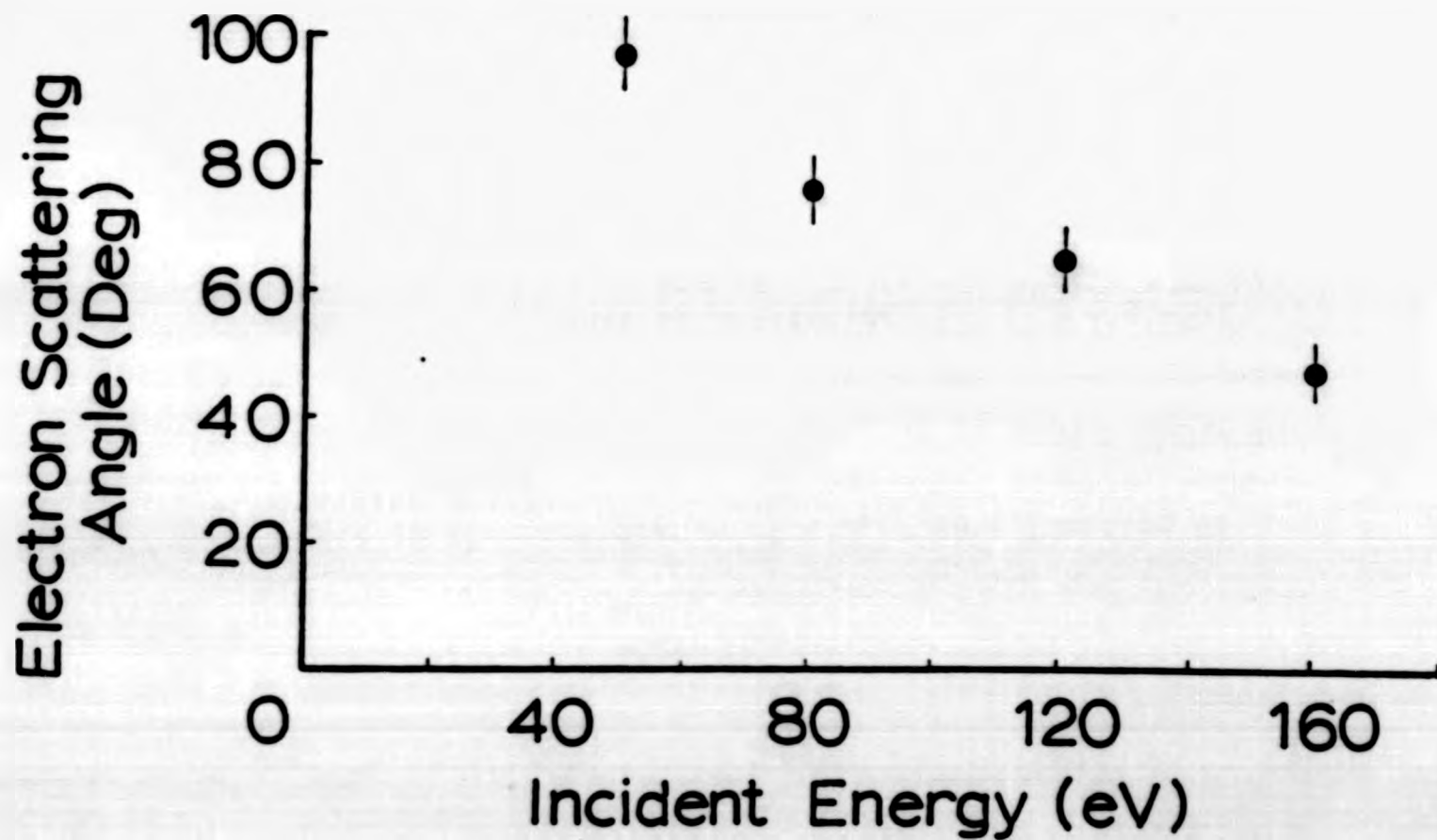


Figure (5-16): Variation of angle of the sign change of  $\langle L_y \rangle$  as a function of the incident energy.

As  $\eta_2$  becomes zero at intermediate scattering angles, the charge cloud forms a dumb-bell shape, becoming close to circular again at larger scattering angles, but now rotating clockwise. Madison (1985) has pointed out that this change in the dynamic rotation of the  $n^1P$  state is due to a manifestation of the change in the relative strength of the attractive scattering potential seen by the electron and not due to a competition between attractive and repulsive interactions as had been suggested earlier by Steph and Golden (1980).

Furthermore, the complete analysis of the electron photon polarization measurements in figure (5-17) shows the magnitude of the vector polarization (equation 2-28) for all measured energies as a function of the electron scattering angle.

Since the excitation of the  $n^1P$  states is coherent we expect the light to be completely polarized with  $P = [\eta_1^2 + \eta_2^2 + \eta_3^2]^{\frac{1}{2}} = 1$ . Blum (1981) points out that this is not in general true, even if the excitation is completely coherent. In general  $|P| = 1$  only for a transition between two pure states such as  $n^1P - 1^1S$ .

Apart from the values for the incident energy 50 eV, the results in figure (5-17) show that the degree of polarization is equal to 1. At 50 eV the values of  $|P|$  appear to be consistently low but still overlap with the value of 1 within the error bar (one standard deviation).

### 5.2.3. The Excitation Parameters

The excitation parameters  $\lambda$  and  $\chi$  are derived from the measured Stokes parameters using equations (2.33 - 2.35).

The measured variation of  $\lambda$  with the scattering angle for the  $3^1P$  state of helium is presented in figure (5-18) and listed in table (5-7a-d) for all measured energies. The curves for

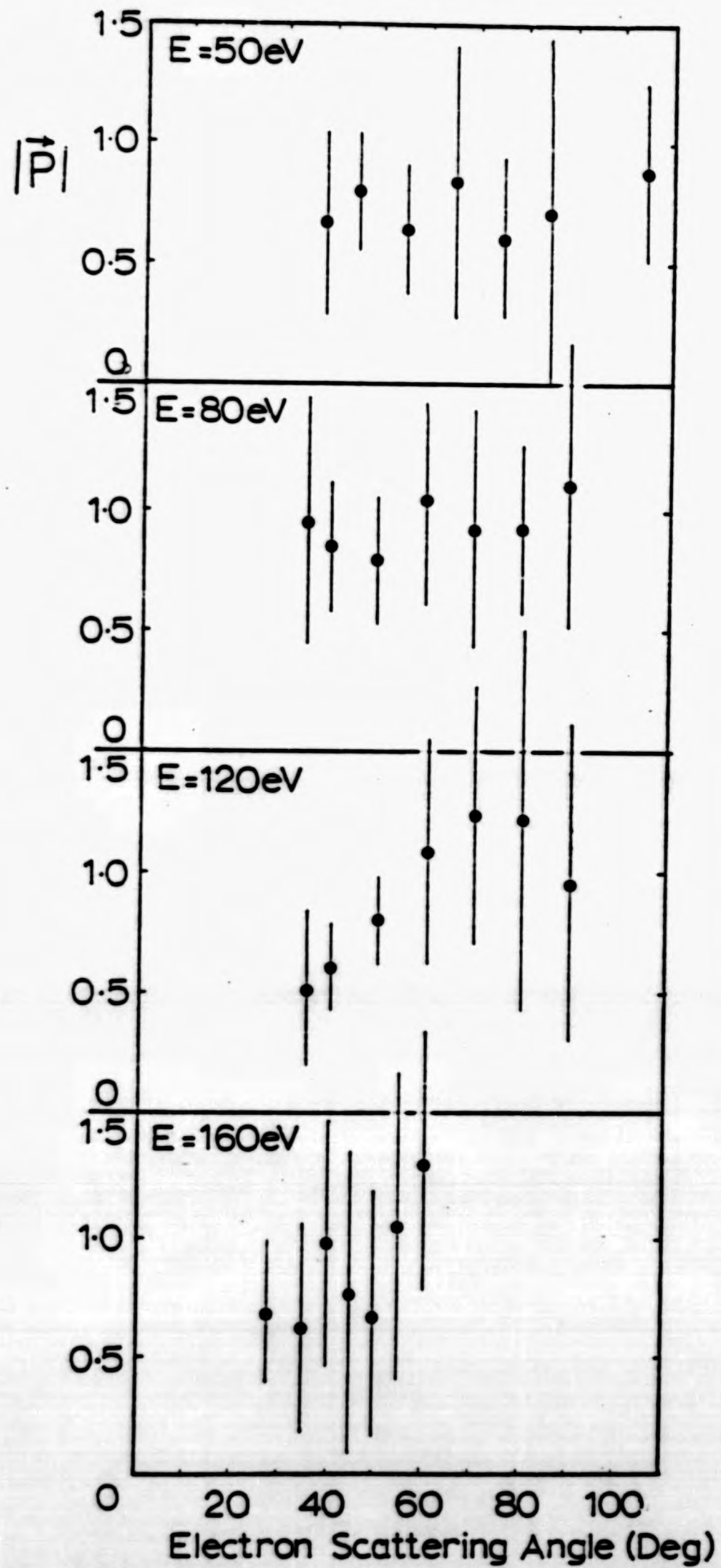


Figure (5-17): Magnitude of the vector polarization  $|\vec{P}| = (\eta_1^2 + \eta_2^2 + \eta_3^2)^{1/2}$  for the He  $3^1P - 2^1S$  (501.6 Å) transition, as a function of the electron scattering angle for the measured energies.

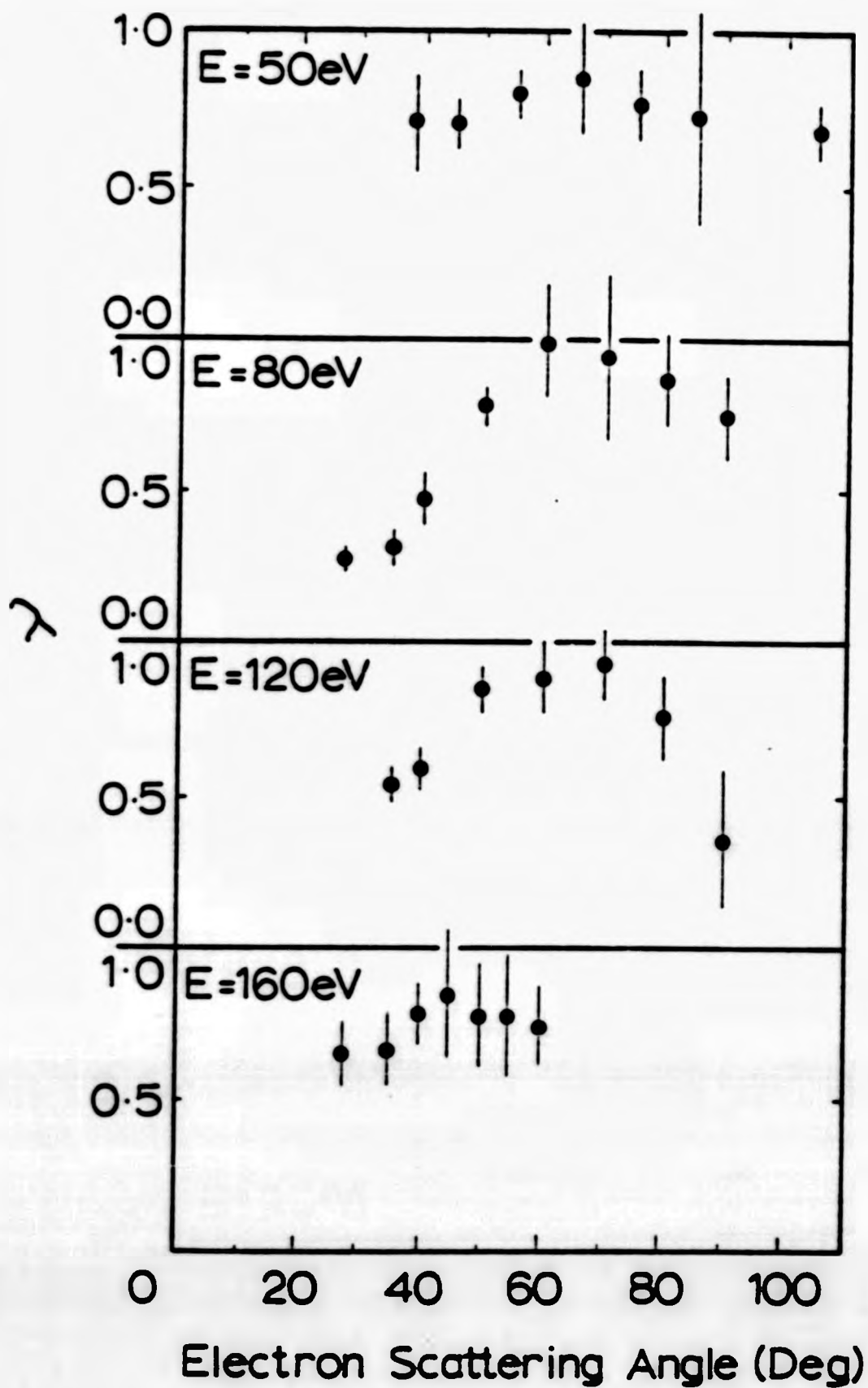


Figure (5-18): Parameter  $\lambda = \frac{\sigma_0}{\sigma}$  for the excitation of the  $3^1P$  state of helium as a function of the electron scattering angle for the different values incident energy.

Table (5-7a)

$\theta_e$	$\lambda(E = 50 \text{ eV})$
38	$0.714 \pm 0.18$
45	$0.726 \pm 0.061$
55	$0.804 \pm 0.080$
65	$0.866 \pm 0.181$
75	$0.777 \pm 0.108$
85	$0.737 \pm 0.340$
105	$0.698 \pm 0.080$

Table (5-7b)

$\theta_e$	$\lambda(E = 80 \text{ eV})$
27.5	$0.269 \pm 0.039$
35	$0.328 \pm 0.056$
40	$0.477 \pm 0.070$
50	$0.766 \pm 0.078$
60	$0.994 \pm 0.182$
70	$0.958 \pm 0.209$
80	$0.858 \pm 0.123$
90	$0.749 \pm 0.143$

Table (5-7c)

$\theta_e$	$\lambda(E = 120 \text{ eV})$
35	$0.545 \pm 0.056$
40	$0.594 \pm 0.040$
50	$0.858 \pm 0.054$
60	$0.896 \pm 0.110$
70	$0.945 \pm 0.108$
80	$0.750 \pm 0.145$
90	$0.431 \pm 0.221$

Table (5-7d)

$\theta_e$	$\lambda(E = 160 \text{ eV})$
28	$0.646 \pm 0.071$
35	$0.660 \pm 0.105$
40	$0.798 \pm 0.101$
45	$0.848 \pm 0.211$
50	$0.788 \pm 0.180$
55	$0.790 \pm 0.209$
60	$0.791 \pm 0.137$

Table (7a, b, c and d): Values of the excitation parameter  $\lambda = \frac{\sigma_0}{\sigma}$  derived from the polarization correlation experiment as a function of electron scattering angle for the measured energies.

the energies 50 and 160 eV show a slow variation of  $\lambda$  with scattering angles, whereas those for 80 and 120 eV exhibit a comparatively sharp maximum at scattering angles of about  $60^\circ$  and  $70^\circ$  respectively.

Figure (5-19) shows  $\lambda$  as a function of the scattering angle at an incident electron energy of 50 eV together with results of previous angular correlation measurements by Crowe et al. (1981) at an incident electron energy of 45.6 eV and by Eminyan et al. (1975) at 50 eV. The measured values are also compared with calculations where values of  $\lambda$  have been reported over the complete angular range from  $0^\circ$  up to  $180^\circ$  (Meneses et al., 1980 and Flannery et al., 1975).

Figure (5-20) shows the variation of  $\lambda$  with  $\theta_e$  at 80 eV together with the experimental values derived from polarization correlation measurements at small scattering angles by Standage and Kleinpoppen (1976), and the angular correlation measurements by Crowe et al. (1981) at 75.6 eV and by MacAdams et al. (1982) at 81.2 eV for large scattering angles along with the theoretical calculation of Meneses et al. (1980) and Flannery et al. (1975). The present values agree quite well with the theoretical calculation and the previous experimental points.

No other experimental or theoretical work has been reported for incident energies of 120 and 160 eV to our knowledge.

Once  $\lambda$  has been determined the excitation parameter  $\chi$  is derived from the linear and circular polarization measurements ( $\eta_1$  and  $\eta_2$  respectively) using equations (2.34 and 2.35). Within the symmetry of the cosine and sine functions each equation gives two possible values of  $\chi$  within any range of  $2\pi$ . All four values are listed in tables (5-8 to 5-11) but only two form a consistent pair as shown in figures (5-21 to 5-24). Equation (4.4) and the two consistent values obtained from the linear and circular measurements of  $\chi$  (marked values in the above tables) have been used to calculate the average

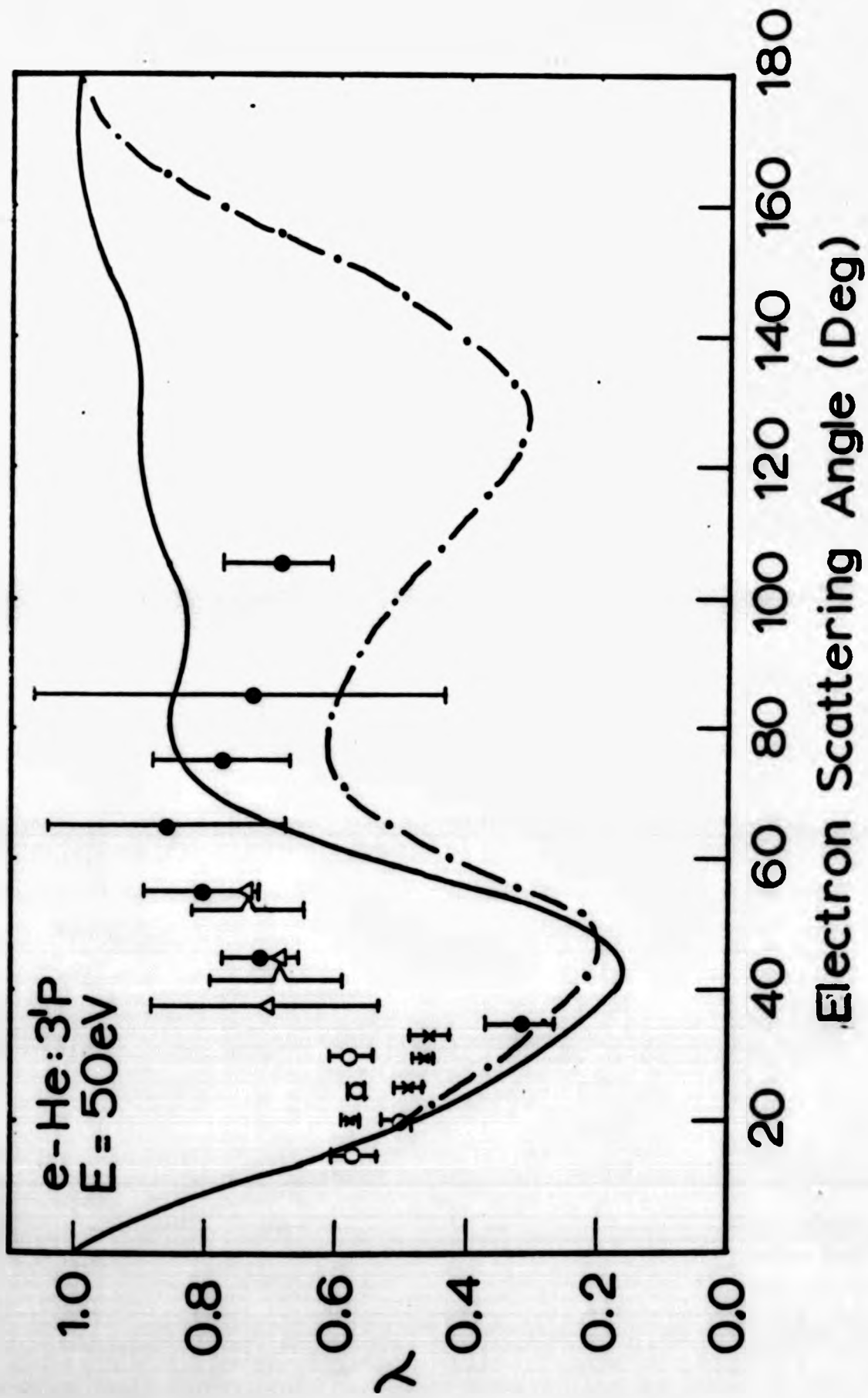
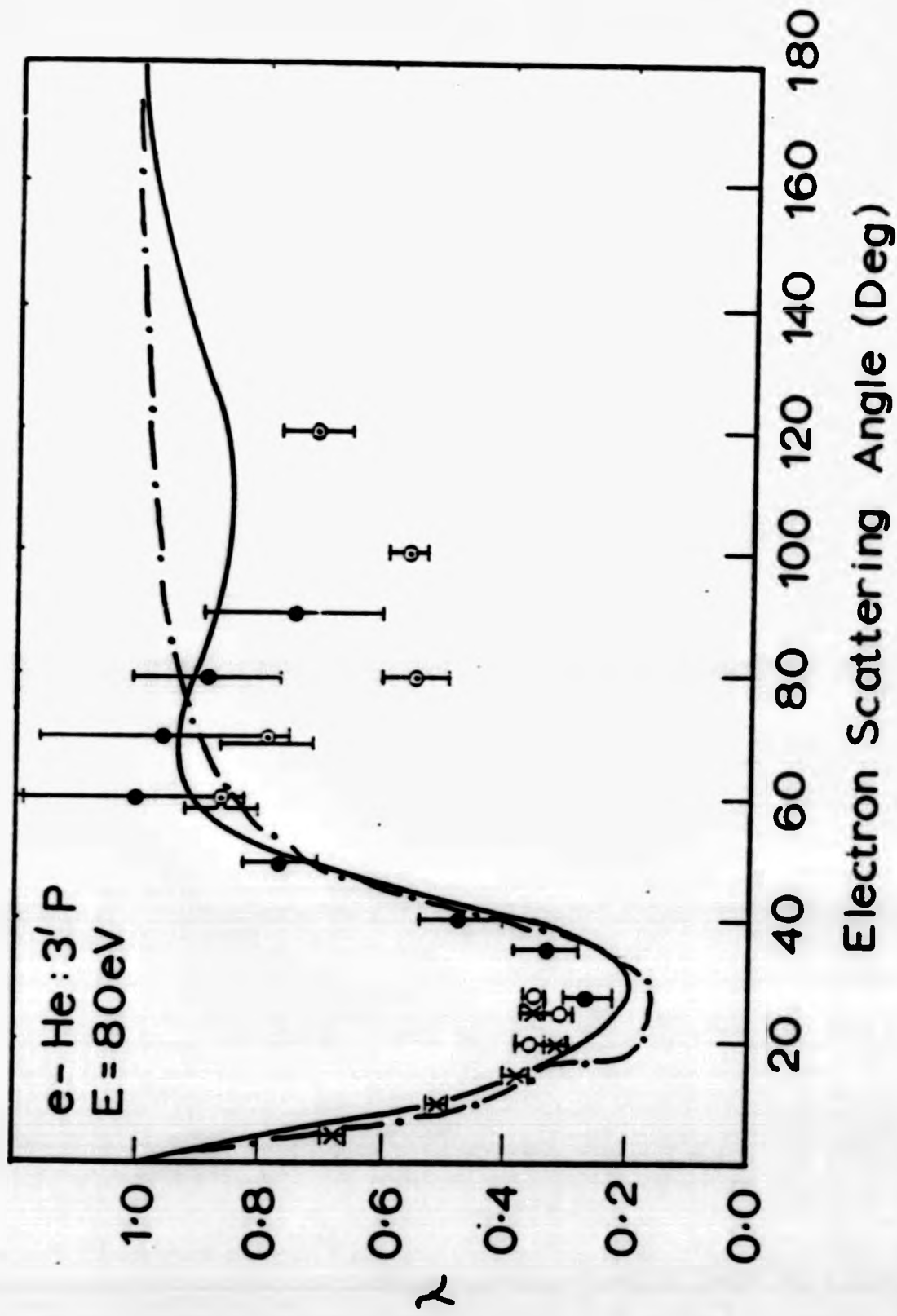


Figure 5-19):  $\lambda$  for the  $3^1P$  state of helium derived from the polarization correlation experiment as a function of the electron scattering angle. Incident energy 50 eV. The present values  $\bullet$  are compared with present angular correlation values  $\Delta$  and with previous angular correlation results of Emynan et al. (1975)  $\circ$ , and Crowe et al. (1980)  $\times$  at incident energy of 45.6 eV, as well as with theoretical calculation of Meneses et al. (1980) —, and Scott et al. (1976) . . . .



Figure(5-20):  $\lambda$  for the 3'P state of helium derived from the polarization correlation experiment as a function of the electron scattering angle for the incident energy of 80 eV. The present results  $\bullet$  are compared with previous values of Standage et al. (1976)  $\circ$  and with angular correlation results of Crowe et al. (1981)  $\times$  at energy of 75.6 eV. and MacAdam (1982)  $\odot$  at energy of 81.2 eV, as well as with the theoretical calculations of Meneses et al. (1980) —, and Flannery et al. (1975). - . - . - .

E = 50 eV

Table (5-8)

$\theta_e$ Deg.	The possibilities of $\chi$ derived from circular polarization Stokes parameter $\eta_2$		The possibilities of $\chi$ derived from the linear polarization Stokes parameter $\eta_1$		The average value of $\chi$ calculated from the marked values in columns 1, 2, 3 and 4
	1	2	3	4	
38	-0.514 ± 0.184	-2.627 ± 0.184	-1.627 ± 0.14 <sup>x</sup>	-1.291 ± 0.144	-0.995 ± 0.113
45	-0.635 ± 0.228 <sup>x</sup>	-2.506 ± 0.228	-1.099 ± 0.170 <sup>x</sup>	-5.184 ± 0.170 <sup>x</sup>	-0.933 ± 0.136
55	-0.113 ± 0.355 <sup>x</sup>	-3.028 ± 0.355	-1.811 ± 0.301 <sup>x</sup>	-4.472 ± 0.301	-2,319 ± 0.229
65	-0.165 ± 0.516 <sup>x</sup>	-2.976 ± 0.416	-2.257 ± 0.860 <sup>x</sup>	-4.026 ± 0.860	-2.839 ± 0.374
75	-0.064 ± 0.274	-3.077 ± 0.274 <sup>x</sup>	-1.893 ± 0.347	-4.390 ± 0.347 <sup>x</sup>	-3.581 ± 0.215
85	-3.348 ± 0.328 <sup>x</sup>	-6.076 ± 0.328	-1.952 ± 0.574	-4.331 ± 0.574 <sup>x</sup>	-3.590 ± 0.284
105	-3.805 ± 0.240 <sup>x</sup>	-5.619 ± 0.240	-2.226 ± 0.574	-4.057 ± 0.574 <sup>x</sup>	-3.842 ± 0.221

Tables (5-8 to 5-11):

The possible values of the phase difference  $\chi$  between  $a_1$  and  $a_2$  for different electron scattering angles and impact energies derived from the circular polarization. Stokes parameter  $\eta_2$  (column 1 and 2) and the linear polarization Stokes parameter  $\eta_1$  (column 3 and 4). The average values of  $\chi$  in column 5 are calculated from the consistent pair of circular and linear results. (Marked by stars in columns 1-4).



E = 120 eV  
Table (5-10)

No	$\theta_e$	The possibilities of $\chi$ derived from circular polarization Stokes parameter $\eta_2$		The possibilities of $\chi$ derived from the linear polarization Stokes parameter $\eta_1$		The average value of $\chi$
		1	2	3	4	
1-	35	$-0.392 \pm 0.274^x$	$-2.749 \pm 0.274$	$-1.258 \pm 0.179^x$	$-5.025 \pm 0.179$	$-0.998 \pm 0.149$
2-	40	$-0.530 \pm 0.125^x$	$-2.611 \pm 0.125$	$-1.303 \pm 0.118^x$	$-4.980 \pm 0.118$	$-0.938 \pm 0.085$
3-	50	$-0.565 \pm 0.324^x$	$-2.576 \pm 0.324^x$	$-1.563 \pm 0.274^x$	$-4.720 \pm 0.274$	$-1.985 \pm 0.209$
4-	60	$-3.538 \pm 0.416^x$	$-5.886 \pm 0.416$	$-2.679 \pm 1.150$	$-3.604 \pm 1.150^x$	$-3.545 \pm 0.391$
5-	70	$-3.889 \pm 1.112^x$	$-5.540 \pm 1.112$	$-2.387 \pm 0.965$	$-3.896 \pm 0.965^x$	$-3.892 \pm 0.728$
6-	80	$-4.110 \pm 0.956^x$	$-5.314 \pm 0.956$	$-2.481 \pm 0.873$	$-3.802 \pm 0.873^x$	$-3.942 \pm 0.644$
7-	90	$-4.303 \pm 1.276^x$	$-5.121 \pm 1.276$	$-1.812 \pm 0.245$	$-4.471 \pm 0.245^x$	$-4.465 \pm 0.240$

E = 160 eV  
Table (5-11)

No	$\theta_e$	The possibilities of $\chi$ derived from circular polarization Stokes parameter $\eta_2$		The possibilities of $\chi$ derived from the linear polarization Stokes parameter $\eta_1$		The average value of $\chi$
		1	2	3	4	
1-	28	$-0.491 \pm 0.208^x$	$-2.650 \pm 0.208$	$-1.091 \pm 0.288^x$	$-5.192 \pm 0.288$	$-0.696 \pm 0.168$
2-	35	$-0.511 \pm 0.414^x$	$-2.630 \pm 0.414$	$-1.259 \pm 0.246^x$	$-5.024 \pm 0.246$	$-1.063 \pm 0.211$
3-	40	$-1.191 \pm 1.654^x$	$-1.950 \pm 1.654$	$-1.789 \pm 0.213^x$	$-4.494 \pm 0.213$	$1.791 \pm 0.201$
4-	45	$-3.551 \pm 0.863^x$	$-5.873 \pm 0.559$	$-1.763 \pm 0.410$	$-4.520 \pm 0.410^x$	$-4.341 \pm 0.370$
5-	50	$-3.413 \pm 0.559^x$	$-6.011 \pm 0.559$	$-1.841 \pm 0.447$	$-4.442 \pm 0.447^x$	$-4.040 \pm 0.349$
6-	55	$-4.049 \pm 0.657^x$	$-5.375 \pm 0.652$	$-2.394 \pm 0.759$	$-3.889 \pm 0.759^x$	$-4.232 \pm 0.496$
7-	60	$-4.587 \pm 2.509^x$	$-4.835 \pm 2.509$	$-2.711 \pm 0.672$	$-3.572 \pm 0.672^x$	$-3.639 \pm 0.649$

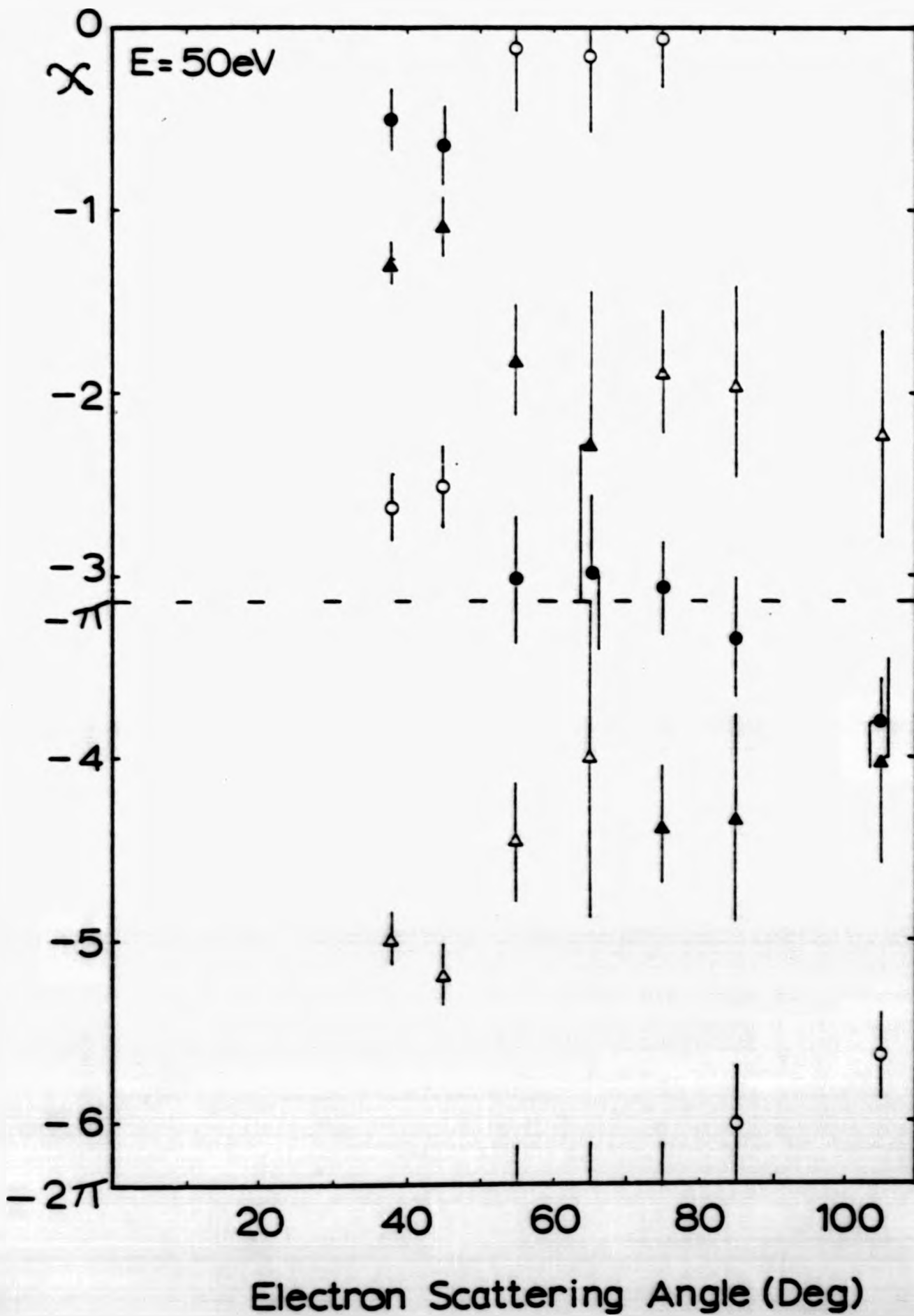


Figure (5-21): Possible values of  $\chi$  as a function of the electron scattering angle for the incident energy of 50 eV,  $\circ$  and  $\bullet$  derived from the circular polarization Stokes parameters  $\eta_2$ ,  $\Delta$  and  $\triangle$  from the linear polarization Stokes parameter  $\eta_1$ . The consistent pairs of  $\chi$  values adopted to calculate the final average are marked by full symbols ( $\bullet$  and  $\triangle$ ).

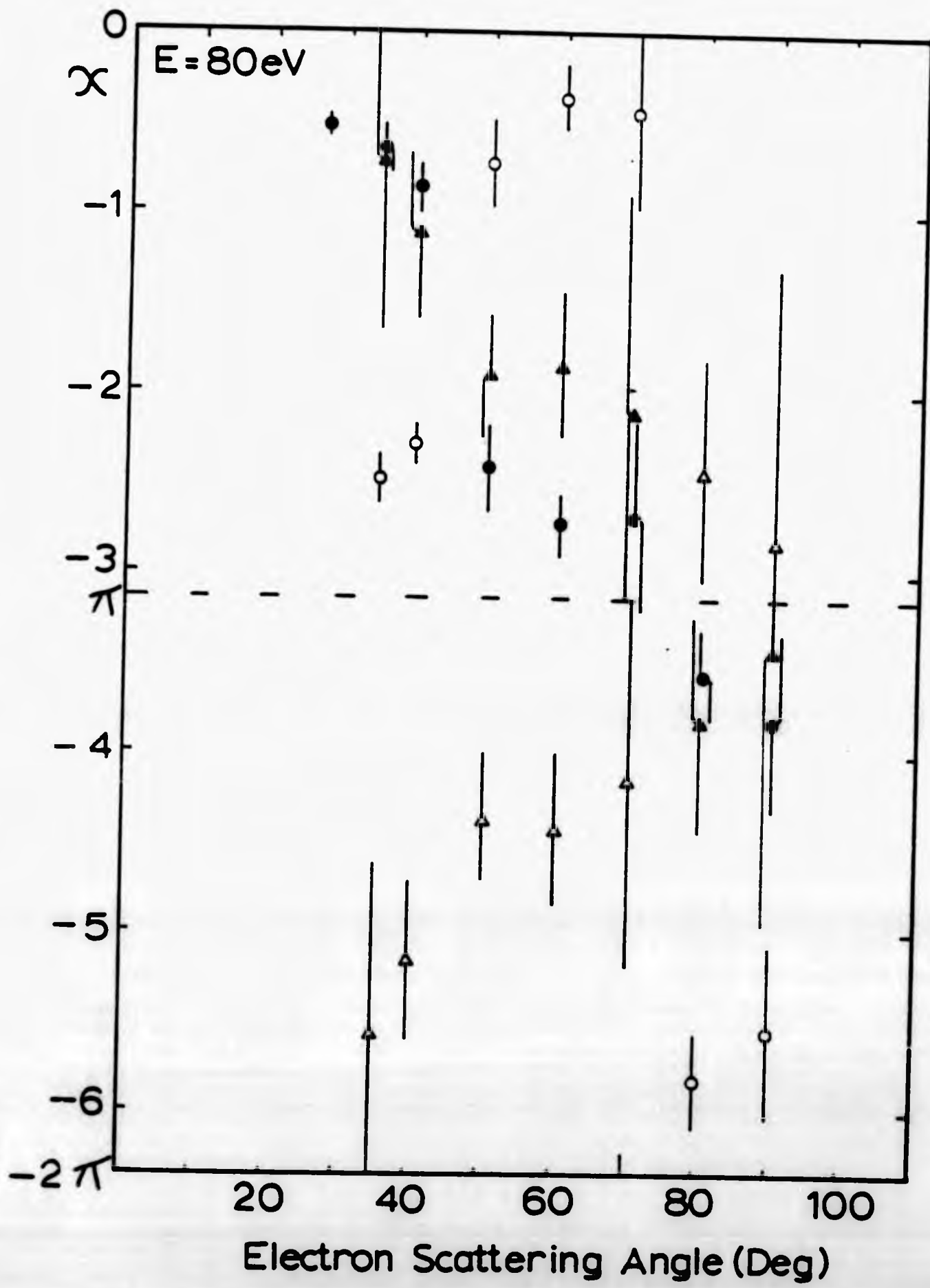


Figure (5-25): Possible values of  $\chi$  as a function of the electron scattering angle for the incident energy of 80 eV,  $\circ$  and  $\bullet$  derived from the circular polarization Stokes parameter  $\eta_2$ ,  $\triangle$  and  $\blacktriangle$  from the linear polarization Stokes parameter  $\eta_1$ . The consistent pairs of  $\chi$  values adopted to calculate the final average are marked by full symbols ( $\bullet$  and  $\blacktriangle$ ).

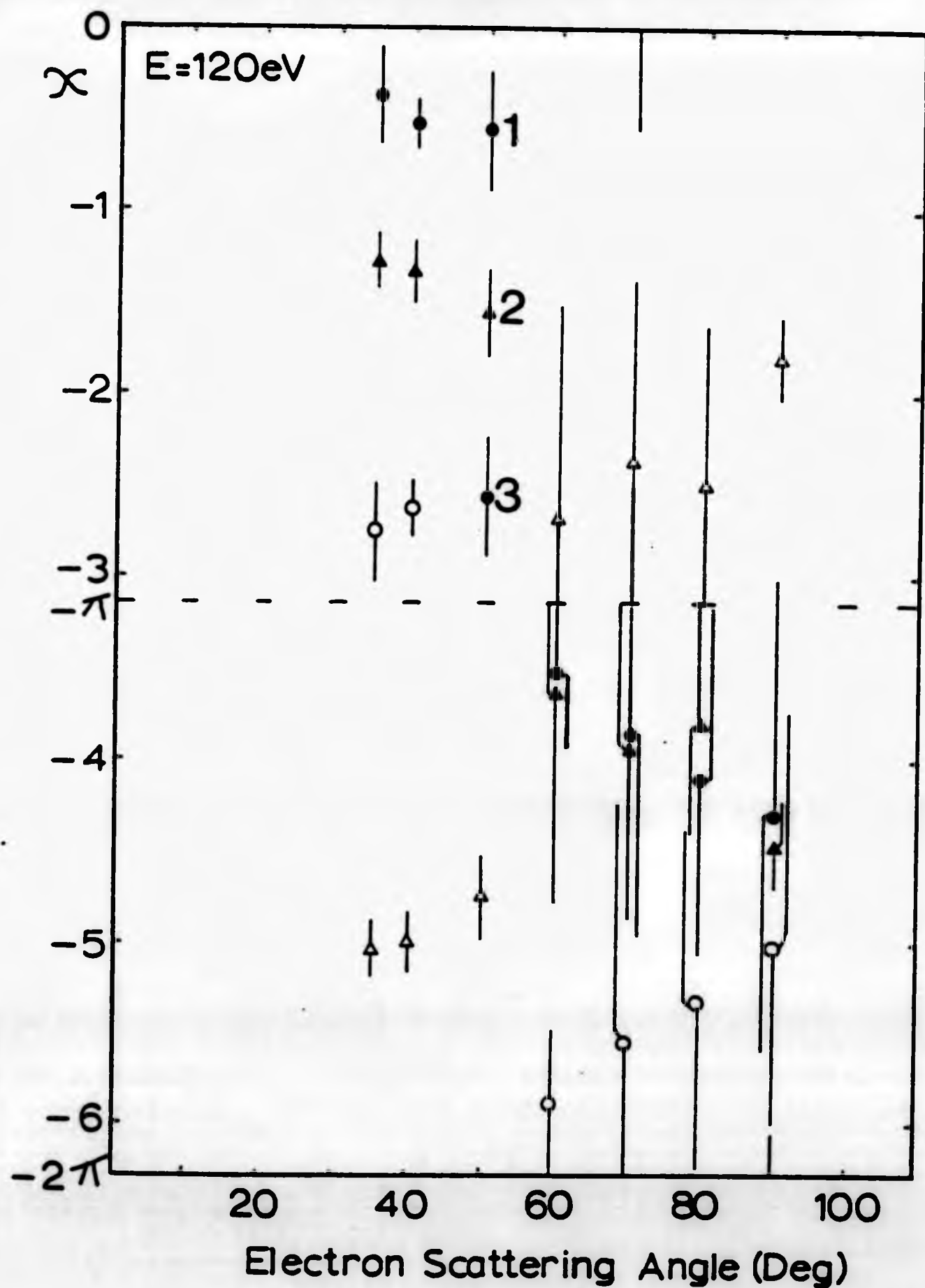


Figure (5-23): Possible values of  $\chi$  as a function of the electron scattering angle for the incident energy of 120 eV,  $\circ$  and  $\bullet$  derived from the circular polarization Stokes parameter  $\eta_2$ ,  $\Delta$  and  $\blacktriangle$  from the linear polarization Stokes parameter  $\eta_1$ . The consistent pairs of  $\chi$  values adopted to calculate final average are marked by full symbols ( $\bullet$  and  $\blacktriangle$ ). for  $\theta_e=50^\circ$ , the pairs (1,2) and (2,3) are equally "consistent". However, in line with the general trend of the  $\chi$  values the pair (2,3) has been chosen for the final value.

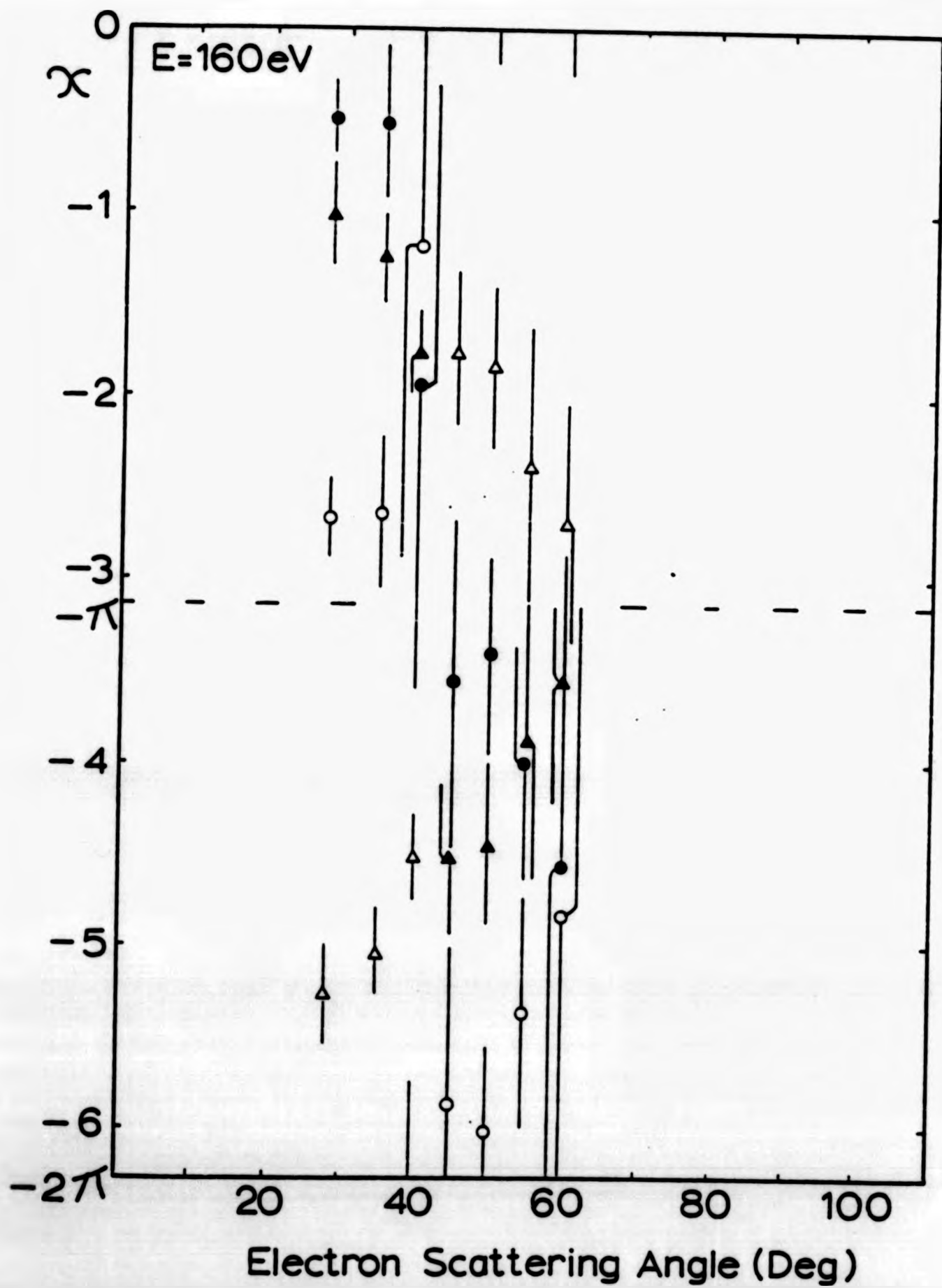


Figure (5-24): Possible values of  $\chi$  as a function of the electron scattering angle for the incident energy of 160 eV,  $\circ$  and  $\bullet$  derived from the circular polarization Stokes parameter  $\eta_2$ ,  $\triangle$  and  $\blacktriangle$  from the linear polarization Stokes parameter  $\eta_1$ . The consistent pairs of  $\chi$  values adopted to calculate the final average are marked by full symbols ( $\bullet$  and  $\blacktriangle$ ).

values of  $\chi$  as shown in column five of the tables (5-8 to 5-11) and in figure (5-25). The curves in figure 5-25 show the behaviour of  $\chi$  for different measured energies, and they show a sharp drop in the value of  $\chi$  between small and large scattering angles for all measured energies.

In figure (5-26) the measured values of  $\chi$  at 50 eV incident electron energy are compared with the previous angular correlation measurements at small scattering angles by Eminyán et al. (1975) at 50 eV and Crowe et al. (1981) at 45.6 eV, as well as with the first-order many body calculations by Meneses et al. (1980) and multichannel eikonal theory results by Flannery et al. (1975). There is very good agreement between our results and the theoretical calculations over the wide range.

In figure (5.27) the parameter  $\chi$  is plotted at 80 eV incident energy, along with the values obtained at small scattering angles from the polarization correlation measurements of Standage and Kleinpoppen (1976). The present values are also compared with the angular correlation results of  $|\chi|$  measured by Crowe et al. (1981) at small scattering angles, and MacAdams et al. (1982) at large scattering angles, and with the theoretical calculations of Meneses et al. (1980) and Flannery et al. (1975). There is good agreement between the present results and the theoretical calculations.

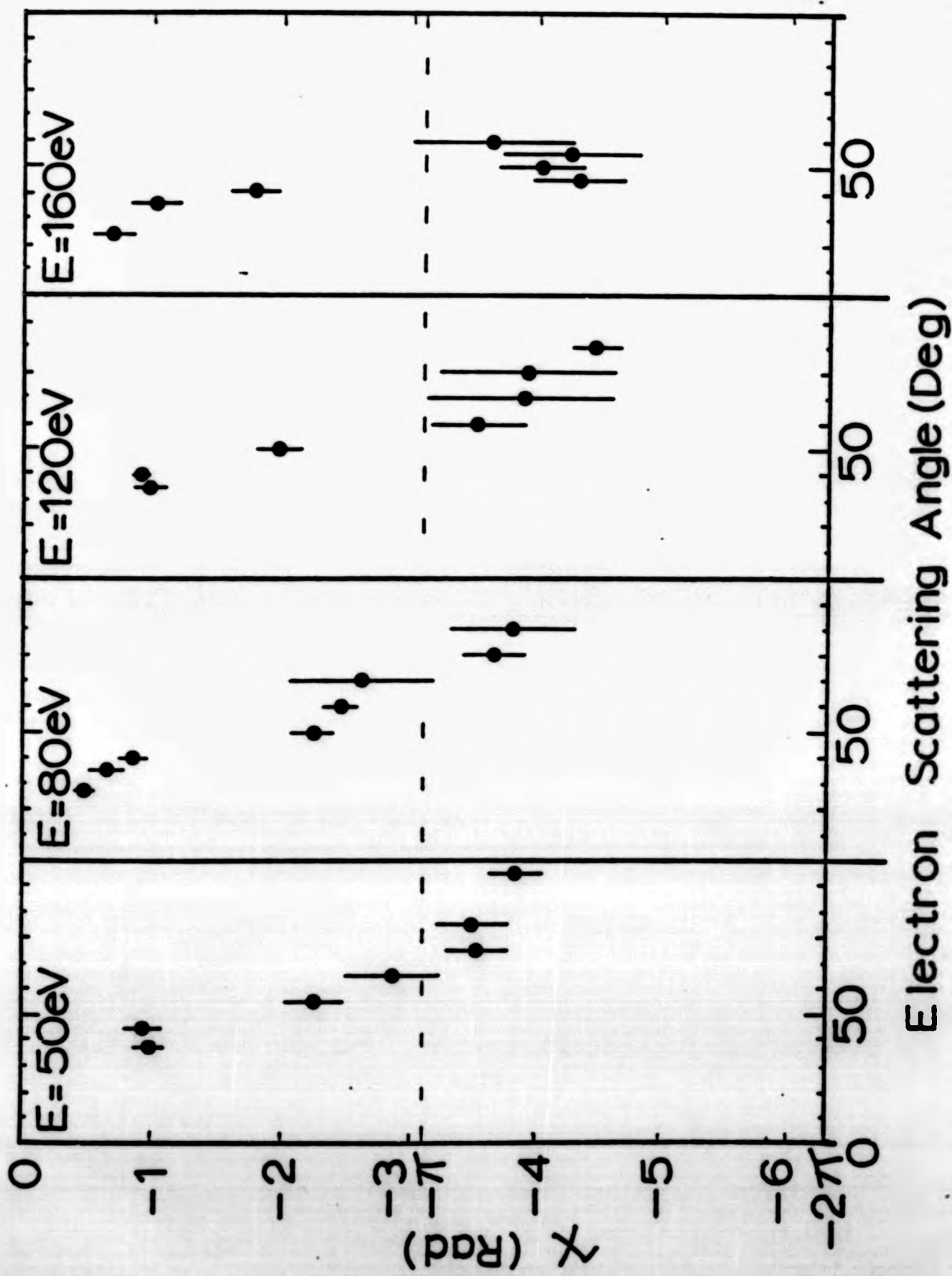


Figure (5-25): The average values of the phase difference  $\chi$  between the helium excitation amplitudes  $a_1 (M_L = \pm 1)$  and  $a_0 (M_L = 0)$  as a function of the electron scattering angle for the measured incident electron energies.

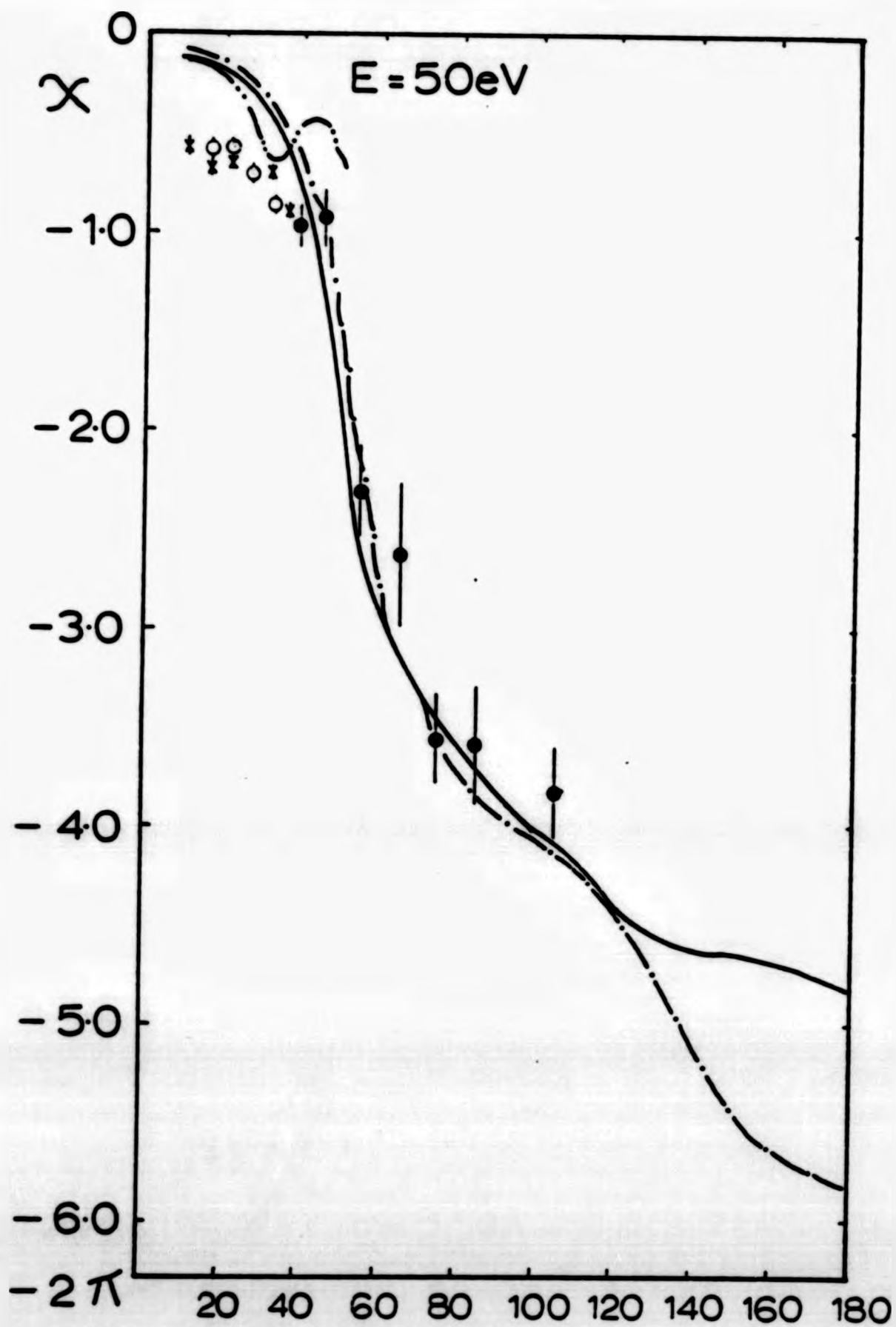


Figure (5-26): The phase difference  $\chi$  between the He  $3^1P$  excitation amplitudes  $a_1(M_L = \pm 1)$  and  $a_0(M_L = 0)$  as a function of the electron scattering angle for the incident electron energy of 50 eV. The present results  $\bullet$  are compared with previous angular correlation results where the sign of  $\chi$  has been chosen in line with the present values; Crowe et al. (1981)  $\times$  at an energy of 45.6 eV and Eminyan et al. (1975)  $\circ$ . As well as with theoretical calculation of Flannery et al. (1975)  $---$ , and Menses et al. (1980)  $---$ .

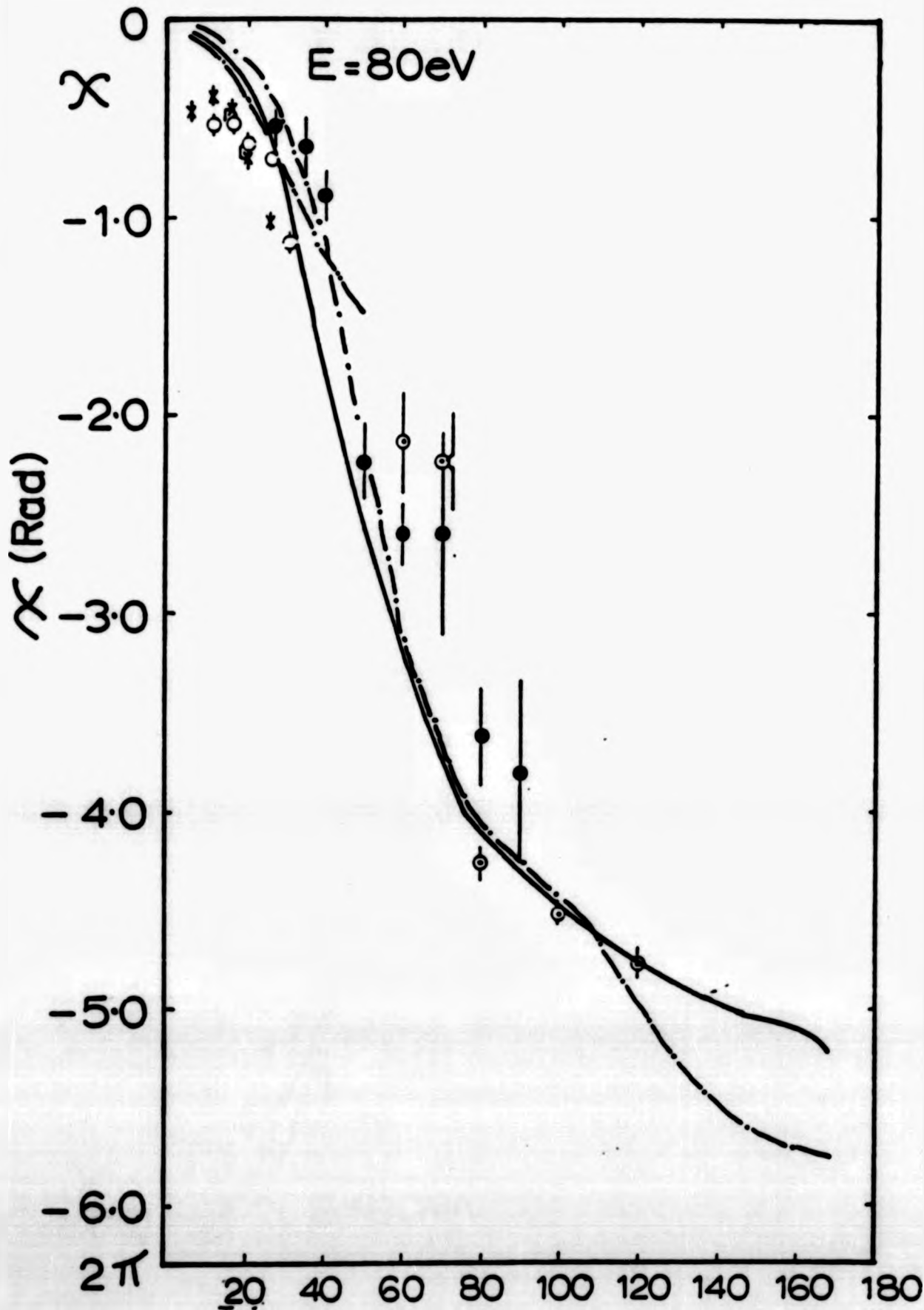


Figure (5-27): The phase difference  $\chi$  between the He  $3^1P_1$  excitation amplitudes  $a_1(M_L=\pm 1)$  and  $a_0(M_L=0)$  as a function of the electron scattering angle at the incident electron energy of 80 eV. The present values  $\bullet$  are compared with previous angular correlation results where the sign of  $\chi$  has been chosen in line with the present values; Crowe et al. (1981)  $\times$ , Eminyany et al. (1975)  $\circ$  and MacAdam et al. (1982)  $\odot$ , as well as with theoretical calculations of Flannery et al. (1975)  $-\cdot-\cdot-$  and Meneses et al. (1980)  $\text{—}$ .

CHAPTER VI  
CONCLUSIONS

The polarization correlation measurements reported in this thesis have extended the complete analysis of the electron impact excitation of the  $3^1P$  state of helium to a wide range of scattering angles and energies. As part of this work the measurement of the circular polarization data can determine the sign of the angular momentum transfer to the atom during the excitation process. It had been a matter of much dispute whether the angular momentum changes sign of some angle other than  $0^\circ$  and  $180^\circ$  and the present data clearly show such a sign change for all energies investigated.

As a result of the low branching ratio of the  $3^1P - 2^1S$  transition the coincidence signals in the present work are very weak, especially at 50 eV and 160 eV where the cross sections and (for 50 eV) the background signal add further to the problem. The effect of the low branching ratio could be overcome by using the  $3^1P - 1^1S$  or  $2^1P - 1^1S$  transitions, but there the difficulties of producing suitable  $\frac{\lambda}{4}$  plates and linear polarizers for the VUV region are only slowly being solved.

With respect to the present study it would be desirable to have some theoretical data for comparison of the 120 eV and 160 eV results. It might also be worthwhile to extend the present linear polarization measurements to the full range of scattering angles used for the circular polarization data as  $\theta_{\min}$  would be expected to change rapidly at large angles. For 50 eV the magnitude of the overall polarization vector  $|\vec{P}|$  was found to be less than the expected value for 1 for a number of scattering angles and it would appear worthwhile to check the origin of this effect if the measurements are rescued.

REFERENCES

1. Andersen N., Gallagher J.W. and Hertel I.V. (1985). Invited Talk 14th Int. Conf.
2. Andersen N., Hertel I.V. and Kleinpoppen H. (1984), J.Phys.B17 L901-908.
3. Andersen N., Andersen T., Ostgaard J. and Horsdal G., (1980), J.Phys.B13 2421-2434.
4. Andersen N., Anderson T., Coke C.L. and Horsdal Pedersen R. (1979) J.Phys.B12 2541-2551.
5. Arriola M., Teubner P.J.D., Ugbabe A. and Weigold E. (1975), J.Phys.B8 1275-1279.
6. Back C., Wright G.r., Tool R.R. and Van der Wiel M.J. (1975) J.Phys.B8
7. Becker H., Angew . (1961) Z.Phys. 13 p59.
8. Beigear J.P., Van Eck J. and Heideman H.G.M. (1984) J.Phys.B17 L265-269.
9. Beyer H.J., McGregor I., Kleinpoppen H. and McIntyre I.C. (1982) J.Phys.B15 L545-548.
10. Beyer H.J. Private Communication.
11. Blum K. (1981) Density Matrix Theory and Application, (Plenum, New York, London).
12. Blum K. and Kleinpoppen H. (1979) Phys.Rep. 52 203-261.
13. Born M. and Wolf E. (1976). "Principle of Optics" (Pergamon, Oxford, London, Edinburgh, New York, Paris, Frankfurt) p12-32 and 544-555.
14. Brannen E., Hunt F.R., Adlington R.H. and Nicholls R.W. (1955) Nature, 175 810-811.
15. Clousing P. (1930) Zeits. F. Physik 66 p471.
16. Crowe A (1983). Invited Talk ICPEAC 1983, Berlin.
17. Crowe A., King T.C.F., Williams J.F. (1981) J.Phys.B14 1219-1228.
18. Da Paixao F.J., Padial N.T. and Casanak G.Y. (1984) Phys.Ref. A30 1697-1713.
19. Deutsch M and Brady E.L. (1947) Phys.Rev. 72 870.
20. Dixon A.J., Hood S.J. and Weigold E. (1978) Phys.Rev.Lett. 40 1262-1266.

21. Dunsworth J.V. (1940) Rev.Sci.Inst. 11 p167.
22. Ehrhardt H., Hesselbacher K.H., Jung K., Schubert E. and Willmann K. (1974) J.Phys.B7 69-78.
23. Ehrhardt H., Schulz M., Tekadt T. and Willmann K. (1969) Phys.Rev.Lett. 22 89-92.
24. Eminyan M., MacAdam K.B., Slevin J. and Kleinpoppen H. (1974) J.Phys.B7 1519-1542
25. Eminyan M., MacAdam K.B., Slevin J., Standage M.C. and Kleinpoppen H (1975) J.Phys.B8 2058-2066.
26. Eminyan M., MacAdam K.B., Slevin J. and Kleinpoppen H. (1973) Phys.Rev.Lett. 31 576-579.
27. Fano U. and Macek J.H. (1973) Rev.Mod.Phys. 45 553-573.
28. Federov V.L. and Mezentsev A.P. (1965) Opt.Spectrosc. 19 p5-8.
29. Flannery M.R. and McCann K.J. (1975) J.Phys. B8 1716-1733.
30. Flower D.R. and Seaton M.J. (1967) Proc.Phys.Soc. 91 59-62.
31. Fon W.C., Brington K.A. and Kingston A.S. (1980) J.Phys.B13 2309-2325.
32. Gibson J.R. and Dolder K.T. (1969) J.Phys.B13 p59.
33. Giordmaine J.A. and Wang T.O. (1960) Appl.Phys. 31 463-471.
34. Hafner H., Kleinpoppen H., Kruger N. (1967) Phys.Lett. 18 p270
35. Hamilton D.R. (1940) Phys.Rev. 58 p122.
36. Harting E. and Read F.H. (1976) Electrostatic Lenses (Amsterdam, Elsevier).
37. Heddle D.W.O. and Kissing R.G.W. (1967) Proc.Roy.Soc. London A299 212-220.
38. Heideman H.G.M., Smith C. and Smith J.A. (1969) Physica 45 305-320.
39. Herman R.W. and Hertel I.V. (1980) J.Phys.B13 4285-
40. Hollywood M.T., Crowe A. and Williams J.F. (1979) J.Phys.B12 819-834.
41. Holt R.A. and Pipkin F.M. (1974) Phys.Rev.A9 581-584.
42. Hughes A.L. and McMillan J.H. (1929) Phys.Rev. 34 291-295.
43. Imhof R. and Read F.H. (1971c) Chem.Phys.Lett. 11 326-328.
44. Imhof R. and Read F.H. (1969) Chem.Phys.Lett. 3 652-654.

21. Dunsworth J.V. (1940) Rev.Sci.Inst. 11 p167.
22. Ehrhardt H., Hesselbacher K.H., Jung K., Schubert E. and Willmann K. (1974) J.Phys.B7 69-78.
23. Ehrhardt H., Schulz M., Tekadt T. and Willmann K. (1969) Phys.Rev.Lett. 22 89-92.
24. Eminyan M., MacAdam K.B., Slevin J. and Kleinpoppen H. (1974) J.Phys.B7 1519-1542
25. Eminyan M., MacAdam K.B., Slevin J., Standage M.C. and Kleinpoppen H (1975) J.Phys.B8 2058-2066.
26. Eminyan M., MacAdam K.B., Slevin J. and Kleinpoppen H. (1973) Phys.Rev.Lett. 31 576-579.
27. Fano U. and Macek J.H. (1973) Rev.Mod.Phys. 45 553-573.
28. Federov V.L. and Mezentsev A.P. (1965) Opt.Spectrosc. 19 p5-8.
29. Flannery M.R. and McCann K.J. (1975) J.Phys. B8 1716-1733.
30. Flower D.R. and Seaton M.J. (1967) Proc.Phys.Soc. 91 59-62.
31. Fon W.C., Brington K.A. and Kingston A.S. (1980) J.Phys.B13 2309-2325.
32. Gibson J.R. and Dolder K.T. (1969) J.Phys.B13 p59.
33. Giordmaine J.A. and Wang T.O. (1960) Appl.Phys. 31 463-471.
34. Hafner H., Kleinpoppen H., Kruger N. (1967) Phys.Lett. 18 p270
35. Hamilton D.R. (1940) Phys.Rev. 58 p122.
36. Harting E. and Read F.H. (1976) Electrostatic Lenses (Amsterdam, Elsevier).
37. Heddle D.W.O. and Kissing R.G.W. (1967) Proc.Roy.Soc. London A299 212-220.
38. Heideman H.G.M., Smith C. and Smith J.A. (1969) Physica 45 305-320.
39. Herman R.W. and Hertel I.V. (1980) J.Phys.B13 4285-
40. Hollywood M.T., Crowe A. and Williams J.F. (1979) J.Phys.B12 819-834.
41. Holt R.A. and Pipkin F.M. (1974) Phys.Rev.A9 581-584.
42. Hughes A.L. and McMillan J.H. (1929) Phys.Rev. 34 291-295.
43. Imhof R. and Read F.H. (1971c) Chem.Phys.Lett. 11 326-328.
44. Imhof R. and Read F.H. (1969) Chem.Phys.Lett. 3 652-654.

45. Imhof R.E. and Read F.H. (1977) Rep.Prog.Phys. 40 1.m-
46. Imhof R.E. and Read F.H. (1971a) J.Phys.B4 450-480.
47. Imhof R.E. and Read F.H. (1971b) J.Phys.B4 1063-1069.
48. Jung K., Schubert E., Paul D.A. and Ehrhardt K. (1975) J.Phys.B8
49. Kaul R.D. (1966) J.Opt.Soc.Am. 56 1262-1263.
50. Khakoo M.A., Forand L., Becker K. and McConkey J.W. (1985) Abst. 14th Int.Conf.
51. Khakoo M.A., Becker K., Forand J.L. and McConkey J.W. (1986) J.Phys.B19
52. King G.C., Adam A. and Read F.H. (1972) J.Phys.B5 L254-257.
53. King G.C., Mohamed K.A., Read F.H. and Imhof R.E. (1976) J.Phys.B9 1274-1280.
54. King G.C., Read F.H. and Imhof R. (1975) J.Phys.B8 665-673.
55. King G.C. and Adam A. (1974) J.Phys.B7, 1712-1718.
56. Kohmoto N. and Fano U. (1981) J.Phys.B14 L477.
57. Kuyatt C.E. and Simpson J. (1967) Rev.Sci.Instrum. 38 103-111.
58. MacFarland R.H. (1962) Phys.Rev. 127 2090-2097.
59. Macek J. and Jaecks D.H. (1971) Phys.Rev.A4 2288-2300.
60. Madison D.H. (1979) J.Phys.B12 3399-3414.
61. Madison D.H. and Winters K.H. (1981) Phys.Rev.Lett. 47 1885-
62. Madison D.H. and Winters K.H. (1983) J.Phys. B16 4437-4450
63. Malcolm I.C. and McConkey J.W. (1979) J.Phys.B12 L67-70.
63. Malcolm I.C. and McConkey J.W. (1979) J.Phys.B12 511-519.
64. Malik A. Thesis submitted to Stirling University (1980).
65. Malik N.A. and Kleinpoppen H. (1980). (Thesis submitted to Stirling University).
66. Marmet P. and Kerwin L. (1960) Can.J.Phys. 38 787-796.
67. MacAdams R., Hollywood M.T., Crowe A. and Williams J.F. (1980) J.Phys.B13 3691.
68. MacAdams R. and Williams J.F. (1982) J.Phys.B15 1247-1251.

69. Meneses G.D. and Csanak G.Y. (1978) J.Phys. B11 L237-242.
70. Moiseiwitsch . and Smith . (1966) Rev.Mod.Phys. 40 238-353.
71. Moustfa H.R., Deheer F.I. and Schutten H. (1969) Physica 40 517-549.
72. Neil P.A. and Crowe A. (1984) J.Phys.B 17 791-795.
73. Ottley T.W. and Kleinpoppen H. (1975) J.Phys.B8 621-627.
74. Poppet M., Schafer G. and Bodenstedt E. (1970) Z.Phys. 240 71-92.
75. Percival I.C. and Seaton M.J. (1958) Phil.Trans.R.Soc. A 251 113-138.
76. Pochat A., Rozvel D. and Peress J. (1973) J. de Physique 34 p701.
77. Poultney S. (1972) Advan. Electronics. Electron.Phys. 31 p39.
78. Ramsey N.F. (1963) Molecular Beams (Oxford, Clarendon) p12-21 and 544-555.
79. Scott T. and McDowell M.R.C. (1976) J.Phys.B9 2235-2253.
80. Shaw D.A., Adam A. and King G.C. (1975) J.Phys.B8 2456-2460.
81. Simpson J.A. and Kuyatt C.E. (1963) Rev.Sci.Inst. 34 265-268.
82. Simpson J.A. (1964) Rev.Sci.Inst. 35 p1698.
83. Slevin J. (1985) Rep. on Progress in Phys. Vol.47, No.5 463-511.
84. Slevin J., Porter H.Q., Eminyany M. DeFrance A. Vassilev G. (1980) J.Phys. B13 L23-25.
85. Smith A.J., Imhof R. and Read F.H. (1973) J.Phys. B6 1333-1338.
86. Smith A.J., Read F.H. and Imhof R.E. (1975) J.Phys. B8 2869-2879.
87. Standage M.C. (1977) J.Phys. B10 2789-2796.
88. Standage M.C. and Kleinpoppen H. (1976) Phys.Rev.Lett. 36 577-580.
89. Steirner K. (1928) Z.Phys.52
90. Steph N.C. and Golden D.E. (1983) Phys.Rev. A27 1676-1681.
91. Steph N.C. and Golden D.E. (1982) Phys.Rev.A26 148-153.
92. Steph N.C. and Golden D.E. (1980) Phys.Rev.A21 759-770.
93. Sutcliffe V.C., Haddad G.N., Steph N.C. and Golden D.E. (1978) Phys.Rev.A17 100-107.
94. Tan K.H., Fryar J., Farago P.S. and McConkey J.M. (1977) J.Phys.B10 1073-1082.

95. Ugbabe A., Teubner P.J.O., Weigold E. and Arriola H. (1977)  
J.Phys.B.10 71-79.
96. Weigold E., Hood S.T. and Teubner P.J.O. (1973) Phys.Rev.Lett.  
30 475-478.
97. Williams J.F., 9th ICPEAC (Seattle).
98. Wykes J. (1972) J.Phys.B5 1126-1137.
99. Zaidi A.A., McGregor I. and Kleinpoppen H. (1980) Phys.Rev. A45  
1168-1171.
100. Zehnle L., Clemens E., Martin P.J., Schauble W. and Kempter V.  
(1978) J.Phys.B11 2865.